ADSORPTION OF LIGHT GASES AND GAS MIXTURES ON ZEOLITES AND NANOPOROUS CARBONS

by

Lucas Mitchell

Dissertation

Submitted to the Faculty of the

Graduate School of Vanderbilt University

in partial fulfillment of the requirements

for the degree of

DOCTOR OF PHILOSOPHY

in

Chemical Engineering

May, 2014

Nashville, Tennessee

Approved:

Professor M. Douglas LeVan

Professor G. Kane Jennings

Professor Peter T. Cummings

Professor Sandra J. Rosenthal

To Caitlin and my family,

for your love and support.

ACKNOWLEDGEMENTS

I would first like to thank my research advisor, Professor M. Douglas LeVan. His patience, guidance, and excelling mentor ability have been an inspiration. I feel that, with his help and support, I have begun to realize my potential in both my research ability and presentation skills. I am thankful and honored for the opportunity to study under his guidance and to be a part of his research team.

I would also like to acknowledge the members of my Ph.D. committee, Professors Peter Cummings, Kane Jennings, and Sandra Rosenthal. Their critiques and insight into my research have been extremely helpful in my growth as a researcher and keeping my on track to complete my thesis. The staff of our department also deserve thanks, including Mary Gilleran and Rae uson for their general assistance, and Mark Holmes for his technical help and assistance with the equipment.

The National Space Biomedical Research Institute, the National Aeronautics and Space Administration Experimental Program to Stimulate Competivite Research, and NASA George C. Marshall Space Flight Center are also graciously acknowledged for funding this research. It has been a privilege to present at project team meetings and to network with other scientists and engineers. I would specifically like to acknowledge James Ritter, Armin Ebner, and James Knox for stimulating research discussions and and general assistence with my research. Bryan Schindler has also been of invaluable help with understanding and implementing Density Functional Theory.

I wish to thank members of the LeVan research group for stimulating discussions and assistance during my time here. Specifically, I would like to thank Yu Wang for her assistance with constructing my apparatus and operating the equipment necessary for my research, as well as general guidance throughout my time as a graduate student. I would like to thank Amanda Furtado for her assistance and support throughout my time as a graduate student.

I wish to thank Jian Liu for his guidance in my experiments and intoducing me to the equipment that I used for my thesis. I would also like to acknowledge Tim Giesy, Dushyant Barpaga, and Trenton Tovar, as well as Robert Harl from Bridget Roger's research group, for stimulating conversations and insight.

Finally, I would like to acknowledge my family for all their support and contributions. I am eternally grateful to my parents for encouraging me to pursue my interest in math and science, as well as my brother, for introducing me to the realm of engineering. I am also grateful to my sister and her family for their support throughout my school career. I would also like to acknowledge my fiance, Caitlin, for her love and support. She has helped me to push myself to realize my potential and learn from my mistakes, as well as celebrate my successes. I would also like to thank my future in-laws, CJ, Cindy, and John, for their love and support.

TABLE OF CONTENTS

LIST OF TABLES

LIST OF FIGURES

CHAPTER I

INTRODUCTION

The generation of medical oxygen is a crucial industry to the modern world. More and more people are in need of medical oxygen in their daily lives as the average life expectancy continues to increase. Also, as advances in space travel continue, new technology and separation processes are required to insure the health of future astronauts.

There are three commonly used techniques to generate pure oxygen: cryogenic distillation, water electrolysis, and adsorption. Cryogenic distillation has a high power and equipment requirement, which is acceptable for large industrial applications. For smaller applications, both terrestrial and space, these high power and equipment requirements are unreasonable. Water electrolysis is the current standard for generating oxygen in a spacecraft or space station, but it can quickly exceed cabin oxygen levels when used to provide oxygen to an injured or sick crew member, potentially creating a fire or explosive hazard. The best method is the use of adsorption to produce a stream of pure oxygen, which can also be further pressurized for use in the extravehicular activity suits as well as portable oxygen generation for terrestrial applications.

To generate pure oxygen, three separation steps must take place. First, the removal of water and strongly-bonding impurities like carbon dioxide. Second, the removal of nitrogen, resulting in a stream consisting of 95% oxygen and 5% argon. Lastly, and the most challenging separation, argon is removed to yield a pure oxygen stream. Different zeolites have been used for many years to accomplish the first two separations using differences in the isotherm loadings. For the third separation, a different type of adsorbent must be utilized. Carbon molecular sieves are able to effectively separate oxygen and argon, a feat that zeolites are unable to accomplish.

The thrust of this dissertation is to measure fundamental adsorption equilibrium properties for adsorbents selected to be used in the next generation oxygen concentrator. The result will benefit government and private space ventures, as well as the terrestrial medical oxygen field. As well as fundamental measurements, this project has yielded new models that describe the adsorption of light gases, including the constituents of air as well as light alkanes. This is vital, as accurate predictions and models of adsorption, particularly of gas mixtures, can further progress separation processes without the need of experiments.

Chapter 2 focuses on the adsorption of oxygen and nitrogen on a LiLSX (Li-exchanged low silica X) zeolite, both as pure gases and binary mixtures. A new method is developed to measure and predict adsorption equilibrium of binary mixtures across a range of compositions using Henry's law data with one component in excess. To accomplish this, a new volumetric system is constructed to measure binary adsorption equilibrium while minimizing dead volume. Pure oxygen and nitrogen are measured on the zeolite at 25 °C and 75 °C and modeled with a Toth isotherm. Binary mixture Henry's law data are measured for one component while the other is held in excess for both nitrogen and oxygen. The Henry's law behavior are modeled using the ideal adsorbed solution theory and the virial excess mixture coefficients methods, where Toth isotherm is used as the isotherm model for the ideal adsorbed solution theory, and the mixture coefficients are determined solely from the binary Henry's law behavior. Binary Henry's law relations are developed, which agree well with the ideal adsorbed solution theory.

Two methods are used to predict the binary equilibrium across a range of compositions: the ideal adsorbed solution theory and the virial excess mixture coefficients. Using the pure component isotherms and the mixture coefficients determined solely from the Henry's law data, the binary adsorption isotherm of oxygen and nitrogen is predicted with the two different methods. The predicted binary isotherms are compared to experimentally measured binary isotherms, with the virial excess mixture coefficients model describing the experiments

accurately. This new method of predicting binary adsorption equilibrium helps to construct a comprehensive understanding of binary adsorption.

In Chapter 3, a carbon molecular sieve is investigated for the possibility of oxygen generation and oxygen storage. This is an important separation for portable medical oxygen devices as well as for oxygen generation for future space flight missions. Adsorption isotherms are measured for oxygen and argon using an apparatus designed for adsorption of high pressure oxygen. Isotherms are measured for oxygen and argon at temperatures of 25, 50, 75, and 100 °C, as well as nitrogen at 25 °C, and pressures up to 100 bar. Isosteric heats of adsorption are determined for oxygen and argon, which are observed to be relatively constant for increasing loadings and temperatures. High loadings are determined for oxygen, nitrogen, and argon, and compared to other materials in the literature. The oxygen density adsorbed in the carbon molecular sieve is calculated and compared to that of compressed gaseous oxygen.

In Chapter 4, a SAFT-FMT-DFT approach is developed to model adsorption of chain molecules on various surfaces. It combines a form of the statistical associating fluid theory (SAFT), fundamental measure theory (FMT), and density functional theory (DFT) to result in a new approach to describe chain fluids adsorbing onto straight and slit-shaped pores. The main theory, following the initial development by Bryan Schindler for half pores,[1] is updated to include the most recent FMT[2] and expanded to include full pores. The results and graphs were calculated with the improved SAFT-FMT-DFT. Intermolecular attractive potentials of increasing complexity are used to create a more accurate approach, with the results agreeing well with simulations from the literature. Wall attractive potentials of increasing complexity are used, ranging from hard sphere to Lennard-Jones, with results showing increasingly realistic behavior.

In Chapter 5, the SAFT-FMT-DFT approach is used to model adsorption of light gases in slit-shaped carbon pores. The SAFT-FMT-DFT used is the improved version presented in

Chapter 4. The pore densities, isotherms, and pore size distribution are recalculated incorporating the updated FMT as well as the use of full pores. The two gases that are investigated are nitrogen at 77 K and n-pentane at 298.15 K. Parameters were taken from the development of Bryan Schindler for both nitrogen and n-pentane at their respective temperatures, with the wall described by the 10-4-3 potential for carbon walls.[3] Using these parameters, pore densities of nitrogen are modeled and used to determine the pore size distribution of BPL activated carbon. Using the pore size distribution, along with pore densities modeled for pentane, a pentane isotherm is predicted and compared to an experimental isotherm measured by Bryan Schindler.[4]

Finally, Chapter 6 summarizes the major conclusions of this research. Included also are recommendations for future work that have been identified as a result of this dissertation.

References

(1) Schindler, B. J. Henry's Law Behavior and Density Functional Theory Analysis of Adsorption Equilibrium. Ph.D. Dissertation, Vanderbilt University, Nashville, TN, 2008.

(2) Hansen-Goos, H.; Roth, R. Density Functional Theory for Hard Sphere Mixtures: the White Bear Version Mark II. *J. Phys.: Condens. Matter*, **2006**, *18*, 8413–8425.

(3) Steele, W. A. The Physical Interaction of Gases with Crystalline Solids. I. Gas-Solid Energies and Properties of Isolated Adsorbed Atoms. *Surf. Sci.*, **1973**, *36*, 317–352.

(4) Schindler, B. J.; Buettner, L. C.; LeVan, M. D. Transition to Henry's Law in Ultra-Low Concentration Adsorption Equilibrium for n-Pentane on BPL Activated Carbon. *Carbon* **2008**, *46*, 1285–1293.

CHAPTER II

DEVELOPMENT OF ADSORPTION EQUILIBRIUM RELATIONS FOR MIXTURES FROM PURE COMPONENT ISOTHERMS AND HENRY'S LAW BEHAVIOR WITH COMPONENTS IN EXCESS

2.1 Introduction

Understanding adsorption equilibrium is vital for designing new adsorbents and separation processes, which require knowledge of how the pure components and mixtures behave. Yet, measuring adsorption equilibrium for mixtures can be complicated, with the difficulty increasing with the number of gases involved. For a binary system, one often wants to establish an equilibrium relation across a full range of compositions at a specific temperature and total pressure. This is difficult to accomplish conveniently and accurately with common methods, as described below. This chapter proposes a new approach to establish such adsorption equilibrium relations.

The most common technique for measuring mixture data involves the use of a volumetric system. A closed volume, often with a recirculation loop, is dosed with the gases to be adsorbed, and after equilibrium is established, measured gas-phase concentrations give the adsorbed-phase concentrations by material balance. With such a procedure, one has no direct control over either the gas-phase or adsorbed-phase composition. Instead, a dose is partitioned between the adsorbed and gas phases in a manner that is not known *a priori*.

Another technique that can be applied to gas mixtures involves the use of a gravimetric apparatus for measurement of pressure and total mass adsorbed. With the apparatus used in a flow-through mode, a method based on the ideal adsorbed solution theory has been developed to permit determination of the composition of the adsorbed phase. However, this is a rarely applied technique, as it is lacking in accuracy in typical applications.[1] A second

gravimetric technique measures the total mass of the adsorbate, the pressure, and the gas-phase density. The gas-phase composition can be determined, and from that the adsorbed-phase concentrations.[2] This technique can be difficult to use, especially if the gases have similar densities, and it requires a specialized apparatus. Of course, the composition of the gas phase could also be measured by some other means, but then this method resembles the volumetric method.

Some additional techniques allow for the control of the gas-phase composition. The simplest is the chromatographic or breakthrough method, in which a mixture is fed to a bed, the full breakthrough curve is measured, and equilibrium adsorbed-phase concentrations are determined by material balance. To overcome inaccuracies typically involved with the method, specially designed flow-through apparatuses have been constructed. With these, the mixed feed gas flows over the adsorbent until equilibrium is established, and then the adsorbate is completely desorbed and its quantity and composition are determined.[3,4] The shortcomings of this method are the time required to measure each data point and the need to capture all of the gas that desorbs. Clearly, there is a need for a simpler method to establish mixture adsorption equilibrium relations across a full range of compositions.

Independently from the measurement methods, many models have been developed to describe the adsorption of gas mixtures, with the adsorbed solution theory being of major underlying importance. Several are variations on the Langmuir isotherm, such as the dual-site Langmuir model,[5] the multi-site Langmuir model,[6] and the dual-process Langmuir model.[7] One of the most successful methods for treating highly nonideal systems is through the use of the virial equation of state (VEOS). The parameters in the VEOS can be related directly to intermolecular forces, and the number of terms can be expanded or truncated depending on the complexity of the system. Also, it is a straightforward matter to include binary mixtures within the VEOS formalism.[8,9] The VEOS has been extended to create other approaches, including the virial excess mixture coefficient (VEMC) method,[10] which

we will use here. The VEMC method uses the ideal adsorbed solution theory (IAST)[11] as its base and adds mixture terms from the VEOS to correct for nonidealities.[10,12,13]

This chapter includes measurements of pure and mixed gas adsorption equilibria for oxygen and nitrogen on LiLSX (Li-exchanged Low Silica X) zeolite, a common system used for air separation by pressure swing adsorption. Pure gas studies on zeolites for oxygen and nitrogen adsorption have been conducted using multiple methods, including flow-through,[14] volumetric,[15–20,22,24] and gravimetric systems.[23,24] Binary gas studies have been performed with volumetric systems,[14–17] as well as predicted using multiple theories.[5,24] To the best of our knowledge, the data in this chapter are the first reported on a commercial LiLSX adsorbent that cover a full binary composition range for oxygen and nitrogen at multiple temperatures and pressures.

In this chapter, we introduce a novel approach for developing accurate adsorption equilibrium relations for mixed gases. It is based on measuring Henry's law coefficients for a trace component with another component present in excess, with the amount of that excess component varied over the range of its pure component isotherm. In our view, under these circumstances, the trace component is exhibiting a maximum extent of non-ideality, as it is as far away as possible from pure component behavior. These nonidealities are incorporated into the theory by adding correction terms to the ideal adsorbed solution theory. All measurements can be performed quite easily with a volumetric apparatus.

2.2 Theory

Definition of Henry's Law for Gas Mixtures

Thermodynamic consistency of adsorption equilibrium signifies adherence to the Gibbs adsorption isotherm, which is

$$A\, d\pi = \sum_i n_i\, d\mu_i \qquad \text{(constant } T\text{)} \tag{2.1}$$

where A is the surface area of the adsorbent, π is spreading pressure, n_i is the adsorbed-phase concentration of component i, and μ_i is the chemical potential of component i. If adsorption isotherm equations for an ideal or nonideal mixture are developed from an equation of state for spreading pressure by application of the Gibb's adsorption isotherm, then the isotherms will be thermodynamically consistent by definition.

Our concern in this chapter is the application of eq 2.1 to binary systems, with the extension to multicomponent systems being straightforward. For an ideal gas, substitution of the chemical potential into eq 2.1 gives

$$\frac{A}{RT}\, d\pi = \frac{n_1}{p_1}\, dp_1 + \frac{n_2}{p_2}\, dp_2 \tag{2.2}$$

This equation must be integrated along a path from $\pi = 0$ at $p_1 = p_2 = 0$ to the final state at $[p_1, p_2]$, which then permits isotherms to be obtained from

$$\frac{n_i}{p_i} = \left.\frac{\partial(\pi A/RT)}{\partial p_i}\right|_{p_j} \tag{2.3}$$

If both components are in their respective Henry's law limits (i.e., $n_1 = K_1\, p_1$ and $n_2 = K_2\, p_2$), then integration of eq 2.2 gives simply

$$\frac{\pi A}{RT} = K_1\, p_1 + K_2\, p_2 = n_1 + n_2 \tag{2.4}$$

However, if component 1 is in excess and only a trace of component 2 exists, then we can integrate eq 2.2 along a path from $[0, 0]$ to $[p_1, 0]$ and then to $[p_1, p_2]$. This gives

$$\frac{\pi A}{RT} = \left.\frac{\pi A}{RT}\right|_{\substack{\text{pure 1} \\ \text{at } p_1}} + H_2\, p_2 \tag{2.5}$$

where the Henry's law coefficient for trace component 2 with component 1 in excess is defined by

$$H_2 \equiv \left.\frac{\partial n_2}{\partial p_2}\right|_{p_1} \quad \text{as} \quad p_2 \to 0 \quad (\text{constant } T) \tag{2.6}$$

Note that from eqs 2.3 and 2.5, we have simply $H_2 = n_2/p_2$ as p_2 approaches zero at constant p_1. Thus, in this chapter, we use eq 2.6 as the definition of the Henry's law coefficient of

component 2 for a binary gas mixture with component 1 in excess. We note that in general, for mixtures with more components, we would have

$$H_i = H_i(\overline{p}_j, T) \equiv \left.\frac{\partial n_i}{\partial p_i}\right|_{\overline{p}_j} \quad \text{as} \quad p_i \to 0 \tag{2.7}$$

where $i \notin \overline{j}$.

Relation to Ideal Adsorbed Solution Theory

The ideal adsorbed solution theory of Myers and Prausnitz[11] is based on a few key equations. First and foremost, the partial pressure of a gas over an adsorbed phase is given by

$$P_i = x_i\, P_i^o(\pi) \qquad \text{(constant T)} \tag{2.8}$$

where the pure-component standard state P_i^o is evaluated at the spreading pressure of the mixture. The spreading pressure for a pure component is obtained by integrating eq 2.1 to obtain

$$\frac{\pi A}{RT} = \int_0^{P_i^o} \frac{n_i}{p_i}\, dp_i \tag{2.9}$$

A pure component isotherm is represented by $n_i^o = n_i^o(P_i^o)$. With all components at the spreading pressure of the mixture, the total quantity adsorbed is calculated from the Amagat's law expression

$$\frac{1}{n_t} = \frac{x_1}{n_1^o} + \frac{x_2}{n_2^o} \tag{2.10}$$

Quantities adsorbed for the individual components are then given by

$$n_i = x_i\, n_t \tag{2.11}$$

For the case of component 1 being in excess and component 2 being in its Henry's law limit, since $x_1 \approx 1$, the spreading pressure of the mixture and the total quantity adsorbed will be determined largely by the component in excess, i.e.,

$$n_t \approx n_1^o \tag{2.12}$$

as given by eq 2.10. Therefore, from eqs 2.8, 2.11, and 2.12, the Henry's law constant is

$$H_2 = \frac{n_2}{P_2} = \frac{x_2\, n_1^o}{x_2\, P_2^o} = \frac{n_1^o}{P_2^o} \tag{2.13}$$

where all standard state quantities are evaluated at the spreading pressure of the mixture. This is a powerful relation, with the binary Henry's law constant of trace component 2, with component 1 in excess, depending only on the pure component 1 loading and the pure component 2 pressure at the spreading pressure of the mixture. As $n_1 \to 0$, eq 2.12 no longer applies, and the Henry's law coefficient becomes simply $H_2 = n_2/P_2$, the pure component value.

Incorporation of Virial Excess Mixture Coefficients

The virial equation of state is one of the most accurate theories for describing highly nonideal systems. For a pure gas, the virial equation is

$$\frac{\pi A}{RT} = n_1 + B_{11} n_1^2 + C_{111} n_1^3 + \ldots \tag{2.14}$$

For a binary mixture, the virial equation gives the spreading pressure using both pure component and mixture coefficients in the form

$$\begin{aligned} \frac{\pi A}{RT} \;=\; & n_1 + B_{11} n_1^2 + C_{111} n_1^3 + \ldots + \\ & n_2 + B_{22} n_2^2 + C_{222} n_2^3 + \ldots + \\ & 2B_{12} n_1 n_2 + 3C_{112} n_1^2 n_2 + 3C_{122} n_1 n_2^2 + \ldots \end{aligned} \tag{2.15}$$

The mixing at a surface in an adsorbed solution can be considered as arising from both ideal and excess mixing contributions. Thus, each virial mixture coefficient can be written as the sum of ideal and excess contributions, for example

$$B_{ij} = B_{ij}^{id} + B_{ij}^{E} \tag{2.16}$$

where B_{ij}^{id} and B_{ij}^{E} are the ideal and excess mixing coefficients, respectively.[10]

The virial equation of state can be rearranged with these new coefficients incorporated to give

$$\begin{aligned}\frac{\pi A}{RT} &= n_1 + B_{11}n_1^2 + C_{111}n_1^3 + \ldots + \\ & \quad n_2 + B_{22}n_2^2 + C_{222}n_2^3 + \ldots + \\ & \quad 2B_{12}^{id}n_1n_2 + 3C_{112}^{id}n_1^2n_2 + 3C_{122}^{id}n_1n_2^2 + \ldots + \\ & \quad 2B_{12}^{E}n_1n_2 + 3C_{112}^{E}n_1^2n_2 + 3C_{122}^{E}n_1n_2^2 + \ldots \end{aligned} \tag{2.17}$$

which can be represented in terms of contributions by

$$\frac{\pi A}{RT} = \left.\frac{\pi A}{RT}\right|_{pure\,1} + \left.\frac{\pi A}{RT}\right|_{pure\,2} + \left.\frac{\pi A}{RT}\right|_{mixing}^{id} + \left.\frac{\pi A}{RT}\right|_{mixing}^{E} \tag{2.18}$$

or

$$\frac{\pi A}{RT} = \left.\frac{\pi A}{RT}\right|_{IAS} + \left.\frac{\pi A}{RT}\right|_{mixing}^{E} \tag{2.19}$$

where $\pi A/RT|_{pure\,1}$ and $\pi A/RT|_{pure\,2}$ signify the contributions from the pure components; $\pi A/RT|_{mixing}^{id}$ signifies the ideal surface mixing contribution as given by the third line in eq 2.17; $\pi A/RT|_{mixing}^{E}$ signifies the excess surface mixing contribution as given by the fourth line in eq 2.17; and $\pi A/RT|_{IAS}$ signifies the total contribution from an ideal adsorbed solution, i.e., the summation of the first three lines of eq 2.17 or the first three terms on the right side of eq 2.18. Thus, the equation of state is

$$\frac{\pi A}{RT} = \left.\frac{\pi A}{RT}\right|_{IAS} + 2B_{12}^{E}n_1n_2 + 3C_{112}^{E}n_1^2n_2 + 3C_{122}^{E}n_1n_2^2 + \ldots \tag{2.20}$$

The corresponding isotherms are[10]

$$\ln p_1 = \ln p_{IAS\,1} + 2B_{12}^{E}n_2 + 3C_{112}^{E}n_1n_2 + \frac{3}{2}C_{122}^{E}n_2^2 + \ldots \tag{2.21}$$

$$\ln p_2 = \ln p_{IAS\,2} + 2B_{12}^{E}n_1 + \frac{3}{2}C_{112}^{E}n_1^2 + 3C_{122}^{E}n_1n_2 + \ldots \tag{2.22}$$

where $p_{IAS\,i}$, the partial pressure of component i in equilibrium with an ideal adsorbed solution, can be calculated from the IAST.

All mixture coefficients through the ternary C-terms can be evaluated from Henry's law data measured with a second component in excess. Thus, writing eq 2.21 in the Henry's law limit for component 1 (i.e., $n_1 \to 0$) with component 2 in excess and vice versa for eq 2.22 gives

$$\ln \frac{p_1}{n_1} = -\ln H_1 = -\ln K_1 + 2B_{12}n_2 + \frac{3}{2}C_{122}n_2^2 + \dots \tag{2.23}$$

$$\ln \frac{p_2}{n_2} = -\ln H_2 = -\ln K_2 + 2B_{12}n_1 + \frac{3}{2}C_{112}n_1^2 + \dots \tag{2.24}$$

where $H_1 = H_1(n_2)$ and $H_2 = H_2(n_1)$ are the Henry's law coefficients with the second component in excess. Note that eqs 2.23 and 2.24 contain all of the virial cross-coefficients that appear in eq 2.15 or 2.20. Thus, all information needed to determine adsorption equilibrium for the mixture using the virial equation of state through C-terms is contained in the pure component isotherms and the Henry's law coefficients measured with the second component in excess.

2.3 Experimental Section

Materials

The LiLSX zeolite used in this research was Oxysiv MDX in 30×60 mesh form (lot 2010011670) from Honeywell UOP. All data were measured on a single 0.9085 g sample of the zeolite. All gases were ultrahigh purity (99.99%) and obtained from Airgas and Air Liquide.

Apparatus

The volumetric apparatus is shown in Fig. 3.1. A diaphragm pump was used to recirculate gases in a closed loop. Pressures were measured with an MKS Baratron Type 121A pressure transducer, which was located within the recirculation loop to minimize dead volume and to ensure proper mixing. These pressure measurements were used with the dosing cylinder to determine the amounts of adsorbable components in the apparatus. The

gas chromatograph was an Agilent Technologies 7890A with a TCD detector and 15 m 5A zeolite-lined column. Injections to the gas chromatograph were accomplished using a 6-port, 2-position VICI gas sampling valve. The volume of the recirculation loop, determined by helium expansion, was 44.7 mL; of this volume, 10.7 mL was associated with the region containing the pressure transducer. A mechanical vacuum pump was connected to the apparatus to provide vacuum.

Measurement of Adsorption Equilibria

The zeolite was regenerated at 300 °C in a Micromeritics ASAP 2020 porosimeter to determine the dry weight. The sample was then loaded into the adsorption bed and regenerated a second time under vacuum at 300 °C overnight.

Pure gas isotherms were measured by stepping up isotherms in the usual manner for a volumetric system. The gas charges to the system were determined using the dosing volume and pressure transducer. Residual gas-phase concentrations were measured with the gas chromatograph.

To measure binary equilibria in the Henry's law limit, the region containing the dosing cylinder and pressure transducer was isolated, evacuated, and then charged with the trace gas. The pressure was recorded, and valves were switched to permit entry of a small amount of the gas to the recirculation loop, with that amount determined by the pressure reduction. The pressure transducer region was then isolated, re-evacuated, and the gas to be present in excess was introduced similarly. The recirculation pump was activated, allowing the system to equilibrate, generally overnight. Multiple injections were introduced to the gas chromatograph to yield an accurate reading, and these were accounted for in the material balance. More of the excess gas was then added to the recirculation loop for the next data point. Prior to switching gases, the adsorbent was regenerated at 300 °C under vacuum for 8 hours. Some helium was added to the system to enable the recirculation pump to function

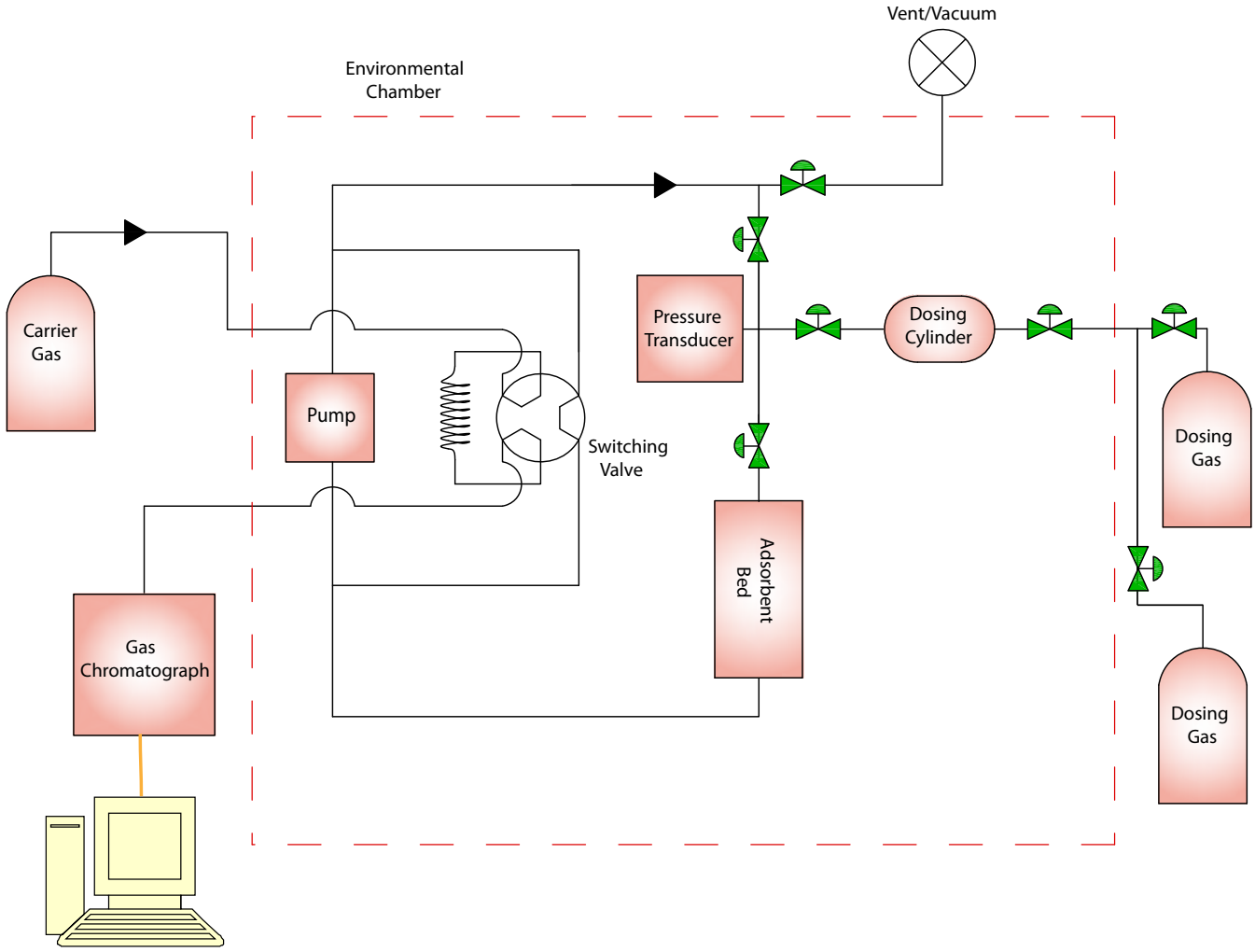

Figure 2.1: Schematic of recirculating volumetric system.

optimally.

To measure binary equilibria over the full recomposition range at 0.25 and 1 bar at 25 and 75 °C, a similar procedure was followed. Both gases were introduced to the system in non-trace amounts. After a measurement had been completed, the adsorbent was regenerated prior to introducing gases for the next data point. Some helium was added to the system for measurements at 0.25 bar.

2.4 Results and Discussion

Pure Gas

Pure component isotherms were measured for nitrogen and oxygen at 25 and 75 °C and pressures up to 5 bar and are shown in Figure 3.2. These were described by the Toth isotherm, written in the form[21]

$$n = \frac{NKP}{[1 + (KP)^t]^{1/t}} \tag{2.25}$$

where N is the monolayer capacity, K describes the adsorption affinity, and t is a measure of adsorbent homogeneity. The Toth isotherm parameters are given in Table 2.1. These were obtained by minimizing the sum of the differences between predicted and measured values of $\ln P$. Spreading pressures were calculated for the pure components using[26]

$$\frac{\pi A}{RT} = N \left[\theta - \frac{\theta}{t} \ln(1 - \theta^t) - \sum_{j=1}^{\infty} \frac{\theta^{jt+1}}{jt(jt+1)} \right] \tag{2.26}$$

where $\theta = n/N$.

Binary Henry's Law

Henry's law coefficients with one component in excess were measured using the procedure described above. The partial pressure of the trace gas was less than 2% of the total pressure near 1 bar. The gas present in excess was increased in pressure at regular intervals

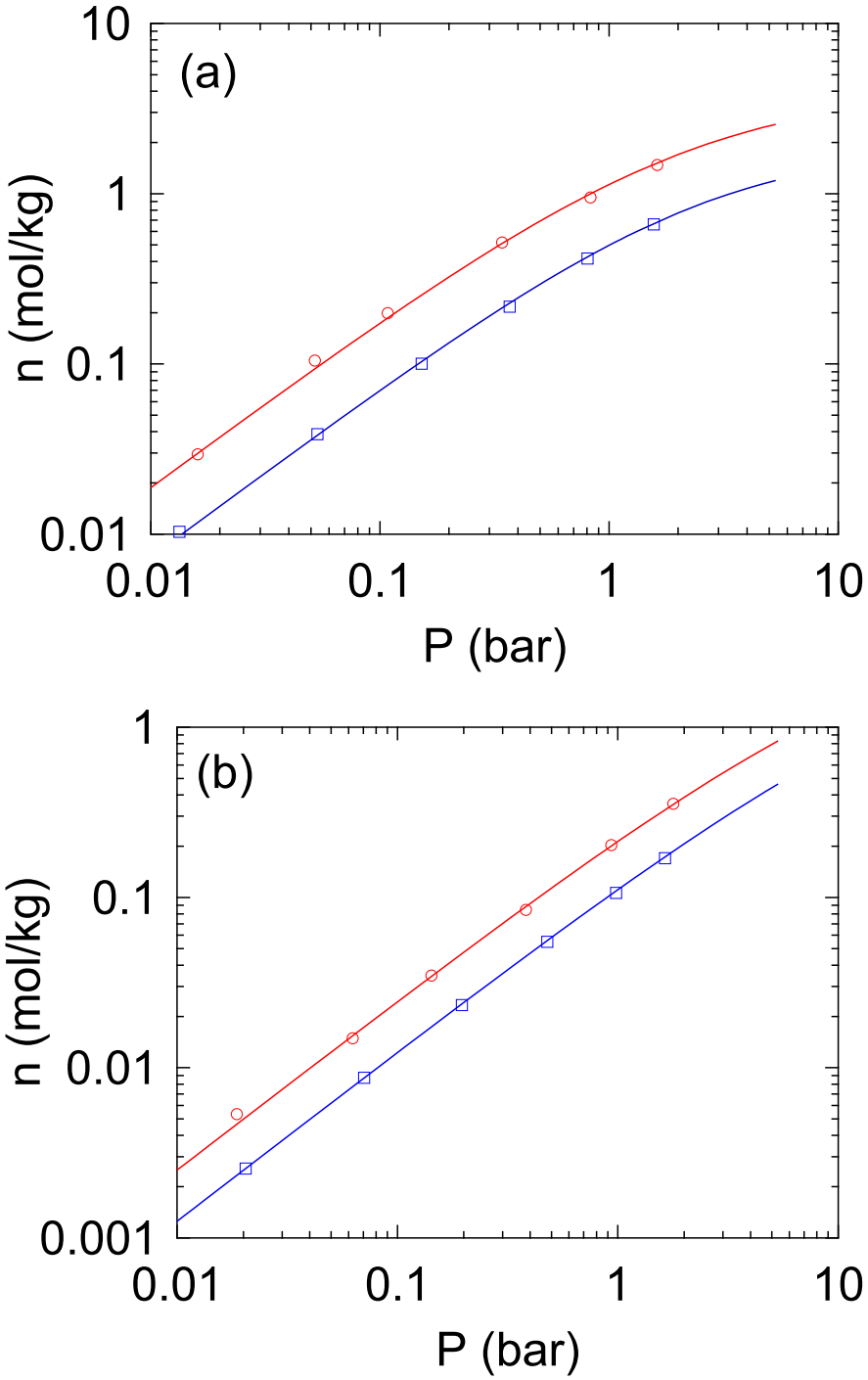

Figure 2.2: Pure gas adsorption isotherms at 25 and 75 °C. (a) nitrogen and (b) oxygen. Curves are Toth isotherms.

Table 2.1: Parameters for pure component Toth isotherms.

Gas	T K	N mol/kg	K bar^{-1}	t
Nitrogen	298.15	3.77	0.582	0.721
	348.15	2.87	0.253	0.720
Oxygen	298.15	2.17	0.111	0.946
	348.15	2.09	4.87×10^{-2}	0.918

as measurements were made. At the lowest pressures, both gases were in the linear ranges of their respective pure component isotherms.

Mixture data were described by two methods. Toth IAST is used below to indicate that the ideal adsorbed solution theory was used with the pure component Toth isotherms to predict the binary equilibria. Toth VEMC indicates that virial excess mixture coefficients were added to the method, as given by eqs 2.21 and 2.22.

Binary Henry's law behavior for 25 and 75 °C is shown in Figures 3.4 and 3.5 for nitrogen and oxygen, respectively. Note that the Henry's law coefficient for nitrogen decreases strongly at oxygen pressures below 0.25 bar. The Henry's law coefficients were modeled with the Toth IAST and Toth VEMC relations. The VEMC mixture coefficients, given in Table 2.2, were obtained by minimizing the sum of the differences between predicted and measured values of $\ln P$ in eqs 2.23 and 2.24. The mixture Henry's law relation developed in eq 2.13 agrees with the trial-and-error calculations using the IAST, overlapping the IAST curves of Figures 3.4 and 3.5. The Toth IAST is able to describe the binary Henry's law data with some success; however, the lack of a quantitative fit suggests that there are nonidealities in the mixture. The Toth VEMC accurately describes the Henry's law behavior for both gases at 25 and 75 °C.

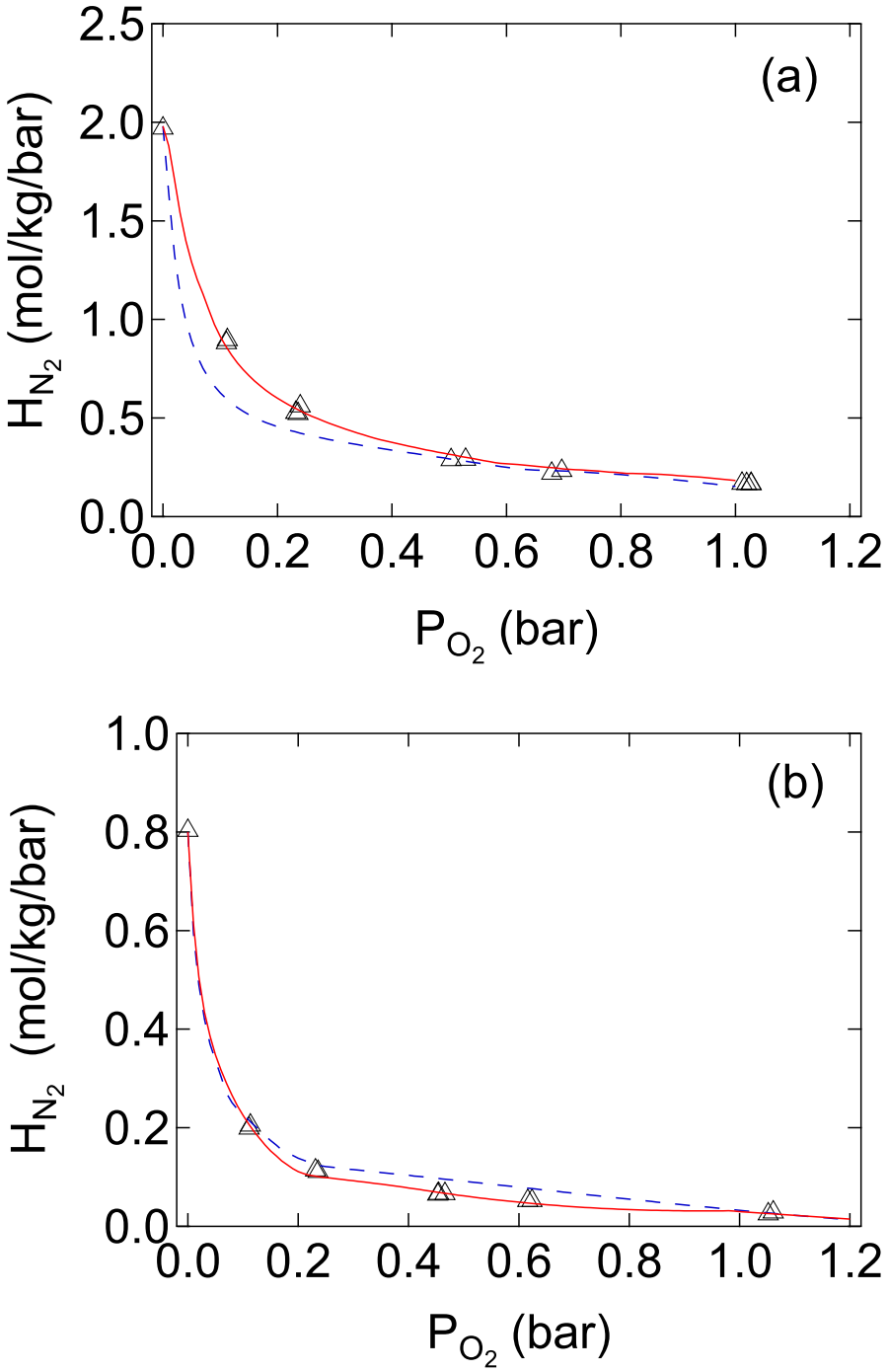

Figure 2.3: Henry's law behavior for nitrogen with oxygen in excess: (a) 25 °C and (b) 75 °C. Dashed curves are the Toth IAST, and solid curves are the Toth VEMC.

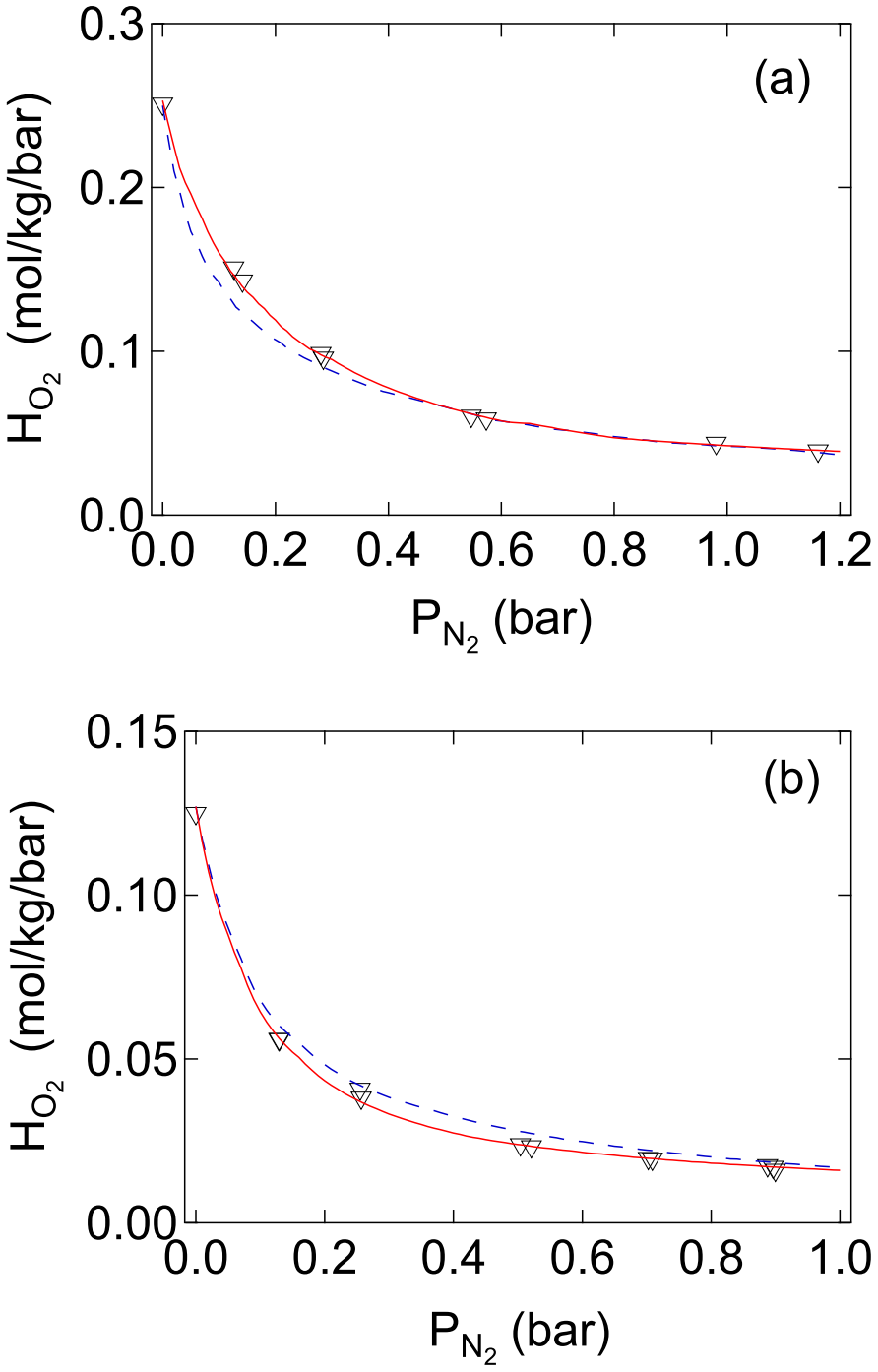

Figure 2.4: Henry's law behavior for oxygen with nitrogen in excess: (a) 25 °C and (b) 75 °C. Dashed curves are the Toth IAST, and solid curves are the Toth VEMC.

Table 2.2: Mixture parameters for Toth VEMC isotherm model.

T	B_{12}^E	C_{112}^E	C_{122}^E
K	$(mol/kg)^{-1}$	$(mol/kg)^{-2}$	$(mol/kg)^{-2}$
298.15	2.89	-6.71	-3.98
348.15	1.39	-14.9	-2.41

Binary Equilibrium Isotherms

Binary equilibria were measured for nitrogen and oxygen at 25 and 75 °C and are shown in Figures 3.6 and 3.7. The isotherms were measured over the full composition space at total nominal pressures of 0.25 and 1.0 bar.

The binary equilibria over the full composition range were predicted for both gases using the Toth IAST and Toth VEMC. The three mixture parameters of the Toth VEMC were determined solely from the binary Henry's law data. The Toth IAST, while able to predict the general trends in the isotherms, is not quantitatively accurate, suggesting that the mixture has a nonideal aspect that is not accounted for by the IAST. However, using the mixture parameters deduced from the Henry's law measurements, the Toth VEMC accurately predicts the equilibria over the full range of compositions. This is noteworthy, as it gives a full spectrum understanding of binary mixtures and how the Henry's law behavior ultimately affects the binary isotherms.

2.5 Conclusions

A new approach for constructing adsorption equilibrium relations for gas mixtures has been reported in this chapter. Pure isotherms are measured as well as Henry's law coefficients for a trace gas with another gas in excess; under this condition, the trace gas is as far away as possible from its pure component behavior and thus should be exhibiting a maximum degree of nonideality. Virial excess mixture coefficients can be calculated from the Henry's law data, and these can be used to improve the predictions of the ideal adsorbed solution

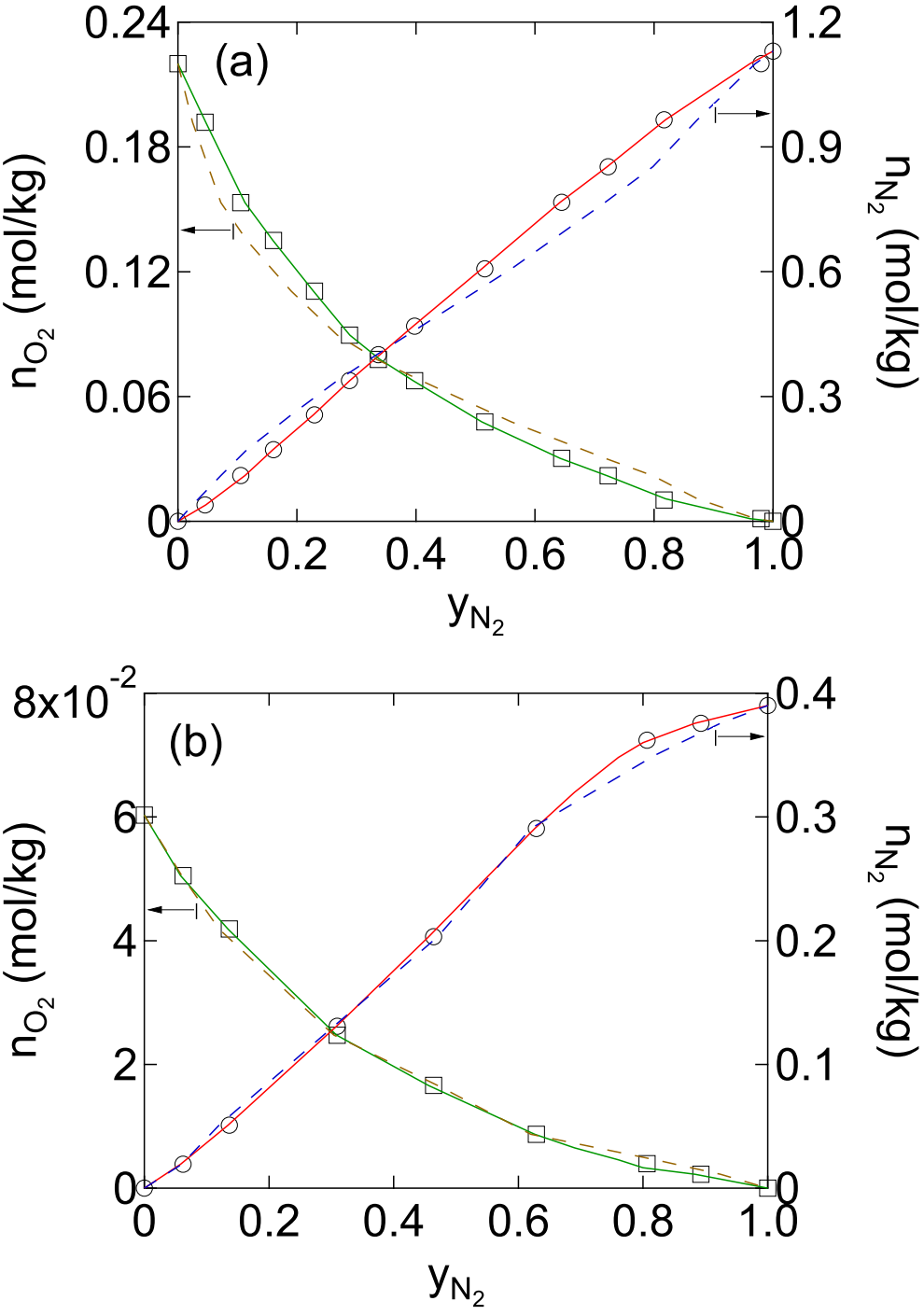

Figure 2.5: Binary adsorption isotherms for nitrogen (◯) and oxygen (□) at 25 °C. (a) 1.0 bar and (b) 0.25 bar, nominally. Dashed curves are the Toth IAST, and the solid curves are the Toth VEMC.

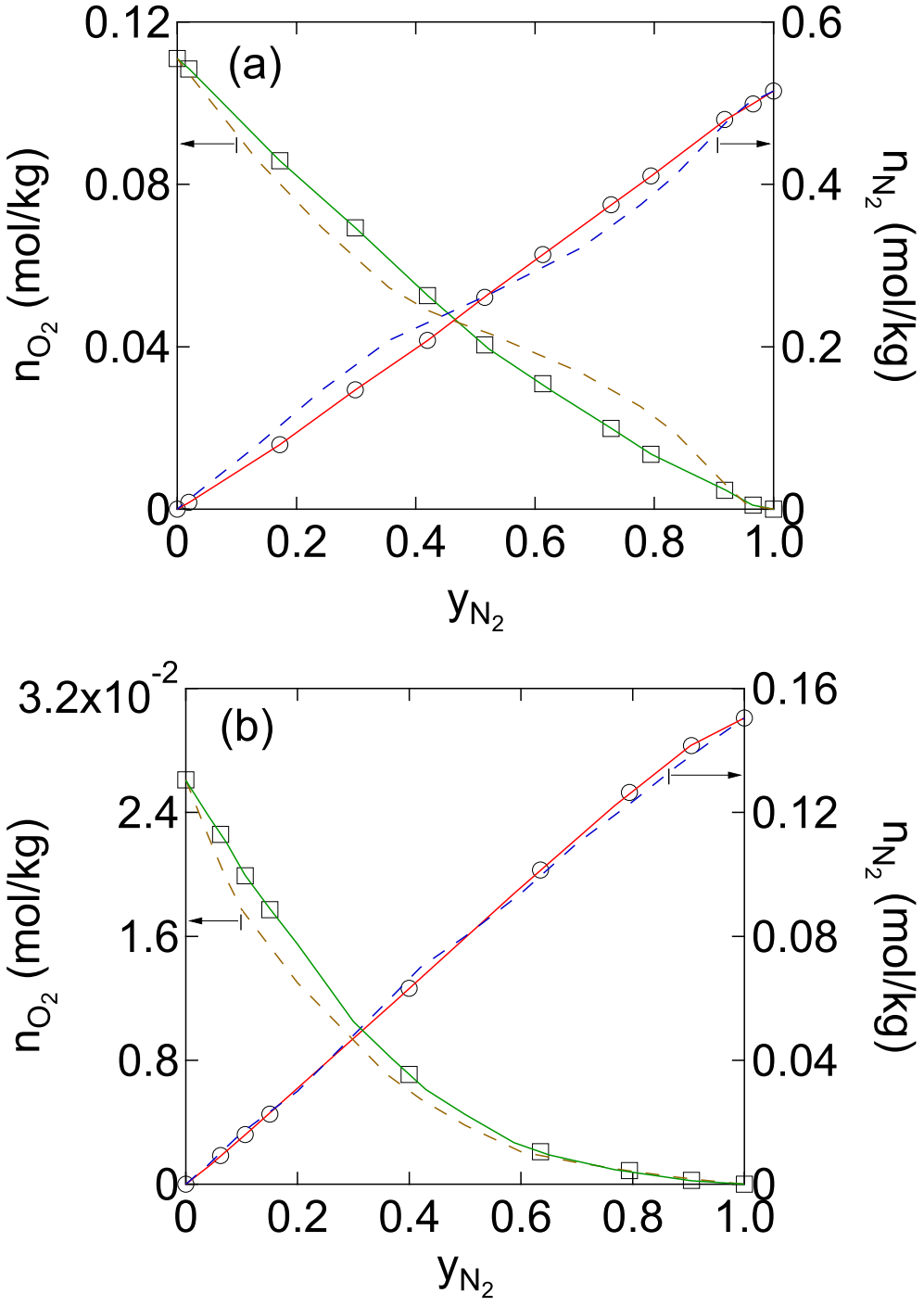

Figure 2.6: Binary adsorption isotherms for nitrogen (◯) and oxygen (□) at 75 °C. (a) 1.0 bar and (b) 0.25 bar, nominally. Dashed curves are the Toth IAST, and solid curves are the Toth VEMC.

theory. The entire approach begins with an equation of state and is thermodynamically consistent. Activity coefficients, if desired, can be calculated as described elsewhere.[10]

To test the approach, pure component adsorption isotherms were measured for oxygen and nitrogen adsorbed on a LiLSX zeolite at 25 and 75 °C at pressures up to 5 bar. These data were described accurately using the Toth isotherm. Binary Henry's law behavior was measured with one component in excess for both nitrogen and oxygen. A new IAST relation, given by eq 2.13, was developed for the binary Henry's law coefficient with a component in excess using pure component loadings and pressures at the mixture spreading pressure, and it agrees with traditional calculations. A Toth IAST model was able to describe the general shape of the data, but was not able to account for nonidealities accurately. Inclusion of virial mixture coefficients, calculated solely from the Henry's law data, led to much more accurate predictions of the Henry's law mixture data.

Binary adsorption isotherms of nitrogen and oxygen were measured across a full range of compositions at 25 and 75 °C and nominal pressures of 0.25 and 1.0 bar. These were predicted using the Toth IAST and Toth VEMC methods, the latter using the mixing parameters obtained exclusively from the binary Henry's law measurements. The Toth IAST method was able to predict the general qualitative trends in adsorption equilibria, but did not give accurate quantitative predictions. The Toth VEMC was able to predict the binary equilibria accurately for the full range of compositions, pressures, and temperatures. Thus, by using Henry's law data with one component in excess, an accurate adsorption equilibrium relation could be developed for the mixture.

References

(1) Karavias, F.; Myers, A. L. Molecular Thermodynamics of Adsorption from Gas Mixtures: Composition of Adsorbed Phase from Gravimetric Data. *Chem. Eng. Sci.* **1992**, *47*, 1441–1451.

(2) Dreisbach, F.; Lösch, H. W. Magnetic Suspension Balance for Simultaneous Measurement of a Sample and the Density of the Measuring Fluid. *J. Therm. Anal. Calorim.* **2000**, *62*, 515–521.

(3) Talu, O.; Zwiebel, I. Multicomponent Adsorption Equilibria of Nonideal Mixtures. *AIChE J.* **1986**, *32*, 1263–1276.

(4) Russell, B. P.; LeVan, M. D. Coadsorption of Organic Compounds and Water Vapor on BPL Activated Carbon. 3. Ethane, Propane, and Mixing Rules. *Ind. Eng. Chem. Res.* **1997**, *36*, 2380–2389.

(5) Mathias, P. M.; Kumar, R.; Moyer, Jr., J. D.; Schork, J. M.; Srinivasan, S. R.; Auvil, S. R.; Talu, O. Correlation of Multicomponent Gas Adsorption by the Dual-Site Langmuir Model. Application to Nitrogen/Oxygen Adsorption on 5A-Zeolite. *Ind. Eng. Chem. Res.* **1996**, *35*, 2477–2483.

(6) Nitta, T.; Shigetomi, T.; Kuro-oka, M.; Katayama, T. An Adsorption Isotherm of Multi-Site Occupancy Model for Homogeneous Surface. *J. Chem. Eng. Jpn.* **1984**, *17*, 39–45.

(7) Ritter, J. A.; Bhadra, S. J.; Ebner, A. D. On the Use of the Dual-Process Langmuir Model for Correlating Unary Equilibria and Predicting Mixed-Gas Adsorption Equilibria. *Langmuir* **2011**, *27*, 4700–4712.

(8) Taqvi, S. M.; LeVan, M. D. A Simple Way to Describe Nonisothermal Adsorption Equilibrium Data Using Polynomials Orthogonal to Summation. *Ind. Eng. Chem. Res.* **1997**, *36*, 419–423.

(9) Taqvi, S. M.; LeVan, M. D. Virial Description of Two-Component Adsorption on Homogeneous and Heterogeneous Surfaces. *Ind. Eng. Chem. Res.* **1997**, *36*, 2197–2206.

(10) Qi, N.; LeVan, M. D. Virial Excess Mixing Coefficient Corrections for the Adsorbed Solution Theory. *Ind. Eng. Chem. Res.* **2005**, *44*, 3726–3732.

(11) Myers, A. L.; Prausnitz, J. M. Thermodynamics of Mixed-Gas Adsorption. *AIChE J.* **1965**, *11*, 121–127.

(12) Qi, N.; LeVan, M. D. Coadsorption of Organic Compounds and Water Vapor on BPL Activated Carbon. 5. Methyl Ethyl Ketone, Methyl Isobutyl Ketone, Toluene, and Modeling. *Ind. Eng. Chem. Res.* **2005**, *44*, 3733–3741.

(13) Wang, Y.; LeVan, M. D. Adsorption Equilibrium of Binary Mixtures of Carbon Dioxide and Water Vapor on Zeolites 5A and 13X. *J. Chem. Eng. Data* **2010**, *55*, 3189–3195.

(14) Talu, O; Li, J.; Kumar, R.; Mathias, P. M.; Moyer, J. D., Jr.; Schork, J. M. Measurement and Correlation of Oxygen/Nitrogen/5A-Zeolite Adsorption Equilibria for Air Separation *Gas. Sep. Purif.* **1996**, *10*, 149–159.

(15) Agha, R. K.; De Weireld, G.; Frère, M. A Complete Set of Experimental Devices for the Determination of the Gas Separation Capacity of Adsorbents. *Adsorption* **2005**, *11*, 179–182.

(16) Zonata, M. L.; Heymans, N.; Gilles, F.; Su, B. L.; Frère, M.; De Weireld, G. Adsorption Isotherms of Pure Gas and Binary Mixtures of Air Compounds on Faujasite Zeolite Adsorbents: Effect of Compensation Cation. *J. Chem. Eng. Data* **2010**, *55*, 448–458.

(17) Zonata, M. L.; Heymans, N.; Gilles, F.; Su, B. L.; De Weireld, G. Thermodynamic Study of NiNaKLSX Zeolites with Different Li Exchange Rate for N_2/O_2 Separation Process. *Micro. Meso. Mater.* **2011**, *143*, 302–310.

(18) Sethia, G.; Pillai, R. S.; Dangi, G. P.; Somani, R. S.; Bajaj, H. C.; Jasra, R. V. Sorption of Methane, Nitrogen, Oxygen, and Argon in ZSM-5 with Different SiO_2/Al_2O_3 Ratios: Grand Cononical Monte Carlo Simulation and Volumetric Measurements. *Ind. Eng. Chem. Res.* **2010**, *49*, 2353–2362.

(19) Bao, Z.; Yu, L.; Dou, T.; Gong, Y.; Zhang, Q.; Ren, Q.; Lu, X.; Deng, S. Adsorption Equilibria of CO_2, CH_4, N_2, O_2, and Ar on High Silica Zeolites. *Ind. Eng. Chem. Res.* **2001**, *56*, 4017–4023.

(20) Ridha, F. N.; Webley, P. A. Anomalous Henry's Law Behavior of Nitrogen and Carbon Dioxide Adsorption on Alkali-Exchanged Chabazite Zeolites. *Sep. Purif. Technol.* **2009**, *67*, 336–343.

(21) Pillai, R. S.; Peter, S. A.; Jasra, R. V. Adsorption of Carbon Dioxide, Methane, Nitrogen, Oxygen and Argon in NaETS-4. *Microporous Mesoporous Mater.* **2008**, *113*, 268–276.

(22) Shi, M.; Kim, J.; Sawada, J. A.; Lam, J.; Sarabadan, S.; Kuznicki, T. M.; Kuznicki, S. M. Production of Argon Free Oxygen by Adsorptive Air Separation on Ag-ETS-10. *AIChE J.* **2013**, *59*, 982–987.

(23) Shen, D.; Bülow, M.; Jale, S. R.; Fitch, F. R.; Ojo, A. F. Thermodynamics of Nitrogen and Oxygen Sorption on Zeolites LiLSX and CaA. *Micro. Meso. Mater.* **2001**, *48*, 211–217.

(24) Yang, R. T.; Chen, Y. D.; Peck, J. D.; Chen, N. Zeolites Containing Mixed Cations

for Air Separation by Weak Chemisorption-Assisted Adsorption. *Ind. Eng. Chem. Res.* **1996**, *35*, 3093–3099.

(25) Do, D. D. *Adsorption Analysis: Equilbria and Kinetics*; Imperial College Press: London, 1998.

(26) Valenzuela, D. P.; Myers, A. L. *Adsorption Equilibrium Data Handbook*; Prentice Hall: Englewood Cliffs, New Jersey, 1989.

CHAPTER III

HIGH PRESSURE EXCESS ISOTHERMS FOR ADSORPTION OF OXYGEN AND ARGON IN A CARBON MOLECULAR SIEVE

3.1 Introduction

The demand for pure oxygen is widespread. It is used to sustain life in the medical profession as well as in specialized applications such as space environments, scuba diving, and mountaineering. It is essential in the steel industry and contributes to the high temperatures of oxy-hydrogen and oxy-acetylene blow torches. In semiconductor fabrication, it is a component in the chemical vapor deposition of silicon dioxide, in diffusional operations for film growth, and in plasma etching and the plasma stripping of photoresistors. It is also used in a wide variety of other scientific, laboratory, commercial, and industrial applications.

Gas storage via adsorption is a targeted technology for future applications including methane and hydrogen storage in transportation vehicles. For these, the goal is to increase the volumetric capacity of a storage vessel and to increase the margin of safety in using pressurized gases by lowering pressures. NASA has an interest in generating pure oxygen from spacecraft cabin air for use in backpacks at high pressure for extravehicular activity.[1] The possibility exists to store oxygen in adsorptive media for this and in other applications such as for first responders.

Air separation to produce oxygen or nearly pure oxygen is generally performed by two methods. Cryogenic distillation is typically the source of pure oxygen, but it has high capital equipment requirements. While this is acceptable for large industrial applications, the demand for smaller sources is increasing. Adsorption processes, namely pressure-swing adsorption (PSA), vacuum-swing adsorption (VSA), and pressure-vacuum-swing adsorption (PVSA) find extensive application on more moderate scales including for medical oxygen

concentrators for home and portable use.

The generation of pure oxygen from air through adsorption is a difficult process. First, the nitrogen, carbon dioxide, and water vapor must be removed. This is commonly accomplished using zeolites in an equilibrium-based separation. There have been many such studies for PSA,[2–9] VSA,[10] and PVSA.[11] Nitrogen is adsorbed preferentially over oxygen on the zeolites. Argon is weakly adsorbed and remains with the oxygen, resulting in a product stream consisting of approximately 95% oxygen and 5% argon.

Then, the argon must be removed to produce a stream of purified oxygen. This is a more difficult separation than the one for oxygen and nitrogen. There have been studies based on zeolites,[6,10,12] but argon does not show an appreciable difference in isotherm loadings from oxygen. A carbon molecular sieve (CMS) separates gases based on differences in mass transfer rates through constricted pores. This adsorbent is well suited for the separation of oxygen and argon, as the mass transfer rate of argon is approximately 60 times slower than oxygen.[2]

There is a need for adsorption equilibrium data and descriptive equations to address design needs for separation and storage processes involving oxygen and argon at high pressures. While there have been prior equilibrium studies of oxygen and argon adsorption on CMS materials,[4,14–19] the pressures do not exceed 20 bar near room temperature (293 to 313 K) or 5 bar for a broader temperature range.

In this chapter, adsorption equilibria of oxygen and argon are reported for a CMS adsorbent, Shirasagi MSC-3R Type 172. The data were measured using a volumetric system designed for oxygen service and cover the temperature range of 25–100 °C and pressures as high as 100 bar. For oxygen, because of safety concerns, only the 25 °C isotherm was measured to 100 bar, with higher temperature isotherms measured to 12 bar. A high pressure nitrogen isotherm at 25 °C was also measured for comparison. The data are represented as excess adsorption isotherms and are analyzed using a traditional temperature-dependent

isotherm model, allowing for accurate prediction of adsorption loadings over wide ranges of temperatures and pressures. Finally, the data for oxygen, argon, and nitrogen are compared with loadings measured on other adsorbents, and the capability for adsorptive storage of oxygen is evaluated.

This chapter reports the highest pressure measurements to date of oxygen and argon isotherms on a carbon molecular sieve and is the first to examine the potential of the material for oxygen storage.

3.2 Materials and Methods

Materials

Shirasagi MSC-3R Type 172 carbon molecular sieve (lot M398) was supplied by Japan EnviroChemicals, Ltd. It is a coconut shell-based material and was in 1.8 mm pellet form. This material was chosen originally because of its ability to separate oxygen and argon on a rate-selective basis. All gases were ultrahigh purity (99.99%) and obtained from Airgas and Air Liquide.

Apparatus and Procedures

The volumetric apparatus and procedures used in this work have been described previously.[1] The adsorbent sample was degassed first using a Micromeritics ASAP 2020 porosimeter to determine the adsorbent mass. Approximately 4 g of sample was heated to 100 °C for 1 h under vacuum and then held at 300 °C for an additional 10 h under vacuum. After the dry sample mass was measured, the sample was loaded into the adsorbent bed of the volumetric apparatus, where it was regenerated again by heating at 300 °C under vacuum overnight. To determine the accessible volume on the sample side of the apparatus, helium expansions were performed at the highest measured isotherm temperature (100 °C) to reduce any potential helium adsorption effects. The sample was then regenerated a final time at

300 °C under vacuum overnight.

All of the data presented in this chapter were obtained using a single charge of CMS. It was regenerated in situ between isotherm measurements by heating to 200 °C under vacuum. Data were measured in the following order: (1) oxygen isotherms in order of increasing temperature to 12 bar, (2) argon isotherms in order of increasing temperature to 100 bar, (3) the 25 °C oxygen isotherm from 10 to 100 bar, and (4) the 25 °C nitrogen isotherm to 100 bar.

3.3 Results and Discussion

Measured Isotherms

Adsorption isotherms for oxygen and argon are shown in Figs. 3.1 and 3.2, respectively, with data for oxygen, argon, and nitrogen tabulated in Tables 3.1, 3.2, and 3.3. All adsorbed quantities are excess adsorption, calculated as in our previous study.[1] Compressibility factors for all gases were calculated using the commercial NIST REFPROP program.

Due to the pore constrictions introduced during manufacturing, rates of uptake on CMS materials are generally slow compared to adsorbents developed for equilibrium-based separations. Time constants for the rate of adsorption on Shirasagi MSC-3R Type 172, based on results of separate experiments performed using a frequency response method,[2] are about 2 minutes for oxygen, 1 hour for nitrogen, and 2 hours for argon; these correspond to times near the middle of an uptake curve. To approach adsorption equilibrium fairly closely, oxygen took hours and argon and nitrogen took about a day. We allowed at least 48 h for equilibration for all gases before recording any final measurements. For oxygen at low temperatures and pressures, we allowed up to 200 h for equilibration, because after a relatively rapid initial uptake and pressure reduction, a very slow exponential decline to a slightly lower pressure was observed (i.e., $\sim$1% drop in pressure between 48 and 200 h). This is possibly due to the ultimate transport of oxygen through tight pore constrictions,

which were too narrow for argon or nitrogen to pass through. It could also be due to a chemisorption process involving a small fraction of the carbon surface. We note that the aging of CMS adsorbents in oxygen containing environments has not been conclusively established, although it is recognized for cellulose-based CMS membranes;[19] studies have been directed toward stabilizing CMS adsorbents by hydrogen treatment, which may reduce significant oxygen chemisorption, should it occur.[20] Additional details about the approach to equilibrium of oxygen are provided in Appendix A. We also note that our data were reproducible after regeneration (see Fig. 3.1).

As shown in Figs. 3.1 and 3.2, the oxygen and argon isotherms are linear at pressures up to about 100 kPa. A line of slope unity is shown in the figures to emphasize this linearity. The decrease in slopes of the isotherms is easily apparent by a pressure of 10^3 kPa, with this decrease being smooth and gradual. Adsorbed-phase loadings for both oxygen and argon are near 10 mol/kg at 25 °C and 10^4 kPa, with argon having a slightly higher loading. The oxygen isotherms appear to be more temperature sensitive than those for argon, as the loadings for oxygen decrease more with increasing temperature.

Isotherms for oxygen, argon, and nitrogen at 25 °C are compared in Fig. 3.3. The three gases have similar loadings across the entire pressure range, with argon having slightly higher loadings than oxygen or nitrogen. Also, all three gases have nearly linear isotherms up to 100 kPa. This linearity suggests that there is little interaction of molecules in the adsorbed phase, so adsorbed-phase concentrations in a mixture of the gases should be described reasonably well by partial pressures and pure gas isotherms.

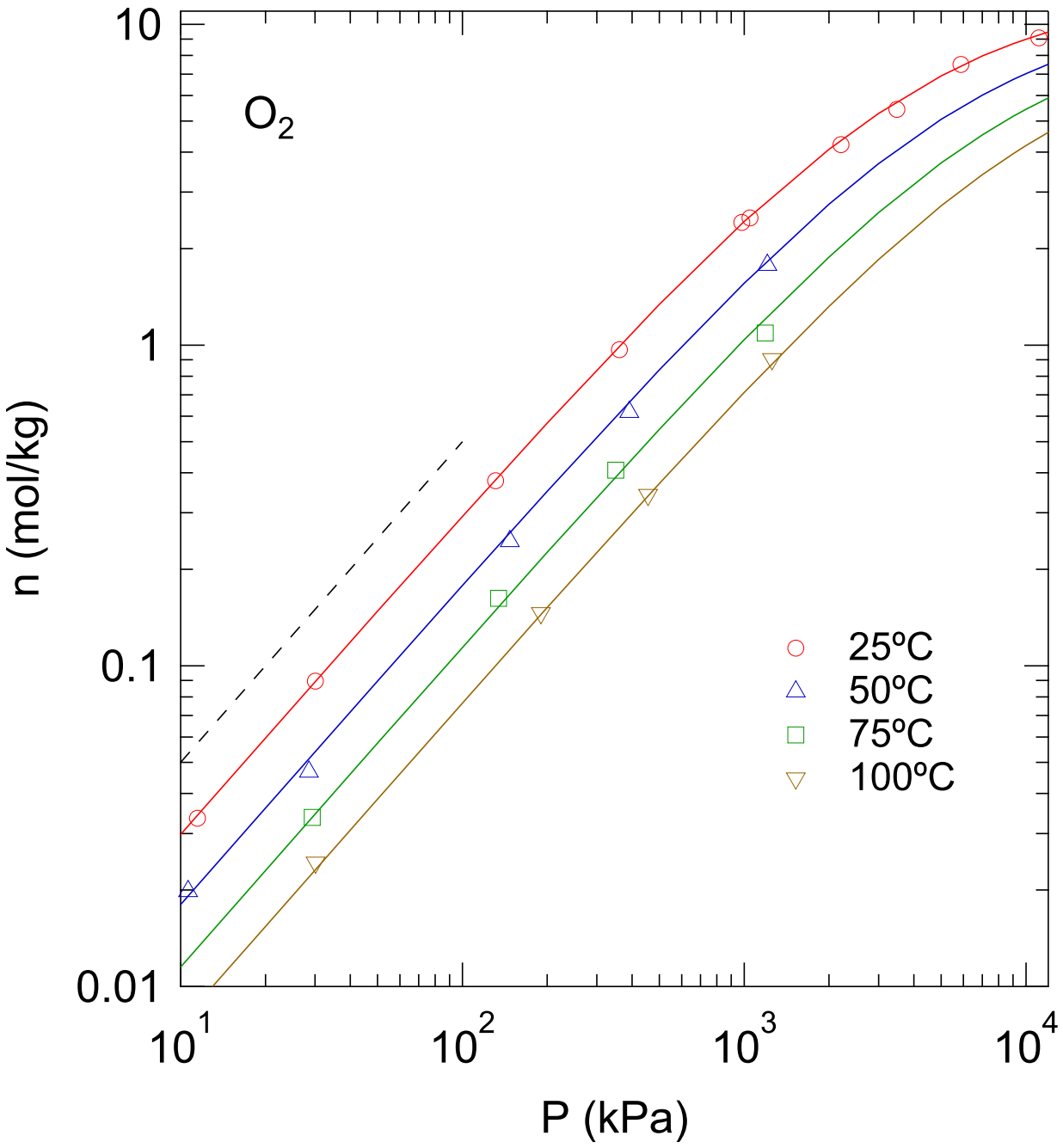

Figure 3.1: Excess adsorption isotherms for oxygen on Shirasagi MSC-3R Type 172. Solid curves are multi-temperature Toth model. Dashed line has a slope of unity. Additional data at lower pressures are included in Table 3.1. Data at 25 °C near 10^3 kPa are reproduced following regeneration.

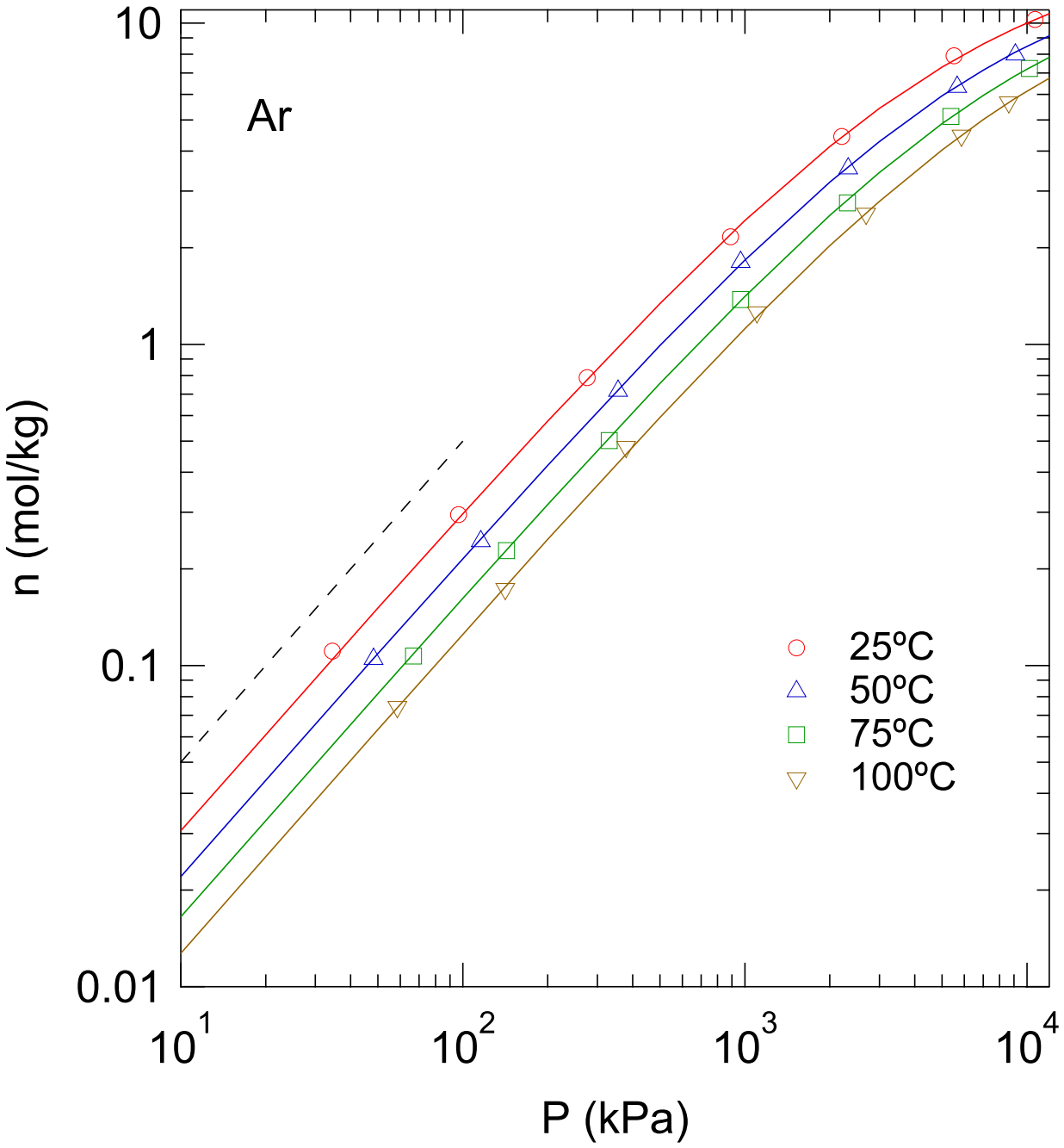

Figure 3.2: Excess adsorption isotherms for argon on Shirasagi MSC-3R Type 172. Solid curves are multi-temperature Toth model. Dashed line has a slope of unity.

Table 3.1: Oxygen excess adsorption data on MSC-3R Type 172

25 °C		50 °C		75 °C		100 °C	
P (kPa)	n (mol/kg)	P (kPa)	n (mol/kg)	P (kPa)	n (mol/kg)	P (kPa)	n (mol/kg)
7.01×10^{-1}	1.96×10^{-3}	8.09×10^{-1}	1.12×10^{-3}	4.46×10^{-1}	4.28×10^{-4}	5.51×10^{-1}	3.76×10^{-4}
9.82×10^{-1}	2.74×10^{-3}	1.48	2.55×10^{-3}	1.14	1.26×10^{-3}	1.29	9.15×10^{-4}
1.58	4.39×10^{-3}	3.20	5.76×10^{-3}	3.20	3.44×10^{-3}	3.60	2.36×10^{-3}
3.81	1.10×10^{-2}	10.6	1.98×10^{-2}	8.30	9.15×10^{-3}	9.61	6.59×10^{-3}
11.5	3.35×10^{-2}	28.5	4.67×10^{-2}	29.3	3.37×10^{-2}	30.1	2.44×10^{-2}
30.1	8.96×10^{-2}	147	2.45×10^{-1}	134	1.62×10^{-1}	190	1.46×10^{-1}
131	3.78×10^{-1}	391	6.19×10^{-1}	350	4.07×10^{-1}	456	3.41×10^{-1}
360	9.68×10^{-1}	1210	1.79	1190	1.09	1260	9.05×10^{-1}
1049	2.49						
981	2.42						
2210	4.22						
3480	5.43						
5870	7.49						
11100	9.08						

Table 3.2: Argon excess adsorption data on MSC-3R Type 172

25 °C		50 °C		75 °C		100 °C	
P (kPa)	n (mol/kg)	P (kPa)	n (mol/kg)	P (kPa)	n (mol/kg)	P (kPa)	n (mol/kg)
34.5	1.11×10^{-1}	48.3	1.05×10^{-1}	66.9	1.07×10^{-1}	58.6	7.43×10^{-2}
96.5	2.95×10^{-1}	116	2.44×10^{-1}	143	2.28×10^{-1}	141	1.73×10^{-1}
276	7.88×10^{-1}	355	7.17×10^{-1}	330	5.02×10^{-1}	379	4.80×10^{-1}
889	2.16	965	1.81	965	1.38	1100	1.26
2210	4.44	2320	3.53	2310	2.76	2690	2.55
5520	7.92	5650	6.34	5380	5.12	5860	4.46
10700	10.3	9100	7.99	10200	7.23	8620	5.67

Table 3.3: Nitrogen excess adsorption data on MSC-3R Type 172

25 °C	
P (kPa)	n (mol/kg)
44.8	1.24×10^{-1}
117	3.13×10^{-1}
317	7.47×10^{-1}
965	1.89
2320	3.73
5520	6.64
11000	8.54

Isotherm Model

Adsorption equilibrium models can provide accurate descriptions of the temperature and pressure dependence of data over wide ranges. Many such models are available, and the temperature dependent Toth equation[21] is adopted here. The Toth isotherm is

$$n = \frac{n_s b P}{[1 + (bP)^t]^{(1/t)}} \tag{3.1}$$

where n_s is the saturation loading, b describes the adsorption affinity, and t represents adsorbent homogeneity. Temperature dependences are given by

$$n_s = n_0 \exp\left[\chi\left(1 - \frac{T}{T_0}\right)\right] \tag{3.2}$$

$$b = b_0 \exp\left[\frac{Q}{RT_0}\left(\frac{T_0}{T} - 1\right)\right] \tag{3.3}$$

$$t = t_0 + \alpha\left(1 - \frac{T_0}{T}\right) \tag{3.4}$$

where χ and α are empirical parameters, and Q is the isosteric heat of adsorption in the Henry's law limit. The nitrogen isotherm was modeled using the basic Toth isotherm given by eq 3.1. Using $T_0 = 273.15$ K as the reference temperature, the Toth parameters for all three gases were obtained via a least squares analysis and are given in Table 3.4. Solid curves using the parameters for oxygen and argon are plotted in Figs. 3.1 and 3.2, and they describe the data well.

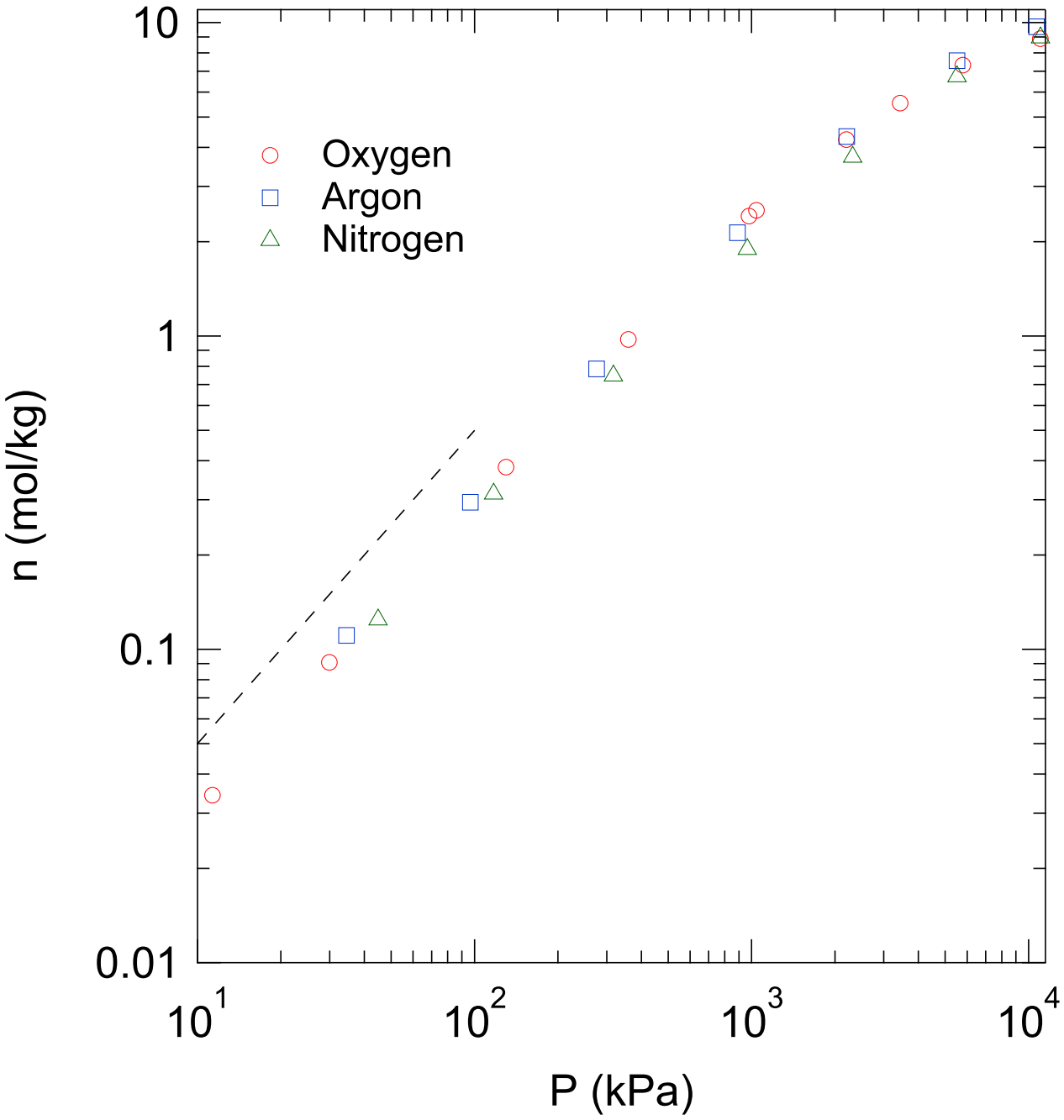

Figure 3.3: Excess adsorption isotherms for oxygen, argon, and nitrogen on Shirasagi MSC-3R Type 172 at 25 °C. Dashed line has a slope of unity.

Table 3.4: Model parameters for multi-temperature Toth equation

	n_0 mol/kg	χ	b_0 kPa^{-1}	$Q/(RT_0)$	t_0	α
Oxygen	14.4	1.23	3.69×10^{-2}	5.52	1.00	1.89×10^{-2}
Argon	18.5	0.589	2.43×10^{-2}	3.89	0.858	1.38×10^{-2}
Nitrogen*	15.8		1.74×10^{-2}		0.778	

*Nitrogen parameters are n_s, b, and t as shown in eq 3.1.

Isosteric Heat of Adsorption

The isosteric heat of adsorption for a pure component can be calculated using the Clausius-Clapeyron equation from isotherms at different temperatures using

$$\Delta H_{ads} = zRT^2 \left.\frac{\partial(\ln P)}{\partial T}\right|_n \tag{3.5}$$

For the Toth isotherm, the isosteric heat of adsorption with $z = 1$ is[21]

$$\Delta H_{ads} = Q - \frac{\alpha RT_0}{t}\left\{\ln(bP) - \left[1+(bP)^t\right]\ln\left[\frac{bP}{(1+(bP)^t)^{1/t}}\right]\right\} \tag{3.6}$$

Isosteric heats for oxygen and argon at 25 and 100 °C on MSC-3R Type 172 are shown as a function of loading in Fig. 3.4. They are only weakly temperature dependent over our range of interest. The isosteric heats are constant over the linear range of the isotherms and decrease slightly as the slopes of the isotherms decrease. We obtain isosteric heats at zero loading of approximately 12.5 kJ/mol for oxygen and 8.9 kJ/mol for argon. These agree reasonably well with respective predicted values of 10.7 kJ/mol and 9.0 kJ/mol,[15] although measured values for other carbon molecular sieves are higher, 16 kJ/mol for oxygen[22] and 18 kJ/mol for argon.[15]

Comparison with Other Adsorbents

Adsorption isotherms for oxygen on various adsorbents at 25 °C are shown in Fig. 3.5. Shirasagi MSC-3R Type 172 gives high loadings, similar to those of a superactivated car-

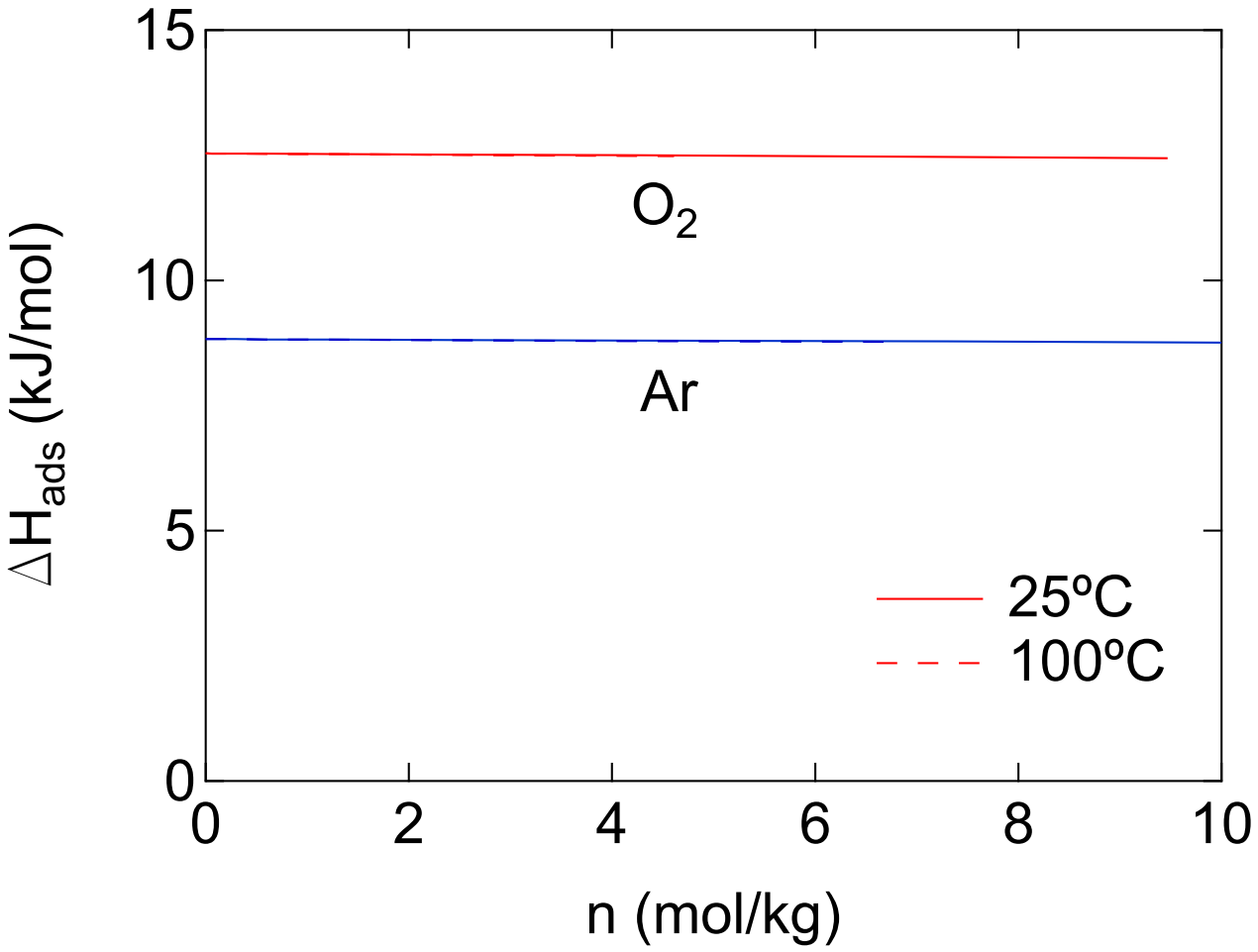

Figure 3.4: Isosteric heat of adsorption as a function of loading on Shirasagi MSC-3R Type 172 at 25 and 100 °C. Curves overlap for each gas.

bon,[23] and the highest at 10^4 kPa. The Takeda 3A CMS[18] and BPL activated carbon give similar loadings that are somewhat lower at high pressures than MSC-3R Type 172 and the superactivated carbon. The 13X zeolite[1] and the titanosilicates[24,25] give comparatively low loadings.

Figure 3.6 shows the 25 °C adsorption isotherm for argon on MSC-3R Type 172 compared to 25 °C argon isotherms on other adsorbents. MSC-3R Type 172 gives the highest loadings at high pressures. The 5A zeolite[26] and BPL activated carbon give similar loadings, with both having higher loadings than Takeda 3A CMS. MSC-3R Type 172 has higher isotherm slopes than Takeda 3A CMS.[18] The titanosilicates[24,25] give comparatively low loadings, which are similar to those for oxygen on these adsorbents.

Figure 3.7 shows 25 °C adsorption isotherms for nitrogen on various adsorbents. MSC-3R Type 172 followed closely by BPL activated carbon give the highest loadings for isotherms measured to high pressure. The isotherm for 13X zeolite,[1] also measured in our laboratory, and Takeda 3A CMS[18] give similar loadings for nitrogen. The capacity of MSC-3R Type 172 is three times that of 13X zeolite at 10^4 kPa. The capacities of the titanosilicates[24,25] at high pressure are not apparent.

Although both are carbons, there are notable differences between MSC-3R Type 172 and BPL. BPL is a coal-based carbon with a surface area of approximately 1200 m^2/g and a median pore width of approximately 12 Å but depends on the method used in porosity analysis.[29] The MSC-3R is a coconut shell-based carbon with a surface area of approximately 750 m^2/g and two average pore widths of 3.5 and 6.0 Å, based on a similar material.[19] Although BPL has a higher surface area, the reduced average pore size in MSC-3R created during production results in higher excess adsorbate densities at high pressures.

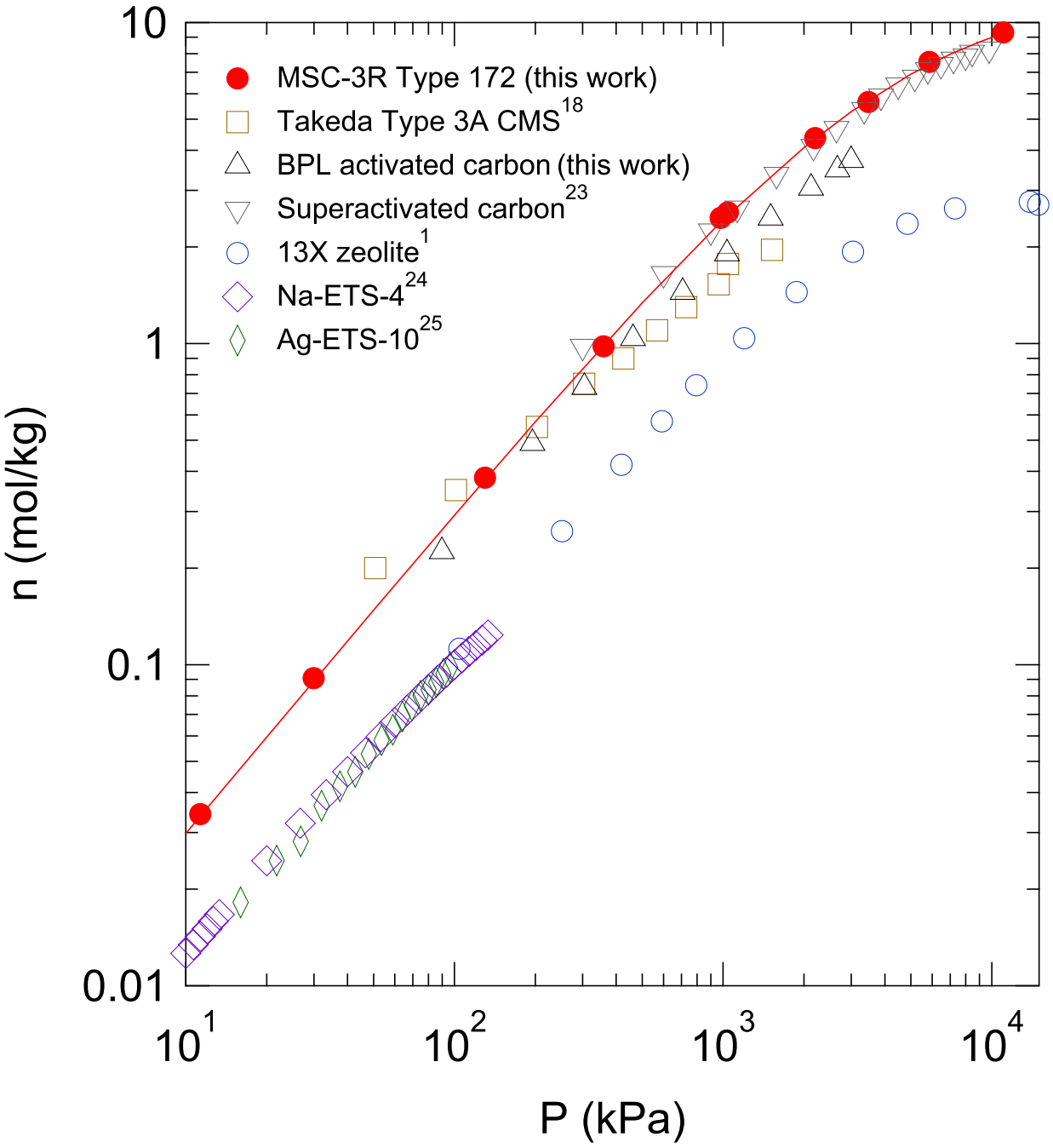

Figure 3.5: Adsorption isotherms for oxygen on several adsorbents at 25 °C. Solid curve is plot of eq 3.1 with parameters for oxygen.

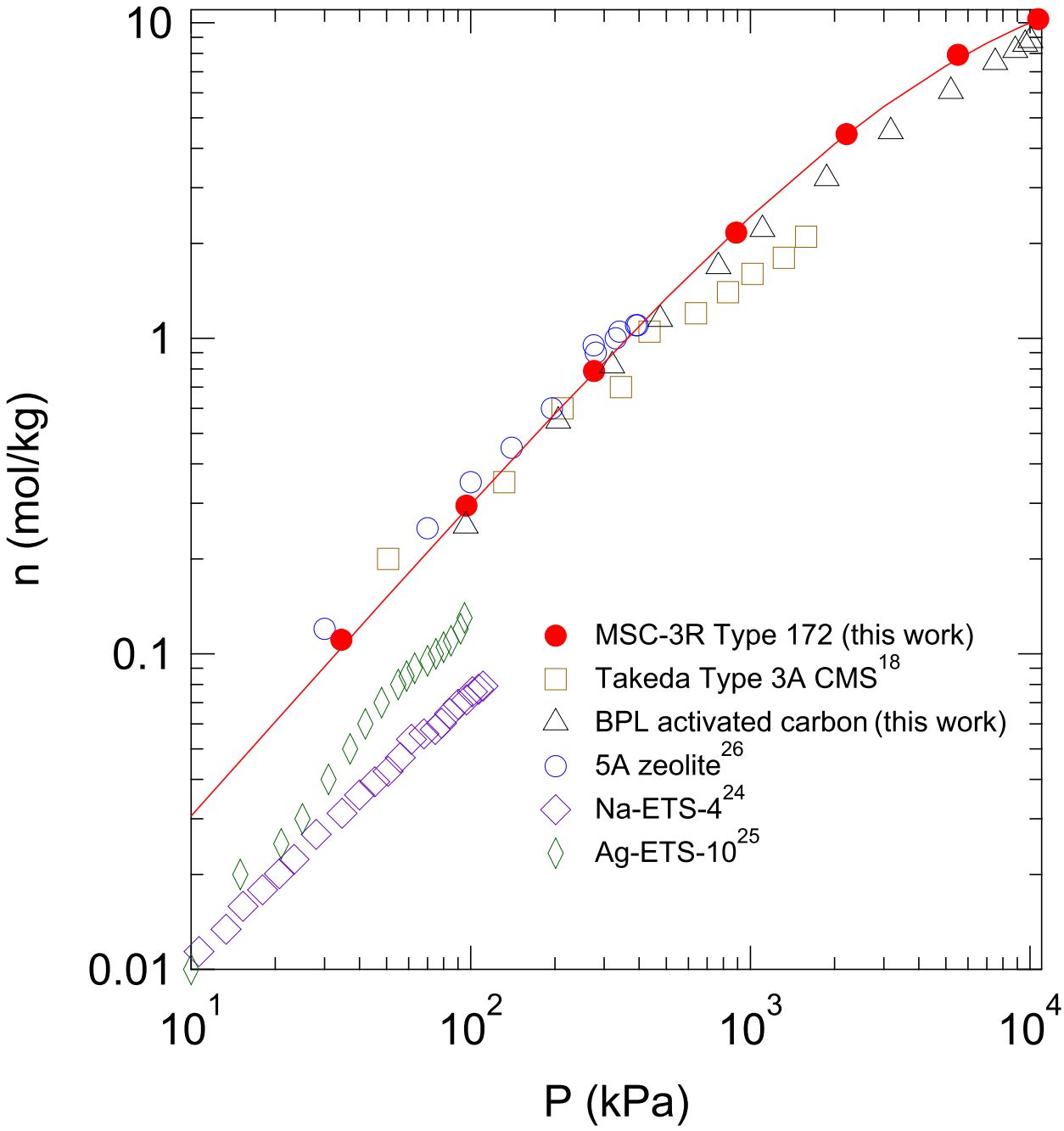

Figure 3.6: Adsorption isotherms for argon on several adsorbents at 25 °C. Solid curve is plot of eq 3.1 with parameters for argon.

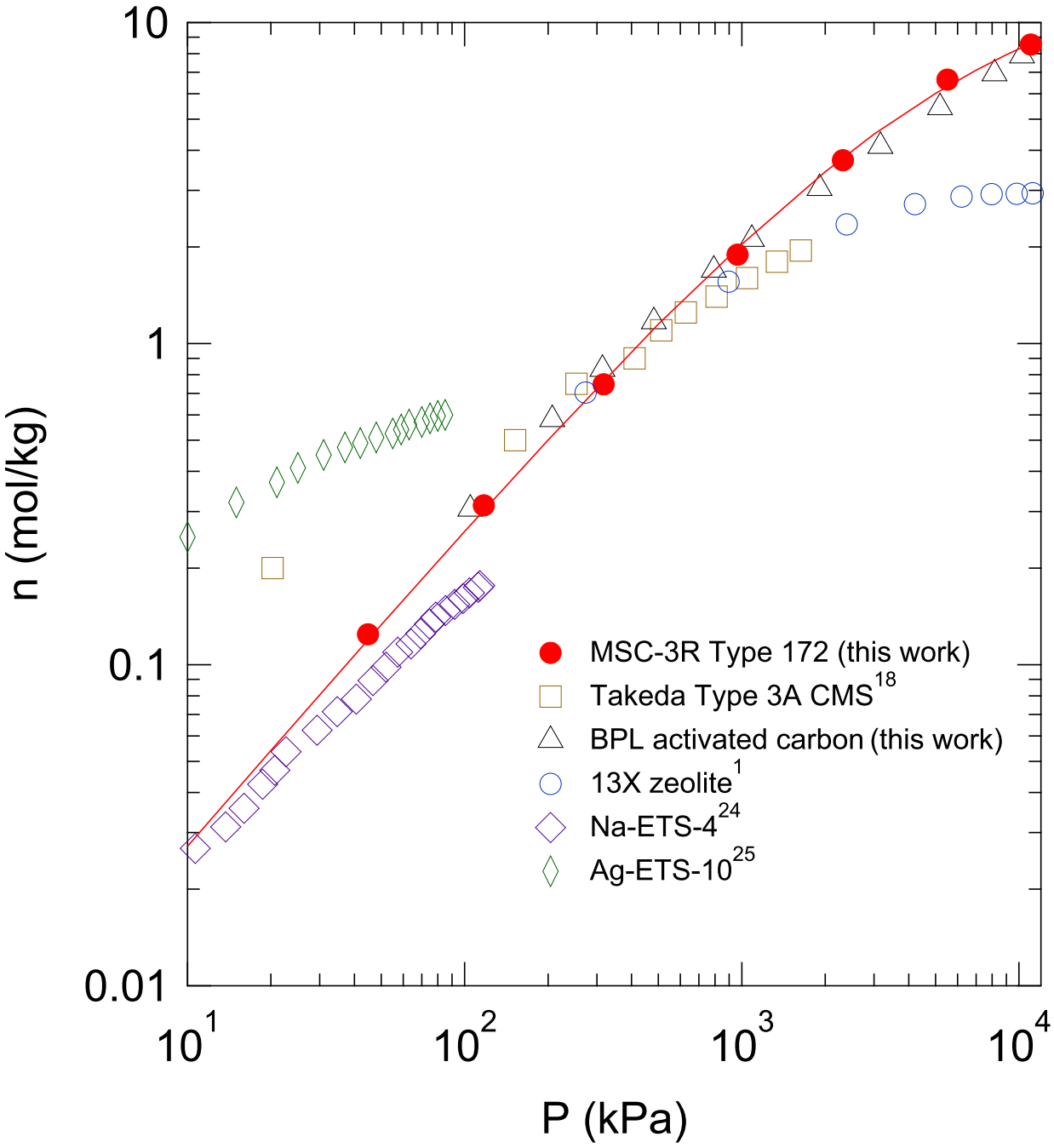

Figure 3.7: Adsorption isotherms for nitrogen on several adsorbents at 25 °C. Solid curve is plot of eq 3.1 with parameters for nitrogen.

Adsorptive Storage of Oxygen

The possibility of using an adsorbent for gas storage can be explored using an adsorption isotherm and the physical properties of the adsorbent. The total volumetric capacity for a mass of adsorbent is given by[27]

$$\rho_{tot} = \rho_b n + \epsilon' c \tag{3.7}$$

with

$$\epsilon' = \epsilon + \chi(1 - \epsilon) \tag{3.8}$$

where ρ_b is the bulk density of the packing, ϵ' is total voidage (with contributions ϵ from packing interstices and χ from total porosity), and $c = P/(zRT)$ is the gas molar density.

Figure 3.8 shows two curves for 25 °C: the oxygen density in an unpacked vessel and the oxygen density in a vessel packed with MSC-3R Type 172 CMS. We used $\rho_b = 705$ kg/m^3, $\epsilon = 0.35$, and $\chi = 0.46$; the value of ρ_b corresponds to the center of the manufacturer's range (680–730 kg/m^3),[28] and the value of χ corresponds to a similar material (Shirasagi MSC-3K Type 162).[19] Oxygen gas is nearly ideal over the entire pressure range, with the compressibility factor reaching 0.95 at 10^4 kPa. Over the linear range of the isotherm, the packed vessel contains 5.3 times the amount of oxygen as an unpacked vessel. At 10^3 kPa, the packed vessel contains about 4.3 times, and at 10^4 kPa it contains about 43% more. Expressed another way, for vessels of the same volume, vessels packed with adsorbent at 230 kPa and 4650 kPa would contain the same amount of oxygen as unpacked vessels at 10^3 kPa and 10^4 kPa, respectively.

The performance of MSC-3R Type 172 CMS for oxygen storage on a volumetric basis will exceed that of a superactivated carbon. Although the isotherms on a mass of adsorbent basis are similar on the two adsorbents, the CMS is denser than the superactivated carbon, and thus gives a much larger contribution from the first term on the right side of eq 3.7. For example, the particle density of AX-21 superactivated carbon[29] is 700 g/cm^3, which

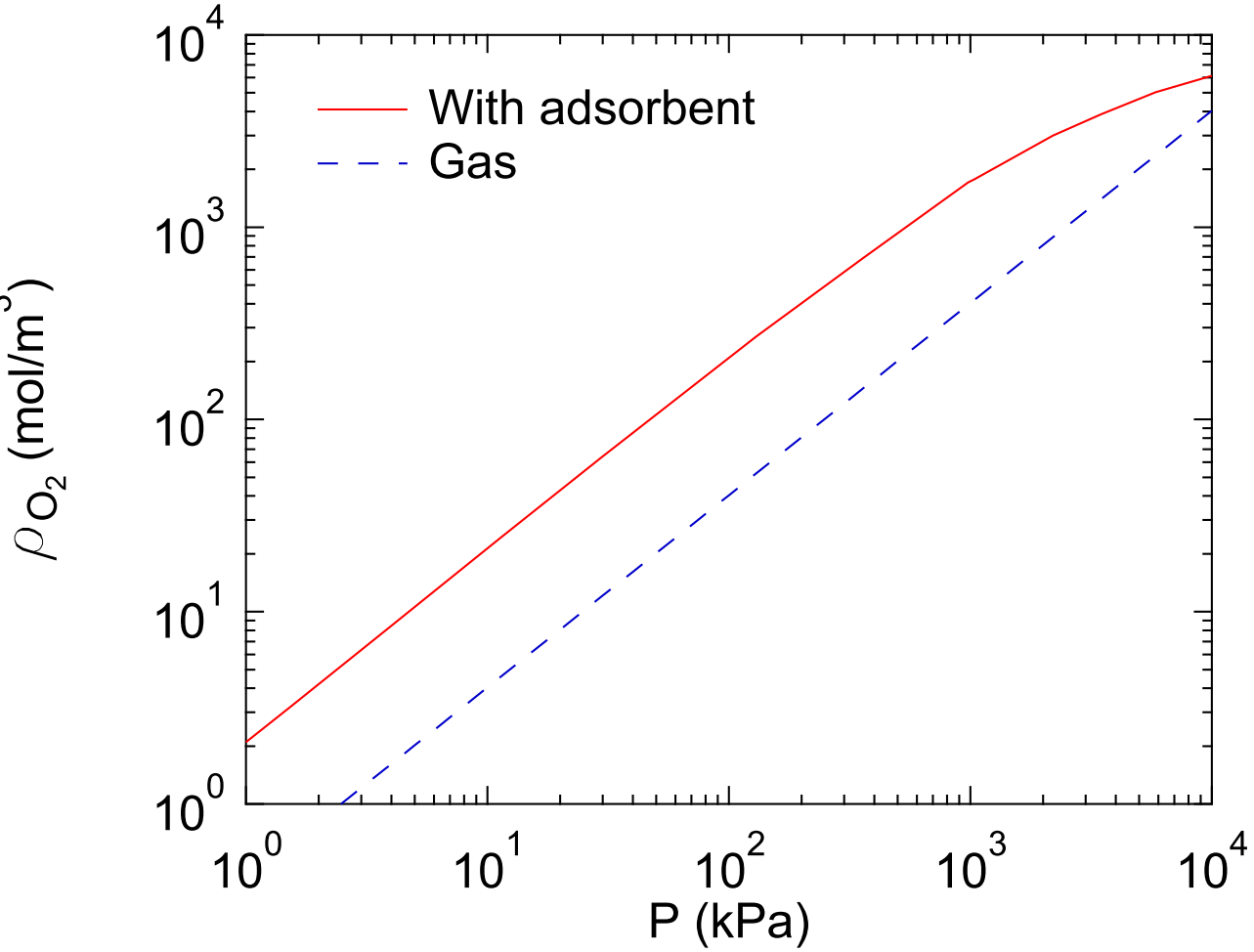

Figure 3.8: Oxygen storage densities with Shirasagi MSC-3R Type 172 at 25 °C compared to bulk gas.

corresponds to a bulk density of 455 kg/m^3 using $\epsilon = 0.35$.

3.4 Conclusions

Surface excess isotherms for oxygen and argon adsorbed on Shirasagi MSC-3R Type 172 carbon molecular sieve over the temperature range 25–100 °C and pressures up to 10^4 kPa have been measured. These are the highest pressure oxygen and argon isotherms reported for a carbon molecular sieve. Excess loadings for oxygen and argon approach 10 mol/kg at 10^4 kPa and 25 °C. Oxygen, argon, and nitrogen isotherms have similar loadings and linear slopes up to 100 kPa at 25 °C.

The measured isotherm data have been analyzed using traditional methods. The oxygen and argon data were modeled with a multi-temperature Toth equation, while the nitrogen data were modeled with the classic Toth isotherm. The isosteric heats of adsorption were determined to be 12.5 kJ/mol for oxygen and 8.9 kJ/mol for argon over the linear ranges of the 25 °C isotherms.

The isotherms for oxygen, argon, and nitrogen adsorption on Shirasagi MSC-3R Type 172 have been compared to isotherms in the literature for these gases on other adsorbents. The CMS has the highest loadings and isotherm slopes at 10^4 kPa, including somewhat higher loadings than a superactivated carbon.

The high capacities of the adsorbent suggest potential as an adsorbent in the production and storage of pure oxygen. Calculations performed for oxygen storage indicate that volumetric density is increased over bulk gas by a factor of more than 5 at low pressure, dropping to 4.3 at 10^3 kPa and 1.43 at 10^4 kPa. While less important in a separation process, as a precautionary measure for storage, the potential chemisorption of oxygen on a carbon surface and the possible creation of gaseous impurities need further study, particularly if the oxygen is to be used for breathing.

References

(1) Wang Y, Helvensteijn B, Nizamidin N, Erion, AM, Steiner LA, Mulloth LM, Luna B, LeVan MD. High pressure excess isotherms for adsorption of oxygen and nitrogen in zeolites. Langmuir 2011;27:10648–10656.

(2) Jee J, Kim M, Lee C. Pressure swing adsorption processes to purify oxygen using a carbon molecular sieve. Chem Eng Sci 2005;60:869–882.

(3) Kim M, Jee J, Bae YS, Lee C. Parametric study of pressure swing adsorption process to purify oxygen using carbon molecular sieve. Ind Eng Chem Res 2005;44:7208–7217.

(4) Jin X, Malek A, Farooq S. Production of argon from an oxygen-argon mixture by pressure swing adsorption. Ind Eng Chem Res 2006;45:5775–5787.

(5) Reynolds SP, Ebner AD, Ritter JA. Enriching PSA cycle for the production of nitrogen from air. Ind Eng Chem Res 2006;45:3256–3264.

(6) Santos JC, Cruz P, Regala T, Magalhães FD, Mendes A. High-purity oxygen production by pressure swing adsorption. Ind Eng Chem Res 2007;46:591–599.

(7) Kupiec K, Rakoczy J, Lalik E. Modeling of PSA separation process including friction pressure drop in adsorbent bed. Chem Eng Process 2009;48:1199–1211.

(8) Mofarahi M, Towfighi J, Fathi L. Oxygen separation from air by four-bed pressure swing adsorption. Ind Eng Chem Res 2009;48:5439–5444.

(9) Rama Rao V, Farooq S, Krantz WB, Design of a two-step pulsed pressure-swing adsorption-based oxygen concentrator. AIChE J 2009;56:354–370.

(10) Bunder Z, Dula J, Podstawa W, Gawdzik A. Study and modelling of the vacuum swing

adsorption (VSA) process employed in the production of oxygen. Trans Inst Chem Eng 1999;77:405–412.

(11) Jee J, Lee S, Kim M, Lee C. Three-bed PVSA process for high-purity O_2 generation from ambient air. AIChE J 2005;51:2988–2999.

(12) Peter SA, Sebastian J, Jasra RV. Adsorption of nitrogen, oxygen, and argon in mono-, di-, and trivalent cation-exchanged zeolite mordenite. Ind Eng Chem Res 2005;44:6856–6864.

(13) Giesy TJ, LeVan MD. Mass transfer rates of oxygen, nitrogen, and argon in carbon molecular sieves determined by pressure-swing frequency response. Chem Eng Sci 2013;90:250–257.

(14) Reid CR, O'koye IP, Thomas KM. Adsorption of gases on carbon molecular sieves used for air separation. Spherical adsorptives as probes for kinetic selectivity. Langmuir 1998;14:2415–2425.

(15) Rutherford SW, Coons JE. Adsorption equilibrium and transport kinetics for a range of probe gases in Takeda 3A carbon molecular sieve. J Colloid Interf Sci 2005;284:432–439.

(16) Ma YH, Sun W, Bhandarkar M, Wang J. Adsorption and diffusion of nitrogen, oxygen, argon, and methane in molecular sieve carbon at elevated pressures. Separ Technol 1991;1:90–98.

(17) Rege S, Yang RT. Kinetic separation of oxygen and argon using molecular sieve carbon. Adsorption 2000;6:15–22.

(18) Bae YS, Lee CH. Sorption kinetics of eight gases on a carbon molecular sieve at elevated pressure. Carbon 2005;43:95–107.

(19) Campo MC, Magalhães FD, Mendes A. Comparative study between a CMS membrane and a CMS adsorbent: Part I–Morphology, adsorption equilibrium and kinetics. J Membrane Sci 2010;346:15–25.

(20) Verma SK, Walker Jr PL. Carbon molecular sieves with stable hydrophobic surfaces. Carbon 1992;30:837–844.

(21) Do DD. Adsorption analysis: equilbria and kinetics. London: Imperial College Press. 1998.

(22) Chen YD, Yang RT, Uawithya P. Diffusion of oxygen, nitrogen and their mixtures in carbon molecular sieve. AIChE J 1994;40:577–585.

(23) Zhou Y, Wei L, Yang J, Sun Y, Zhou L. Adsorption of oxygen on superactivated carbon. J Chem Eng Data 2005;50:1068–1072.

(24) Pillai RS, Peter SA, Jasra RV. Adsorption of carbon dioxide, methane, nitrogen, oxygen and argon in NaETS-4. Microporous Mesoporous Mater 2008;113:268–276.

(25) Shi M, Kim J, Sawads JA, Lam J, Sarabadan S, Muznicki TM, Kuznicki SM. Production of argon free oxygen by adsorptive air separation on Ag-ETS-10. AIChE J 2012;59:982–987.

(26) Miller GW, Knaebel KS, Ikels KG. Equilibria of nitrogen, oxygen, argon, and air in molecular sieve 5A. AIChE J 1987;33:194–201.

(27) LeVan MD, Carta G. Adsorption and Ion Exchange. In: Green DW, editor. Perry's chemical engineers' handbook, 8th edn, New York; McGraw-Hill 2008.

(28) JEChem Shirasagi technical information, Data sheet no. M008, September 2012.

(29) Dailly A, Poirier E. Evaluation of an industrial pilot scale densified MOF-177 adsorbent as an on-board hydrogen storage medium. Energy Environ Sci 2011;4:3527–3534.

CHAPTER IV

ADSORPTION OF CHAIN MOLECULES IN SLIT-SHAPED PORES: DEVELOPMENT OF A SAFT-FMT-DFT APPROACH

4.1 Introduction

The use of molecular simulation, the development of accurate models, and the comparison of theoretical predictions with experimental results help to advance our understanding of adsorption and its application. The introduction of density functional theory (DFT) to model inhomogeneous fluids represented a significant advance towards understanding confined fluid behavior and was encouraged by the desire to model a variety of phase transitions accurately.

Many versions of classical DFT have been proposed to calculate thermodynamic properties of systems of varying complexity. In an early treatment, Tarazona[1,2] introduced a weighted density approximation for spherical molecules in which a power series expansion in density was used to describe the direct correlation function. This approach has been applied to many problems in adsorption.[1,4–10] Our development is based instead on the application of fundamental measure theory.

Fundamental measure theory (FMT) was developed by Rosenfeld[20,21] and later improved upon by Roth *et al.*[13] as an extension of scaled particle theory for inhomogeneous fluids. However, Roth's advancement of FMT could not satisfy one of the central equations of the Rosenfeld FMT; specifically, the theory was not consistent with the scaled particle theory differential equation in the bulk.[15,22] This led to an improvement by Hansen-Goos and Roth,[22] which corrected the inconsistency. FMT uses simple geometric factors that describe the direct correlation function, and it has been used for a variety of applications in phase transitions[6,16] and adsorption.[6,16–19] Reviews[15,20,21] of the development of DFT for

spherical molecules are available for both the weighted density approximation and FMT. Evans[21] elaborates on the success of incorporating Rosenfeld's FMT into a DFT, including for mixtures of hard spheres.

There is much interest in expanding the use of DFT to systems of more complex molecules, such as chain fluids and polymers. In order to predict the properties of such molecules, the pioneering work by Wertheim[14–17] on thermodynamic perturbation theory was utilized to develop the statistical associating fluid theory (SAFT) equation of state.

In the SAFT approach, a fluid is described by a chain of tangentially bonded monomer segments that interact via dispersion and association interactions. The free energy is obtained from a sum of the different contributions that account for the monomer-monomer interaction, chain formation, and intermolecular association. Since the SAFT EOS has a firm basis in statistical mechanical perturbation theory for well-defined molecular models, systematic improvement (e.g., by improved expressions for monomer free energy and structure) and extension of the theory (e.g., by considering new monomer fluids, bonding schemes and association interactions) is possible by comparing the theoretical predictions with computer simulation results on the same molecular model.[26–29] Due to its role in improving and validating the theory, the importance of having an underlying molecular model in contrast to engineering equations of state cannot be overemphasized. In comparing with experimental data, it is important to be aware of the error inherent in the theory, as revealed by comparison with computer simulation results, before attempting to estimate the intermolecular parameters. This invaluable advantage over empirical EOSs has resulted in many extensions and variations of the original SAFT expressions, which essentially correspond to different choices for the monomer fluid and different theoretical approaches to the calculation of the monomer free energy and structure. The simplest SAFT approach describes associating chains of hard-sphere segments with the dispersion interactions described at the mean-field level.[30,31] At a similar level of theory is the most extensively applied version of SAFT, that

of Huang and Radosz (SAFT-HR),[32] which has been used to correlate the phase behavior of a wide range of fluid systems. Comparisons with SAFT-HR are often provided when a new version of SAFT is developed to demonstrate the improved ability of a new equation; however, direct and meaningful comparisons between the more recent "second-generation" SAFT equations (namely, soft-SAFT,[33,34] SAFT-VR,[3] and PC-SAFT[36]) are more rare. From the limited number of studies that have performed such comparisons, it is clear that any one version is not superior over the others in general terms.[37–42] A recent review by McCabe and Galindo[43] provides a thorough discussion of the various forms of SAFT and the many systems to which they have been applied. Of particular relevance to this work is SAFT-VR,[3] which keeps a more formal link with the molecular model than other versions of SAFT and as such can be more easily rigorously extended to study more complex molecular models.[44–47] SAFT-VR has been applied to the study the phase behavior of a wide range of fluids, though of particular relevance to the current work are the studies of short alkanes through to polymers.[26,27,39,48–50]

Several molecular theory-based equations of state, including multiple versions of SAFT, have been combined with DFT by using modified versions of Rosenfeld's FMT. Among those most relevant to this work, Yethiraj and Woodward[51] and Forsman and Woodward[52] developed a DFT for square-well chains in hard wall slit pores. Their approach combined the generalized Flory equation of state with a DFT based on a weighted density approximation for the free energy functional. Jackson and coworkers[53,54] developed a SAFT-based DFT by combining SAFT-HS,[30,31] which describes tangentially bonded chain molecules that interact via a mean field dispersion term, with a local density approximation to model the vapor-liquid interface of associating fluids. Only qualitative agreement with experimental surface tension data was found, and in subsequent work, SAFT-HS was replaced by the SAFT-VR equation resulting in more accurate predictions of the surface tension due to the more accurate description of the bulk properties.[55–59] Yu and Wu[4,60] and Yu et al.[62] combined

the first-order thermodynamic perturbation theory of Wertheim[14,15] for hard-sphere chains with a modified version of Rosenfeld's FMT to predict the adsorption behavior of mixtures of hard polymeric fluids. Bryk *et al.*[63] later combined Roth's version of FMT and SAFT for tangentially bonded Lennard-Jones (LJ) chains to study the vapor-liquid interface of associating LJ chains as well as their adsorption in slit pores. Ye *et al.*[64,65] used SAFT-VR as the input to a DFT similar to that of Yethiraj and Woodward[51] to describe chain molecules and attractive wall potentials inside slit pores. Chapman and coworkers developed interfacial SAFT (iSAFT) by combining a DFT based on Rosenfeld's FMT for monomers with bulk fluid properties obtained from SAFT to model bulk and interfacial adsorption properties.[18,19]

In this chapter, we extend the theory of Yu and Wu[4] to treat adsorption on flat surfaces and in slit-shaped pores. We develop a DFT using a modified version of Rosenfeld's FMT and a version of SAFT based on SAFT-VR to treat the adsorption of confined chain molecules. For the chain fluids, we use a perturbation analysis for attractive terms out to second order, rather than assume a mean field. We compare our results with predictions of Monte Carlo simulations of hard-sphere chains near hard walls and chains with attractive potentials in the presence of hard walls and attractive walls. We then compare results for attractive chains in slit pores with a square-well attractive wall potential and a Lennard-Jones attractive wall potential. Finally, we use the theory to predict density profiles in full pores with interactions described by a 10-4 potential.

4.2 Theory

The treatment developed here constructs a DFT using a version of SAFT based on the SAFT-VR approach for the bulk fluid thermodynamics.[3] The DFT is implemented for inhomogeneous fluids near plane walls and flat pore walls through the introduction of FMT for hard sphere and hard sphere chain interactions to permit the use of SAFT to describe

the attractive potential. In doing so, SAFT is transformed from a method for treatment of a homogeneous fluid in the bulk to a method for analysis of an inhomogeneous fluid near a surface. First and second order perturbation terms for the attractive potential originate in SAFT-VR, but it is necessary to recast them for the inhomogeneous fluid. Below we outline the main expressions of the SAFT-FMT-DFT approach developed for confined and bulk fluids and provide additional details in Appendix B.

Density functional theory is used to calculate the density profile that minimizes the grand potential function $\Omega[\rho_m(\mathbf{R})]$, where $\rho_m(\mathbf{R})$ is the density profile of a chain molecule as a function of segment position, i.e. $\mathbf{R} \equiv (\mathbf{r}_1, \mathbf{r}_2, \cdots, \mathbf{r}_m)$, and m is the number of segments in the chain. Minimization is performed by setting the functional derivative of the grand potential with respect to density equal to zero to obtain $\rho_m(\mathbf{R})$. The grand potential is calculated from

$$\Omega[\rho_m(\mathbf{R})] = F[\rho_m(\mathbf{R})] + \int \rho_m(\mathbf{R})[V_{ext}(\mathbf{R}) - \mu]\, d\mathbf{R} \tag{4.1}$$

where $F[\rho_m(\mathbf{R})]$ is the Helmholtz free energy, μ is the chemical potential for the chain molecule calculated from the SAFT equation of state in the bulk (see appendix), and $V_{ext}(\mathbf{R})$ is the external potential.

The Helmholtz free energy is calculated from an ideal term and excess terms. In the general formulation of SAFT, the excess terms describe hard sphere repulsion, attractive interactions, and chain connectivity. Since we are incorporating both first and second order perturbation terms, we write the Helmholtz free energy and the chemical potential from SAFT as

$$F = F_{id} + F_{hs} + F_1 + F_2 + F_{chain} \tag{4.2}$$

$$\mu = \mu_{id} + \mu_{hs} + \mu_1 + \mu_2 + \mu_{chain} \tag{4.3}$$

where the terms correspond to the ideal, hard sphere, first-order attractive, second-order attractive, and chain contributions, respectively.

The ideal term is calculated by

$$F_{id} = kT \int \rho(\mathbf{r}) \left[\ln(\Lambda^3 \rho(\mathbf{r})) - 1 \right] d\mathbf{r} \tag{4.4}$$

where Λ is the de Broglie wave length. The segment density $\rho(\mathbf{r})$ is used instead of $\rho_m(\mathbf{R})$ because we are solving for the segment density, not the molecular density. The chemical potential contribution of the ideal term is calculated from

$$\mu_{id} = kT \ln(\rho_m \Lambda^3) \tag{4.5}$$

where ρ_m is the molecular number density, which is equal to $m\rho_b$, where ρ_b is the bulk segment number density.

The hard sphere term is calculated in FMT using a series of four scalar and two vector densities, which are defined by

$$n_i(\mathbf{r}) = \int \rho(\mathbf{r}')\omega_i(\mathbf{r} - \mathbf{r}')d\mathbf{r}' \tag{4.6}$$

where the subscript ($i = 0, 1, 2, 3, V1, V2$) denotes the weighting function. The six weighting functions are related to the geometry of a molecule and are

$$\omega_0(r) = \frac{\omega_2(r)}{4\pi R^2} \tag{4.7}$$

$$\omega_1(r) = \frac{\omega_2(r)}{4\pi R} \tag{4.8}$$

$$\omega_2(r) = |\nabla\Theta(R - r)| = \delta(R - r) \tag{4.9}$$

$$\omega_3(r) = \Theta(R - r) \tag{4.10}$$

$$\omega_{V1}(\mathbf{r}) = \frac{\omega_{V2}(\mathbf{r})}{4\pi R} \tag{4.11}$$

$$\omega_{V2}(\mathbf{r}) = \nabla\Theta(R - r) = \frac{\mathbf{r}}{r}\delta(R - r) \tag{4.12}$$

for a sphere of radius R where the vector terms $\mathbf{n}_{V1}$ and $\mathbf{n}_{V2}$ vanish in the bulk.

The contribution of the hard sphere repulsive term to the free energy is calculated in FMT using[13,15,22]

$$F_{hs} = kT \int \Phi^{hs}[n_\alpha(\mathbf{r}')]d\mathbf{r}' \tag{4.13}$$

In the original "White Bear" version of FMT by Roth *et al.*,[13] a Mansoori-Carnahan-Starling-Leland (MCSL) fluid, which is described by an equation of state for hard sphere mixtures that reduces to the Carnahan-Starling equation of state[68] for single components, was used to give

$$\Phi^{hs}[n_\alpha(\mathbf{r})] = -n_0 \ln(1-n_3) + \frac{n_1 n_2 - \mathbf{n}_{V1}\cdot\mathbf{n}_{V2}}{1-n_3} + \frac{(n_2^3 - 3n_2\mathbf{n}_{V2}\cdot\mathbf{n}_{V2})(n_3 + (1-n_3)^2\ln(1-n_3))}{36\pi n_3^2(1-n_3)^2} \tag{4.14}$$

The more recent "White Bear Mark II" revision of FMT by Hansen-Goos and Roth[22] corresponds to a Carnahan-Starling-Boublík (CSB) fluid and is of the form

$$\Phi^{hs}[n_\alpha(\mathbf{r})] = -n_0 \ln(1-n_3) + (n_1 n_2 - \mathbf{n}_{V1}\cdot\mathbf{n}_{V2})\frac{1+\frac{1}{3}\phi_2(n_3)}{1-n_3} + (n_2^3 - 3n_2\mathbf{n}_{V2}\cdot\mathbf{n}_{V2})\frac{1-\frac{1}{3}\phi_3(n_3)}{24\pi(1-n_3)^2} \tag{4.15}$$

with

$$\phi_2(n_3) = \frac{1}{n_3}[2n_3 - n_3^2 + 2(1-n_3)\ln(1-n_3)] \tag{4.16}$$

and

$$\phi_3(n_3) = \frac{1}{n_3^2}[2n_3 - 3n_3^2 + 2n_3^3 + 2(1-n_3)^2\ln(1-n_3)] \tag{4.17}$$

The chemical potential contribution for the hard sphere term is calculated from

$$\mu_{hs} = mkT \sum_i \frac{\partial \Phi_b^{hs}}{\partial n_{i,b}} \frac{\partial n_{i,b}}{\partial \rho_b} \tag{4.18}$$

where in the bulk $n_{0,b} = \rho_b$, $n_{1,b} = R\,\rho_b$, $n_{2,b} = 4\pi R^2 \rho_b$, and $n_{3,b} = (4/3)\pi R^3 \rho_b$.

For the attractive terms, a perturbation analysis[3] gives for the first-order term

$$F_1 = \frac{1}{2}\int \rho(\mathbf{r}') \int \rho(\mathbf{r}'') g^{hs}[n_3(\mathbf{r}''); \mathbf{r}'']\phi(|\mathbf{r}' - \mathbf{r}''|)\, d\mathbf{r}''d\mathbf{r}' \tag{4.19}$$

in which the attractive potential is the square-well given by

$$\phi(r) = \begin{cases} -\epsilon_{ff} & \text{if} \quad \sigma_{ff} \leq r < \lambda_f \, \sigma_{ff} \\ 0 & \text{if} \quad r \geq \lambda_f \, \sigma_{ff} \end{cases} \tag{4.20}$$

where $\sigma_{ff} = 2R$ is the hard sphere diameter, and the hard sphere radial distribution function, $g^{hs}[n_3(\mathbf{r}); \mathbf{r}]$, developed by Chang and Sandler[69] with a Verlet-Weis[70] correction, is a function of density and distance. The chemical potential contribution for the first-order term is

$$\mu_1 = -4m\epsilon(\lambda^3 - 1)\left(2n_{3,b}g_e^{hs} + n_{3,b}^2 \frac{\partial g_e^{hs}}{\partial \eta_e}\frac{\partial \eta_e}{\partial n_{3,b}}\right) \tag{4.21}$$

where, following Gil-Villegas *et al.*[3] for SAFT-VR, the hard sphere radial distribution function at contact is calculated using the Carnahan-Starling[68] expression

$$g_e^{hs} = \frac{1 - \eta_e/2}{(1 - \eta_e)^3} \tag{4.22}$$

The effective density η_e is calculated for an extended value up to $\lambda = 3$ using the relation of Patel *et al.*[71]

$$\eta_e = \frac{c_1 n_{3,b} + c_2 n_{3,b}^2}{(1 + c_3 n_{3,b})^3} \tag{4.23}$$

with

$$\begin{pmatrix} c_1 \\ c_2 \\ c_3 \end{pmatrix} = \begin{pmatrix} -3.165 & 13.35 & -14.81 & 5.703 \\ 43.00 & -191.7 & 273.9 & -128.9 \\ 65.04 & -266.5 & 361.0 & 162.7 \end{pmatrix} \begin{pmatrix} 1/\lambda \\ 1/\lambda^2 \\ 1/\lambda^3 \\ 1/\lambda^4 \end{pmatrix} \tag{4.24}$$

The second-order attractive term adopted here is an improvement on the treatment of Barker and Henderson,[72,73] which was used in SAFT-VR. Developed by Zhang[5] and based on a macroscopic compressibility approximation that takes the correlation of molecules in neighboring shells into account, it is given by

$$F_2 = -\frac{1}{4kT}\int \rho(\mathbf{r}') \int \rho(\mathbf{r}'')(1 + 2\xi n_3^2)[\phi(|\mathbf{r}' - \mathbf{r}''|)]^2 K^{hs}(\mathbf{r}'') g^{hs}[n_3(\mathbf{r}''); \mathbf{r}'']d\mathbf{r}''d\mathbf{r}' \tag{4.25}$$

where $\xi = 1/\eta_{con}^2$ with $\eta_{con} = 0.493$, which is the packing fraction where the fluid condenses.[5] The hard sphere isothermal compressibility for a CSB fluid is calculated from

$$K^{hs} = \frac{(1 - n_3)^4}{1 + 4n_3 + 4n_3^2 - 4n_3^3 + n_3^4} \tag{4.26}$$

The chemical potential contribution for the second-order attractive term is given by

$$\mu_2 = \frac{-2m\epsilon^2(\lambda^3-1)}{kT}\left\{4\xi n_{3,b}^3 K^{hs} g_e^{hs} + \left(1+2\xi n_{3,b}^2\right)\times \left[2n_{3,b}K^{hs}g_e^{hs} + n_{3,b}^2\left(\frac{\partial K^{hs}}{\partial n_{3,b}}\, g_e^{hs} + K^{hs}\frac{\partial g_e^{hs}}{\partial \eta_e}\frac{\partial \eta_e}{\partial n_{3,b}}\right)\right]\right\} \tag{4.27}$$

For the hard sphere chain term, Yu and Wu[4] recast Wertheim's first order perturbation theory for chain connectivity in a bulk fluid to a form needed for an inhomogeneous fluid using the weighted densities of FMT. The chain contribution to the Helmholtz energy is described by

$$F_{chain} = kT\int \Phi^{chain}[n_\alpha(\mathbf{r}')]d\mathbf{r}' \tag{4.28}$$

$$\Phi^{chain}[n_\alpha(\mathbf{r})] = \frac{1-m}{m} n_0\,\zeta \ln y^{hs}(\sigma_{ff}, n_\alpha) \tag{4.29}$$

$$\zeta = 1 - \frac{\mathbf{n}_{V2}\cdot\mathbf{n}_{V2}}{n_2^2} \tag{4.30}$$

$$y^{hs}(\sigma_{ff}, n_\alpha) = \frac{1}{1-n_3} + \frac{n_2\sigma_{ff}\zeta}{4(1-n_3)^2} + \frac{n_2^2\sigma_{ff}^2\zeta}{72(1-n_3)^3} \tag{4.31}$$

where y^{hs} is the contact value of the cavity correlation function between segments. Note that, following Yu and Wu,[4] Φ_{chain} differs from the SAFT-VR term, which would contain the square well y^{sw} rather than the hard sphere y^{hs}. The chemical potential contribution for the chain term is given by

$$\mu_{chain} = kT(1-m)\sum_i \frac{\partial \Phi_b^{chain}}{\partial n_i}\,\frac{\partial n_i}{\partial \rho_b} \tag{4.32}$$

The equation used for the external potential depends on the situation being described. The interaction between a hard-sphere chain and a hard wall is described by

$$V_{ext}(z) = \begin{cases} 0, & z \geq 0 \\ \infty, & z < 0 \end{cases} \tag{4.33}$$

The interaction with a square-well attractive wall is given by

$$V_{ext}(z) = \begin{cases} 0, & z > \lambda_w\,\sigma_{sf} \\ -\epsilon_w, & 0 < z < \lambda_w\,\sigma_{sf} \\ \infty, & z < 0 \end{cases} \tag{4.34}$$

where σ_{sf} is the solid-fluid collision diameter. The interaction with a Lennard-Jones attractive wall is represented as

$$V_{ext}(z) = 4\epsilon_w \left[\left(\frac{\sigma_{sf}}{z} \right)^{12} - \left(\frac{\sigma_{sf}}{z} \right)^{6} \right] \tag{4.35}$$

To compare the square-well and Lennard-Jones attractive walls, the ϵ values were determined by equating the second virial coefficient[75] of the square-well wall, B_{SW}, to the second virial coefficient of the Lennard-Jones wall, B_{LJ}, holding σ_{sf} constant.

Integrating the 6-12 Lennard-Jones potential over the walls, rather than applying it to a slice of a pore, gives the 10-4 wall potential on each side of the pore described by[27,77]

$$V_{ext}(z) = \phi_w(z) + \phi_w(H - z) \tag{4.36}$$

with

$$\phi_w(z) = 2\pi\epsilon_w\rho_w\sigma_{sf}^2 \left[\frac{2}{5} \left(\frac{\sigma_{sf}}{z} \right)^{10} - \left(\frac{\sigma_{sf}}{z} \right)^{4} \right] \tag{4.37}$$

where ρ_w is the density of the wall molecules.

Taking the functional derivative of eq 5.1 and rearranging the result gives the following equation for calculation of the segment equilibrium density profile[4]

$$\rho(z) = \frac{1}{\Lambda^3} \exp(\mu) \sum_{i=1}^{m} \exp\left[-\frac{\psi(z)}{kT} \right] G^i(z) G^{m+1-i}(z) \tag{4.38}$$

where μ is the chemical potential. The solution method involves iterating on the segment density. In eq 5.6, we have

$$\psi(z) = \frac{\delta F_{hs}}{\delta\rho(\mathbf{r})} + \frac{\delta F_1}{\delta\rho(\mathbf{r})} + \frac{\delta F_2}{\delta\rho(\mathbf{r})} + \frac{\delta F_{chain}}{\delta\rho(\mathbf{r})} + V_{ext} \tag{4.39}$$

and

$$G^i = \int \exp\left[-\frac{\psi(z)}{kT} \right] \frac{\Theta(\sigma_{ff} - |z - z'|)}{2\sigma_{ff}} G^{i-1} dz' \tag{4.40}$$

where $G^1(z) = 1$. Due to the summation term in eq 5.6, the number of segments m in the implementation of SAFT is limited to integer values.

The equilibrium value of the density, calculated from eq 5.6, can be used to calculate the average density in a pore from

$$\rho_{avg}(H,P) = \frac{1}{m}\,\frac{1}{H}\int_0^H \rho(z)\,dz \tag{4.41}$$

where H is the pore width. The surface excess is then given by

$$\Gamma_{ex} = (\rho_{avg} - \rho_{bulk})\,H \tag{4.42}$$

4.3 Results and Discussion

First, we compare predictions of density profiles for adsorption of chain molecules on flat surfaces with several published results of Monte Carlo simulations; in doing so, we also assess the magnitudes of the contributions of the terms in eqs 5.2 and 4.3 on the density profiles. Second, we extend a published study using its parameters to consider adsorption in narrow pores with the fluid-wall potential given by the square-well potential, and we compare results with those for a Lennard-Jones wall potential. Finally, we consider adsorption in a slit-shaped pore with the fluid-wall potential given by the 10-4 potential.

Adsorption on Flat Surfaces and Comparisons with Monte Carlo Simulations

Predictions from our theoretical approach using the FMT formulations of both Roth *et al.*[13] and Hansen-Goos and Roth[15,22] are compared here with a variety of different Monte Carlo simulations from the literature. First considered are hard spheres against hard-walls. Then, a set of hard-sphere chains against hard-walls are treated to establish the validity of the chain function. Next, attractive potentials are incorporated to compare results with simulations for hard and attractive walls. In our figures for these comparisons, we follow the common convention of measuring the pore wall coordinate from the inside edge of the pore.

For hard spheres against hard walls, we set $m = 1$, $\epsilon_{ff} = 0$, and $V_{ext} = \infty$. Figure 4.1 shows density profiles compared with data of Snook and Henderson[78] for hard spheres against

hard walls at four bulk densities from $\rho\sigma_{ff}^3 = 0.57$ to 0.91. The results agree with the well-known requirement for momentum transfer that the density of any fluid in contact with a hard wall is $\rho(0) = P/kT$. All of the figures show good quantitative agreement between our approach and the Monte Carlo simulations. Only slight differences are seen at the highest densities in Figures 4.1c and 4.1d.

Figure 4.1 also shows our calculations comparing the use of the White Bear FMT [13] and the White Bear Mark II FMT. [15,22] The density profiles from Figure 4.1c for both formulations are shown in an expanded form in Figure 4.2. The White Bear Mark II FMT agrees more closely with the Monte Carlo simulations of Snook and Henderson [78] for hard spheres against hard walls. The insert in Figure 4.2 shows a further blown up portion of where the two theories differ the most. These differences are apparent in modeling chain molecules as well, with White Bear Mark II producing the closest fitting curves. For this reason and because, as mentioned earlier, the derivation of the White Bear Mark II FMT is consistent with scaled-particle theory in the bulk, [22] all of the following calculations reported in this chapter use the White Bear Mark II FMT.

For hard-sphere chains and hard walls, several comparisons were performed involving the adsorption of m-mers. This was done by setting m equal to the number of spherical monomer units in the chain. Figure 4.3 compares segment density profiles determined using our approach with a series of Monte Carlo simulations by Kierlik and Rosinberg [79] for 3-mer chains. The predictions show excellent agreement in both values and structure over the full range of bulk packing fractions, from $\eta_b = 0.1$ to 0.45. At the lower densities in Figures 4.3a and 4.3b, the density at contact is lower than the average density and increases to form the first layer; however, a layer near $z/\sigma_{ff} = 1$ is still apparent. For the intermediate densities shown in Figures 4.3c and 4.3d, the density at contact is above the average density, as for hard spheres, and shows the first layer becoming better defined. For the higher densities shown in Figures 4.3e and 4.3f, the second layer has begun to form.

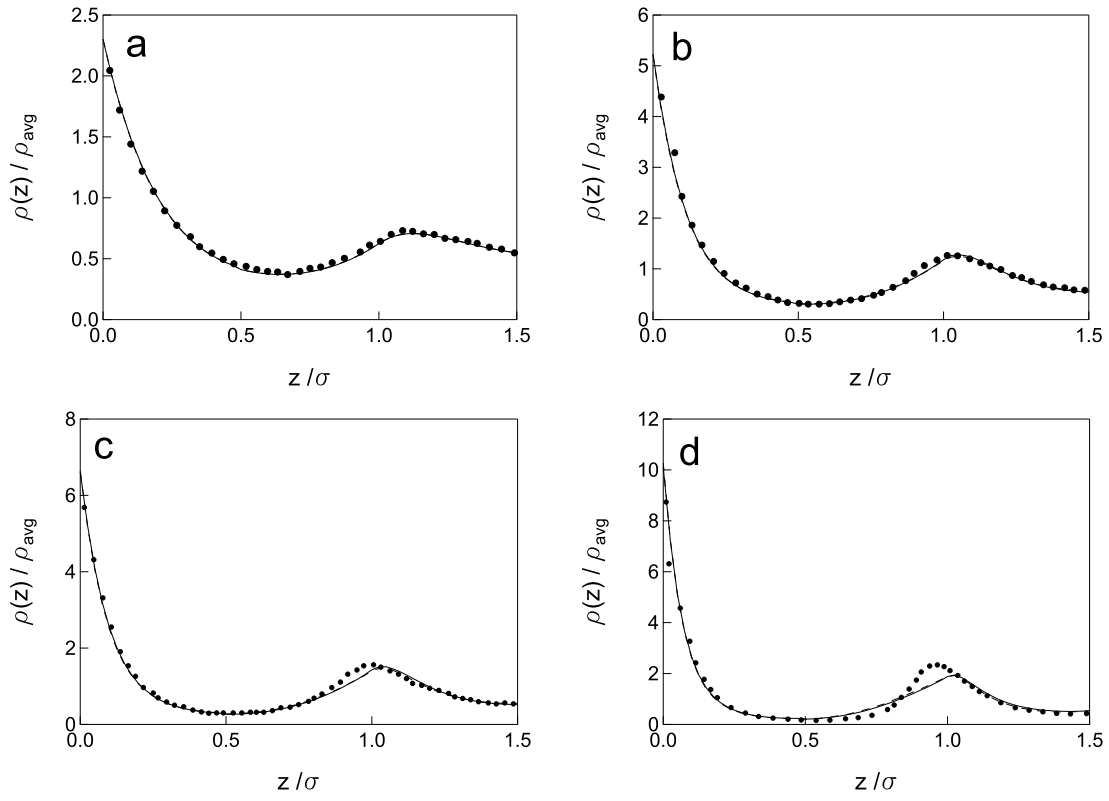

Figure 4.1: Hard sphere against a hard wall at bulk packing fractions η_b of (a) 0.57, (b) 0.755, (c) 0.81, and (d) 0.91. Circles are Monte Carlo results,[78] solid curve is White Bear FMT, and dashed curve is White Bear Mark II FMT.

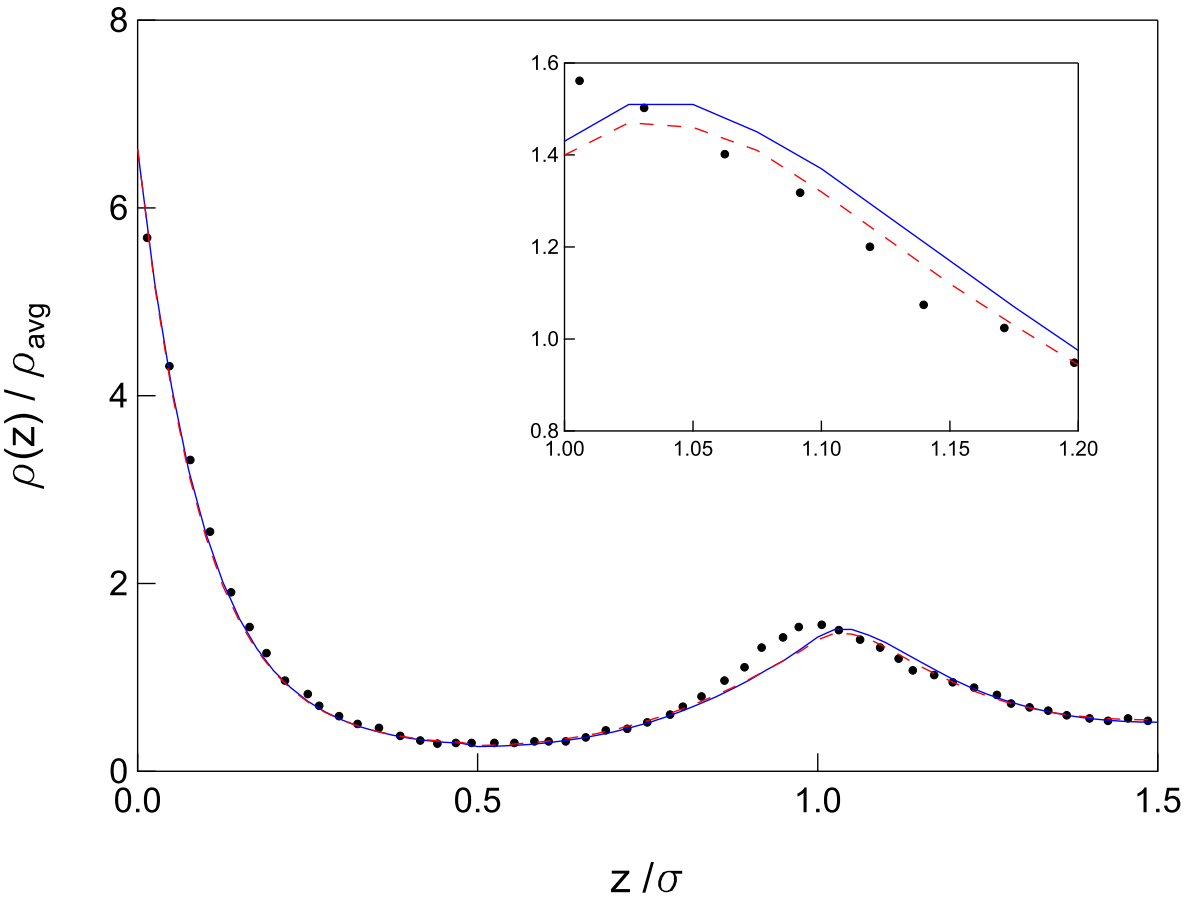

Figure 4.2: Hard sphere against a hard wall at a bulk packing fraction of $\eta_b = 0.81$. Circles are Monte Carlo results,[78] solid curve is the White Bear FMT, and dashed curve is the White Bear Mark II FMT.

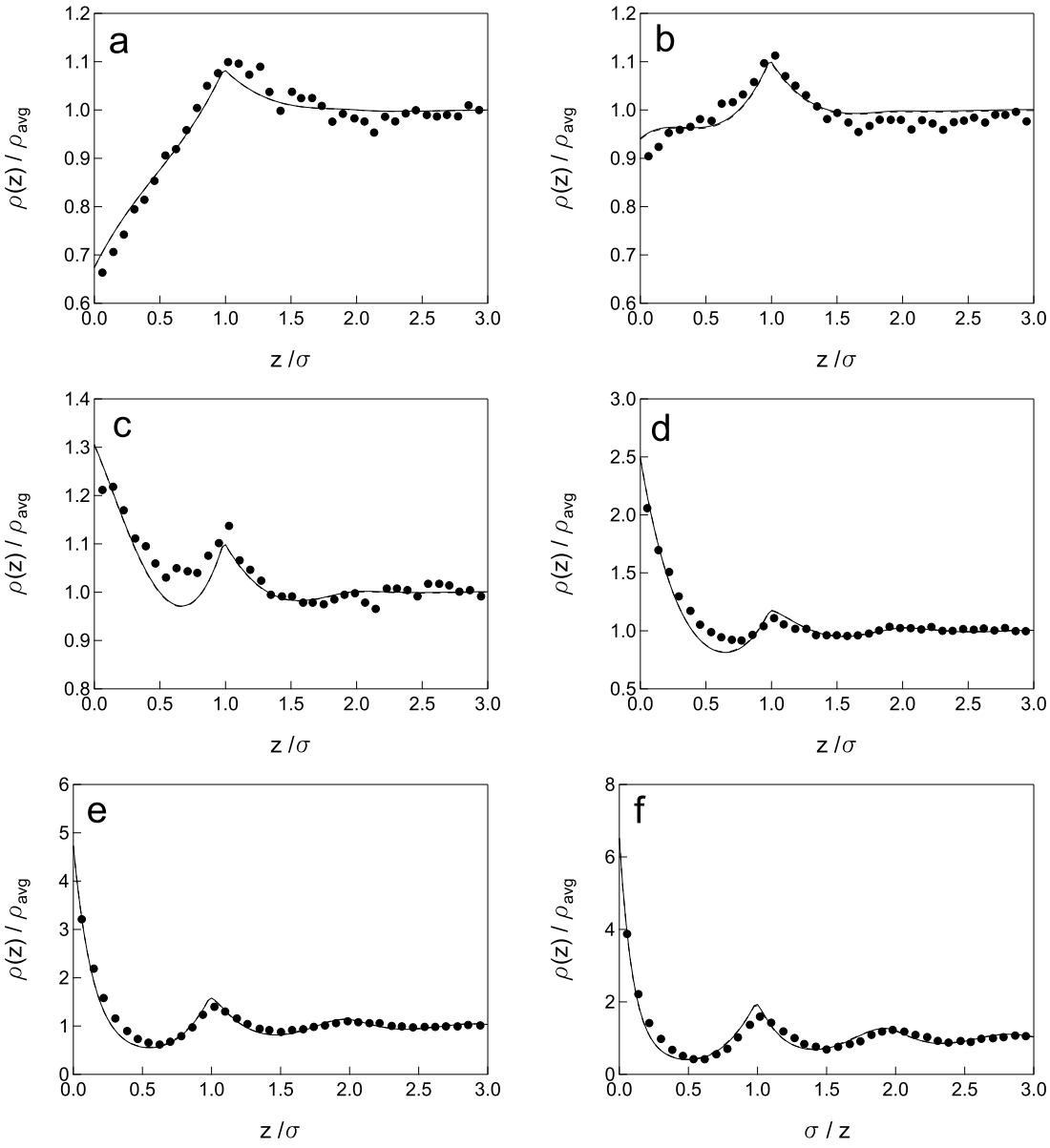

Figure 4.3: Hard sphere 3-mer against a hard wall at bulk packing fractions η_b of (a) 0.1, (b) 0.15, (c) 0.20, (d) 0.30, (e) 0.40, and (f) 0.45. Circles are Monte Carlo results,[79] and solid curve is the White Bear Mark II FMT.

Considering longer hard sphere chains, Figure 4.4 shows a comparison of our predicted segment density profiles with simulations of 4-mer chains by Dickman and Hall[80] at bulk packing densities from 0.107 to 0.417. The density profiles show good agreement with the density at the wall and with the maximum and minimum values. Figure 4.5 shows our predictions compared with simulations of 20-mer chains by Yethiraj and Woodward[51] at bulk packing fractions from 0.1 to 0.35. Small deviations between the theoretical predictions and the Monte Carlo simulations are apparent. Figure 4.5a shows a slightly lower segment density in the center of the pore, and the maximum and minimum values in the troughs and peaks show some variation with the Monte Carlo results in Figures 4.5b and 4.5c. However, the structure of the theory agrees well, showing minimums and maximums at the correct locations. Thus, it is apparent from Figures 4.1–4.5 that the theory provides generally good agreement with Monte Carlo simulation results over a wide range of bulk densities and chain lengths.

We now consider an attractive potential incorporated into the model by the inclusion of eqs 4.19 and 4.25. Results are compared with the Monte Carlo simulations of Ye *et al.*,[64] which use $\epsilon_{ff}/kT = 3.0$, $\lambda_f = 1.5$, and $\lambda_w = 1.0$. The interaction with the hard wall was treated using eq 4.33, while the attractive wall was simulated using eqs 4.34 and 4.35. Figure 4.6 shows the density profiles of 3-mers with second order attractive potentials against a hard wall. Figure 4.6a, for a bulk packing fraction η_b of 0.10, shows good agreement with the Monte Carlo simulations. We note distinct differences between Figure 4.6a and Figure 4.3a resulting from the application of the attractive potential; specifically, the density at contact is lower with the attractive potential included and does not show the peak at $z/\sigma_{ff} = 1$. For $\eta_b = 0.3$, Figure 4.6b shows good agreement in the placement of the maximum and minimum of the density profile; however, significantly larger oscillations are apparent in comparison with the results of the Monte Carlo simulation, or in comparison with the hard sphere chain results shown in Figure 4.3d. For an attractive square-well wall, we use eq 4.34 and compare

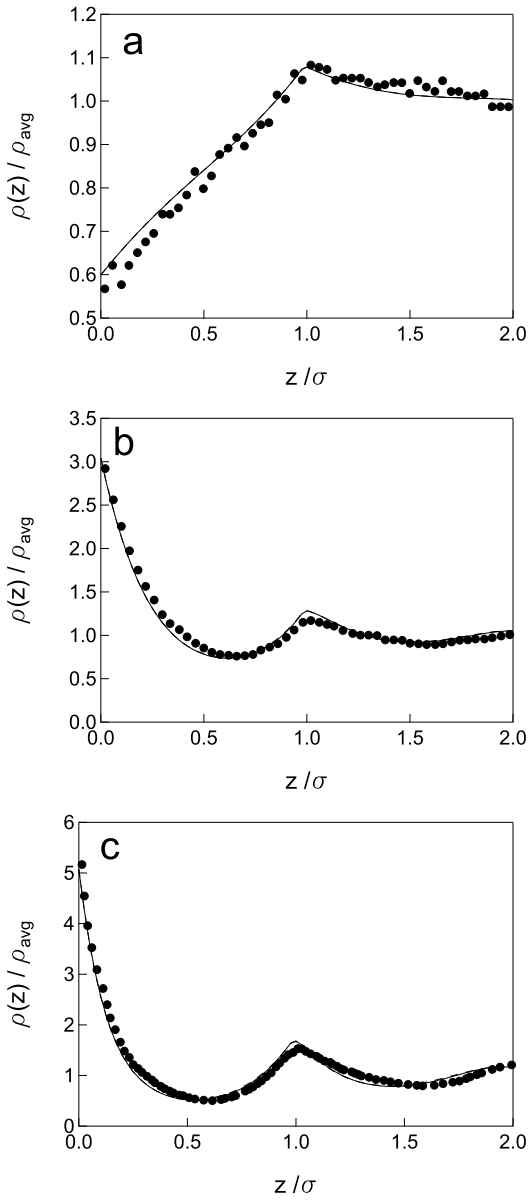

Figure 4.4: Hard sphere 4-mer against a hard wall at bulk packing fractions η_b of (a) 0.107, (b) 0.340, and (c) 0.417. Circles are Monte Carlo results,[80] and solid curve is the White Bear Mark II FMT.

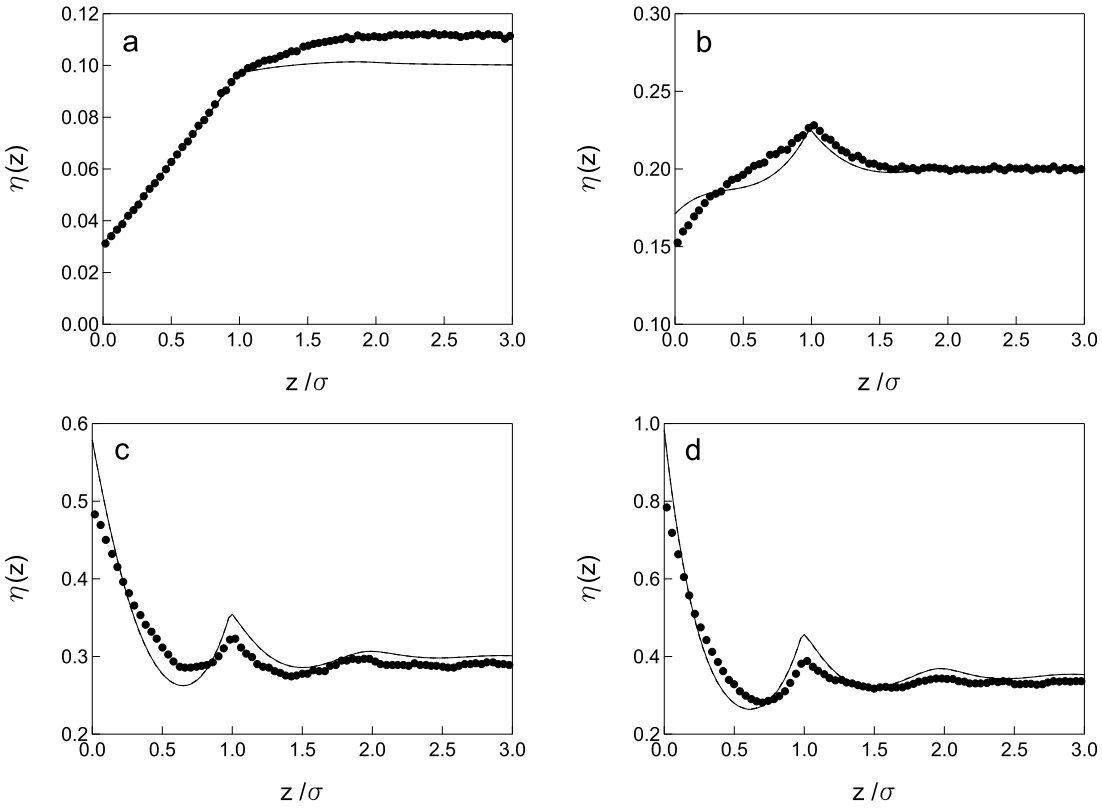

Figure 4.5: Hard sphere 20-mer against a hard wall at bulk packing fractions η_b of (a) 0.10, (b) 0.20, (c) 0.30, and (d) 0.35. $\eta(z) \equiv \rho(z)\sigma_{ff}^3(\pi/6)$ is the local packing fraction in the pore. Circles are Monte Carlo results,[51] and solid curve is the White Bear Mark II FMT.

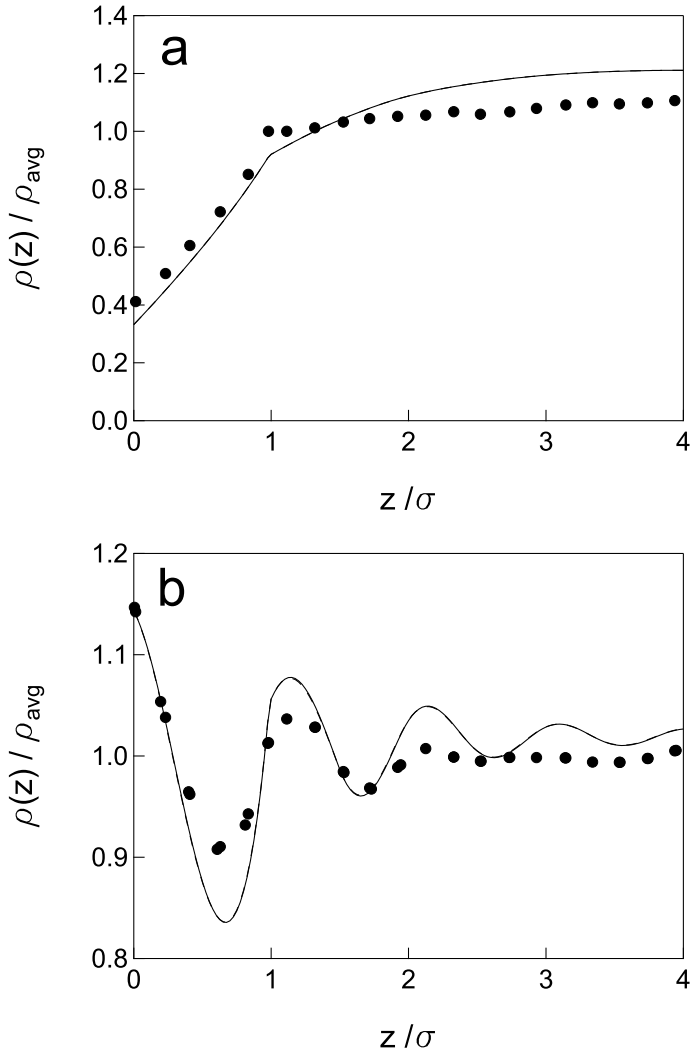

Figure 4.6: Attractive 3-mer against a hard wall at bulk packing fractions η_b of (a) 0.10 and (b) 0.30. Circles are Monte Carlo results,[64] and solid curve is the White Bear Mark II FMT.

the predictions or our approach with the Monte Carlo simulation results of Ye *et al.*,[64] which use $\epsilon_w/kT = -1.0$. Our predictions show good qualitative agreement with the simulations. Figure 4.7a shows the density profile for $\eta_b = 0.10$. The contact density is somewhat lower than for the Monte Carlo simulations, but the density profile shows the same general trends. The drop at $z/\sigma_{ff} = 1$ as well as the hump between $z/\sigma_{ff} = 1$ and 2 are properly located. The results for $\eta_b = 0.3$ are shown in Figure 4.7b. Our approach shows good quantitative agreement with the Monte Carlo simulation, such as the sharp density decrease at $z/\sigma_{ff} = 1$. When compared to the results for the hard wall shown in Figure 4.6, differences are apparent. The attractive potential of the wall clearly affects the profiles. Where the attractive potential ends at $z/\sigma_{ff} = 1$, there is the sharp decrease, which is not seen for the hard wall. Also, the densities near the wall are higher for the attractive wall and the oscillations toward the center of the pore are dampened.

In comparing the impacts of the various terms in eqs 5.2 and 4.3 on the density profiles, we found that the effect of the first-order attractive term was an order of magnitude less than the hard sphere and chain terms. Similarly, the impact of the second-order attractive term was an order of magnitude less than the first-order attractive term.

Extensions of Literature Examples

To consider further the impact of the attractive potential, pores were modeled with attractive walls simulated using the square-well potential of eq 4.34 and, for comparison, the Lennard-Jones potential of eq 4.35. We retain the parameter values from Ye *et al.*[64] for the attractive wall with the square well potential. The value of ϵ for the Lennard-Jones wall potential was obtained from the square well wall parameters of Ye *et al.* by equating second virial coefficients while holding σ_{ff} constant. The coordinate system is shown in Figure 4.8, where the two potentials are compared. For the square-well and LJ pores, the pore width was measured from the edge of the wall atoms of one wall to the edge of the wall atoms of the

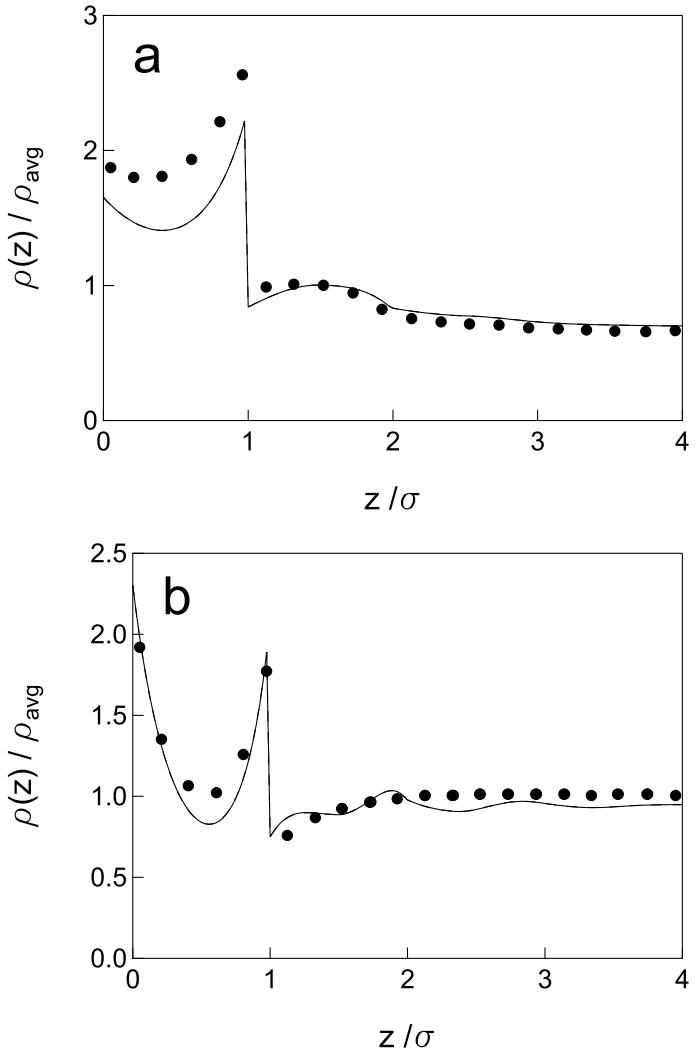

Figure 4.7: Attractive 3-mer against an attractive SW wall at bulk packing fractions η_b of (a) 0.10 and (b) 0.30. The potential between the wall and fluid is $\epsilon_w/kT = -1.0$. Circles are Monte Carlo results,[64] and solid curve is the White Bear Mark II FMT.

opposite wall. The coordinate inside the pore was measured from the edge of the pore wall to the center of a chain segment.

Pore density profiles for 3-mers with second order attractive potentials inside a square-well attractive pore are shown in Figure 4.9 at a packing fraction of $\eta_b = 0.30$ for increasing pore widths from $1\,\sigma_{ff}$ to $8\,\sigma_{ff}$. For the larger pore widths studied, the density profile of Figure 4.7b is reproduced from each pore wall. The oscillations at the center of the $8\,\sigma_{ff}$ pore are of much lower amplitude than those of the smaller pores. The effects of the wall interations are short ranged, and so the center of the larger pores is not influenced by the wall potential. This leads to the center of the larger pores having a lower density than near the wall, approaching the bulk value of $\rho\sigma_{ff}^3 = 0.57$. As the pores become narrower, the oscillations become less and less pronounced until the pore is less than $2\,\sigma_{ff}$ wide. At a pore width less than $2\ \sigma_{ff}$, because the wall potential extends $1\,\sigma_{ff}$ from each wall, the attractive potentials from both walls begin to overlap. Steric effects in the small pores do not allow the molecules to form separate layers until, at a width of $1\ \sigma_{ff}$, a single layer of molecules is formed.

Similar behavior is apparent in Figure 4.10, where the attractive wall is determined by the Lennard-Jones potential. Comparing the integer pore widths, the SW wall predictions are similar to those of the LJ wall. The peaks and troughs coincide for the two potentials, although the oscillations are more prominent in Figure 4.10 as the LJ potential is much farther reaching. In pores between adjacent integer values of σ_{ff} (e.g., Figures 4.10b to 4.10d), the formation of another layer of molecules can be observed. A noticeable difference between the two potentials occurs at $1.5\,\sigma_{ff}$ away from each wall, where the SW potential becomes zero, resulting in a sharp decrease in the density seen previously in Figure 4.7 and Figures 4.9g–4.9i. This occurs only in pores larger than $3\,\sigma_{ff}$, for which the potentials from each wall no longer overlap, leaving a region inside the pore with only fluid-fluid interactions. Another difference is that the density begins to increase at $0.125\,\sigma_{ff}$ into the LJ wall. Because

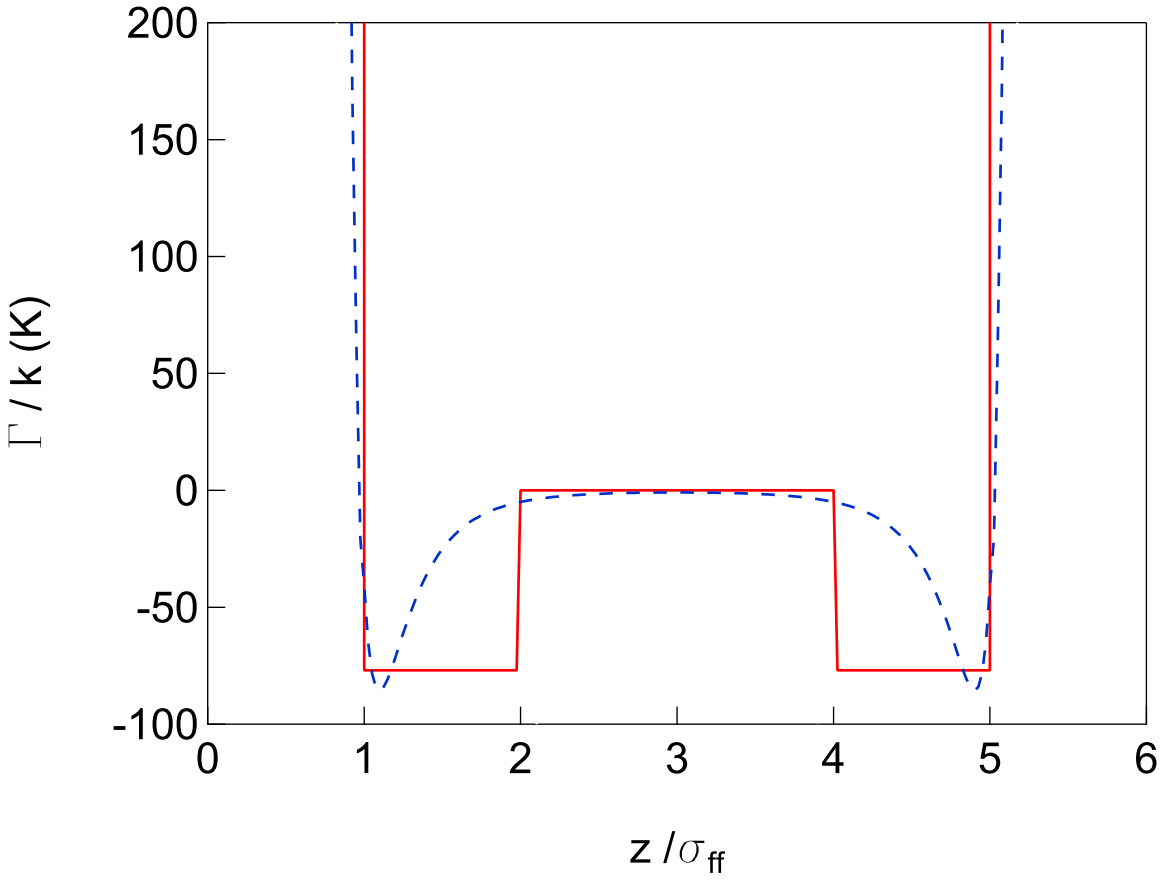

Figure 4.8: Square-well and Lennard-Jones wall potentials for attractive walls. Solid curve is square-well potential, and dashed curve is Lennard-Jones 6–12 potential.

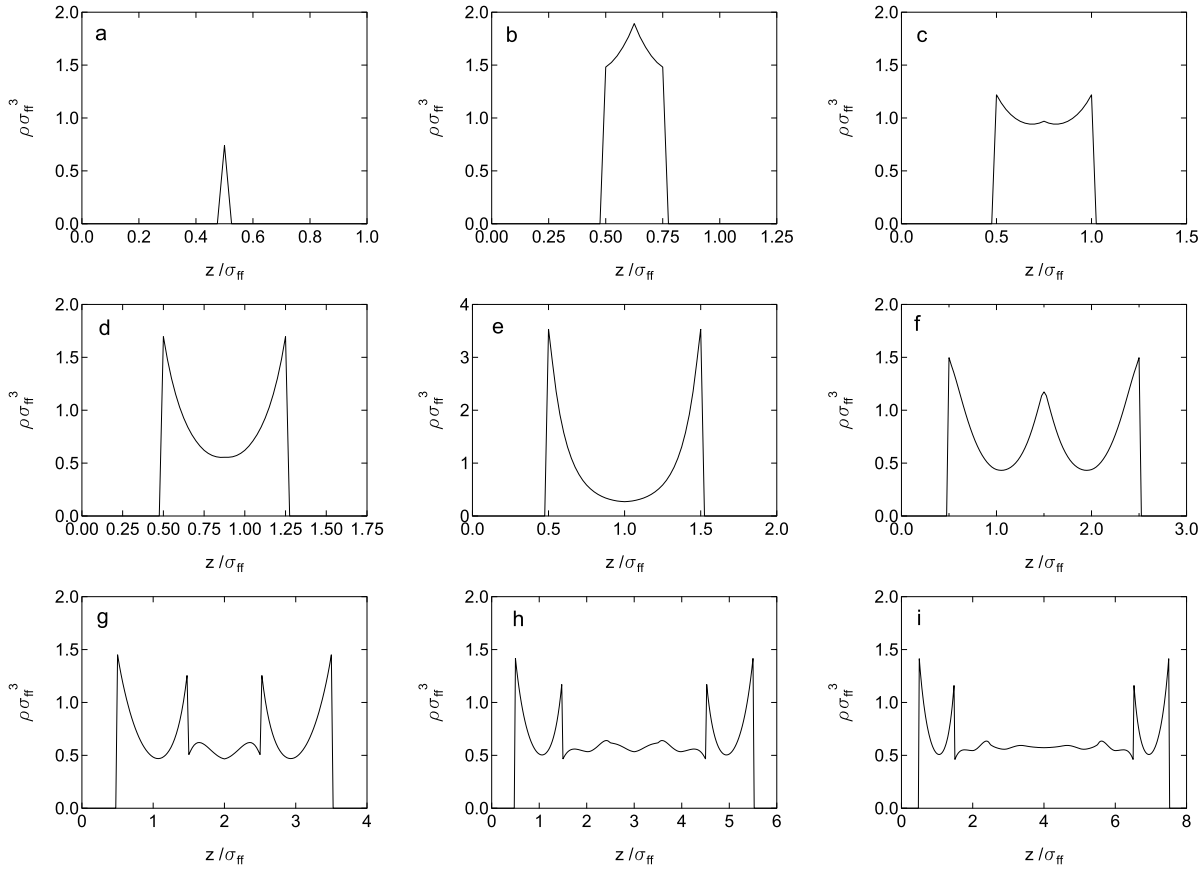

Figure 4.9: Attractive 3-mer against attractive SW walls at bulk packing fraction $\eta_b = 0.30$, which corresponds to $\rho\sigma_{ff}^3 = 0.57$. Pore widths are (a) 1 σ_{ff}, (b) 1.25 σ_{ff}, (c) 1.5 σ_{ff}, (d) 1.75 σ_{ff}, (e) 2 σ_{ff}, (f) 3 σ_{ff}, (g) 4 σ_{ff}, (h) 6 σ_{ff}, and (i) 8 σ_{ff}.

the LJ potential is a soft potential, it does not produce any of the sharp increases or decreases in the density profile found for the SW wall. The LJ potential produces a smoother profile at the walls but also broadens the width of the peak, as shown in Figures 4.9a and 4.10a.

As the pore size increases, the influence of the pore walls on the molecules located near the pore center decreases, as would be expected. In the $8\,\sigma_{ff}$ pore, the wall potential exerts very little influence at the center. From Figure 4.8, the LJ potential extends approximately $2\,\sigma_{ff}$ from each wall, so pores larger than about $6\,\sigma_{ff}$ will have very little influence of the pore walls in the center of the pore. For these large pores, the same oscillations occur from each wall of every pore, consistent with molecules adsorbing on a single flat wall rather than within a pore.

Adsorption in Slit-Shaped Pores

To consider more realistic adsorption in slit-shaped pores, whole pores were modeled with attractive walls using the 10-4 potential[27,77] of eq 4.37. A comparison of the LJ and 10-4 wall potentials is shown in Figure 4.11. The 10-4 potential is much more attractive than the LJ potential, since the 10-4 potential allows for the walls to extend from a single wall atom (as in the SW and LJ cases) to a continuous wall one layer of atoms thick. This allows the 10-4 potential to extend father from the wall into the pore in comparison to the LJ potential, as shown in Figure 4.11. The 10-4 potential used in this theory is similar in depth to other well-known potentials in the literature.[27]

Pore density profiles for 3-mers against 10-4 walls are shown in Figure 4.12. The pore densities for the continuous wall are much larger than for the single wall atom LJ case shown in Figure 4.10 due to many more wall atoms interacting with the chain molecules. Also, the density peaks are much steeper for 10-4 walls due to the greater attraction of the chain molecules to the walls and the formation of more distinct layers. Furthermore, the area between peaks for the 10-4 walls approaches zero, which is significantly different from the

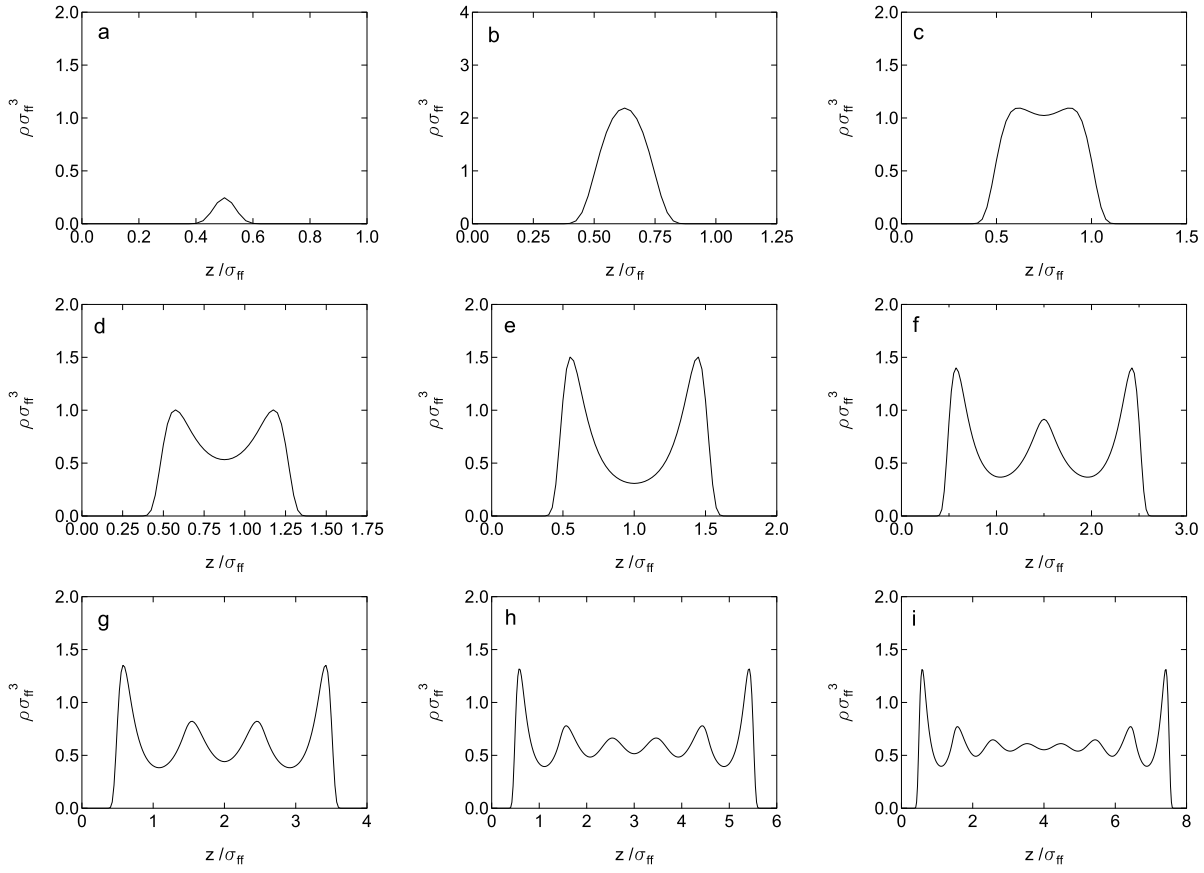

Figure 4.10: Attractive 3-mer against attractive LJ walls at bulk packing fraction $\eta_b = 0.30$, which corresponds to $\rho\sigma_{ff}^3 = 0.57$. Pore widths are (a) 1 σ_{ff}, (b) 1.25 σ_{ff}, (c) 1.5 σ_{ff}, (d) 1.75 σ_{ff}, (e) 2 σ_{ff}, (f) 3 σ_{ff}, (g) 4 σ_{ff}, (h) 6 σ_{ff}, and (i) 8 σ_{ff}.

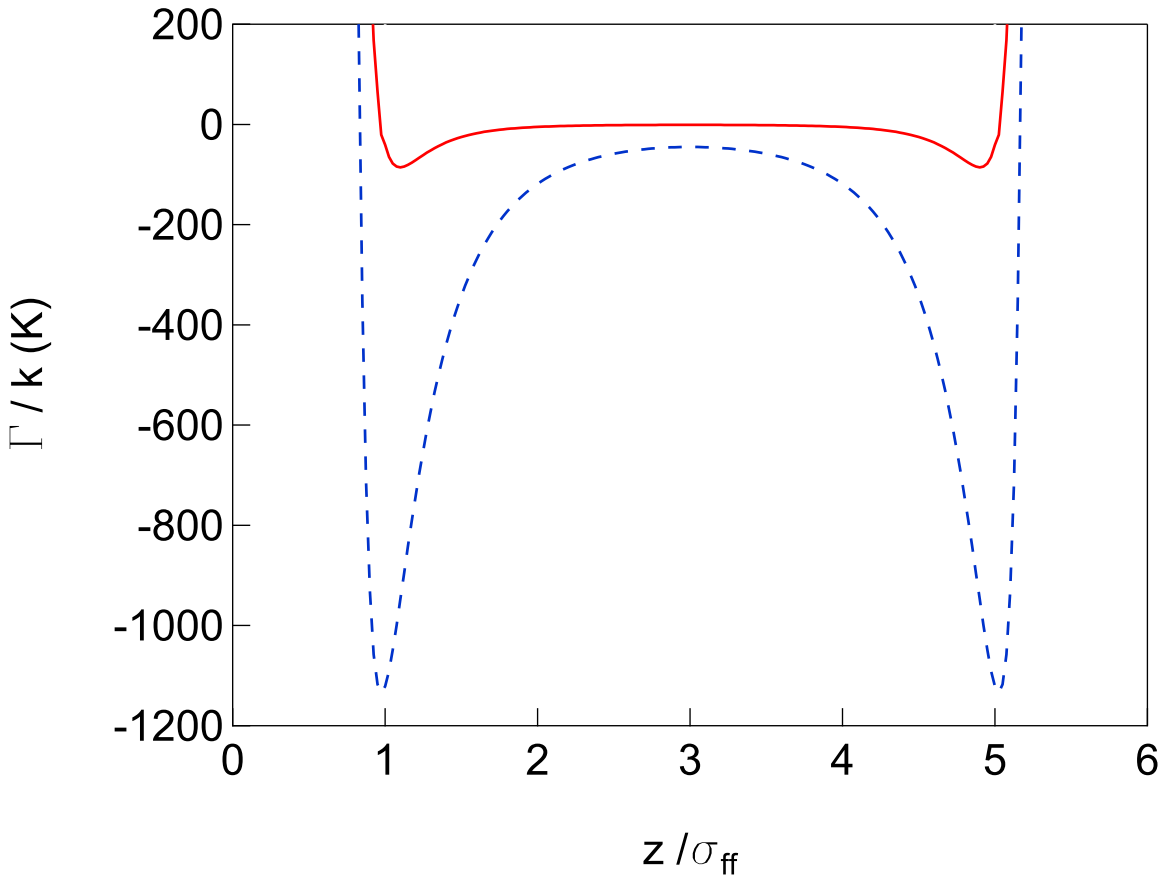

Figure 4.11: 6-12 Lennard-Jones and 10-4 wall potentials for attractive walls. Solid curve is 6-12 LJ potential and dashed (– – –) curve is 10-4 potential.

SW or LJ wall where the wall attractive potentials are not as strong. It should be noted that the density profiles for the $2\,\sigma_{ff}$ and $3\,\sigma_{ff}$ pores are steeper than for the other pores with 10-4 walls. Also, the peaks in the density profiles for these pores are much higher than those of the other pores. This results from the two walls of the pore exerting strong overlapping attractive potentials with the molecules inside the pore at small pore widths. As the pores becomes wider, the potentials become weaker as the attraction by the far wall, now further away, lessens. Thus, the molecules in the pore do not adsorb as strongly in the center as the pore widens past $3\,\sigma_{ff}$. At a pore width of $8\,\sigma_{ff}$, the density at the center of the pore has approached the bulk density.

Effect of chain length was also considered. Figure 4.13 shows isotherms for a 3-mer, a 2-mer, and a 1-mer in a $4\,\sigma_{ff}$ pore. Surface excess, calculated using eq 4.42, is plotted versus bulk packing fraction. The 1-mer pore isotherm becomes non-linear at a bulk packing fraction of approximately 10^{-6}. A point is reached where the average density within the pore increases more slowly than the bulk density, and the surface excess begins to decrease. The 2-mer chain has similar transitions, with the average pore density increasing slower than the bulk packing fraction above a bulk density of 0.2. The 3-mer chain has the broadest range of surface excesses, with the average pore density dropping below the bulk density at a bulk packing fraction of approximately 0.1.

It should be noted that the highest packing fractions shown in Figure 4.13 and those used in the literature examples are quite large. For example, pure gaseous nitrogen at its normal boiling point of 77 K has a packing fraction of approximately 10^{-3}. Higher bulk packing fractions for gaseous nitrogen at 77 K would not be possible in an equilibrium sense, as it would condense to a liquid if pressure were increased.

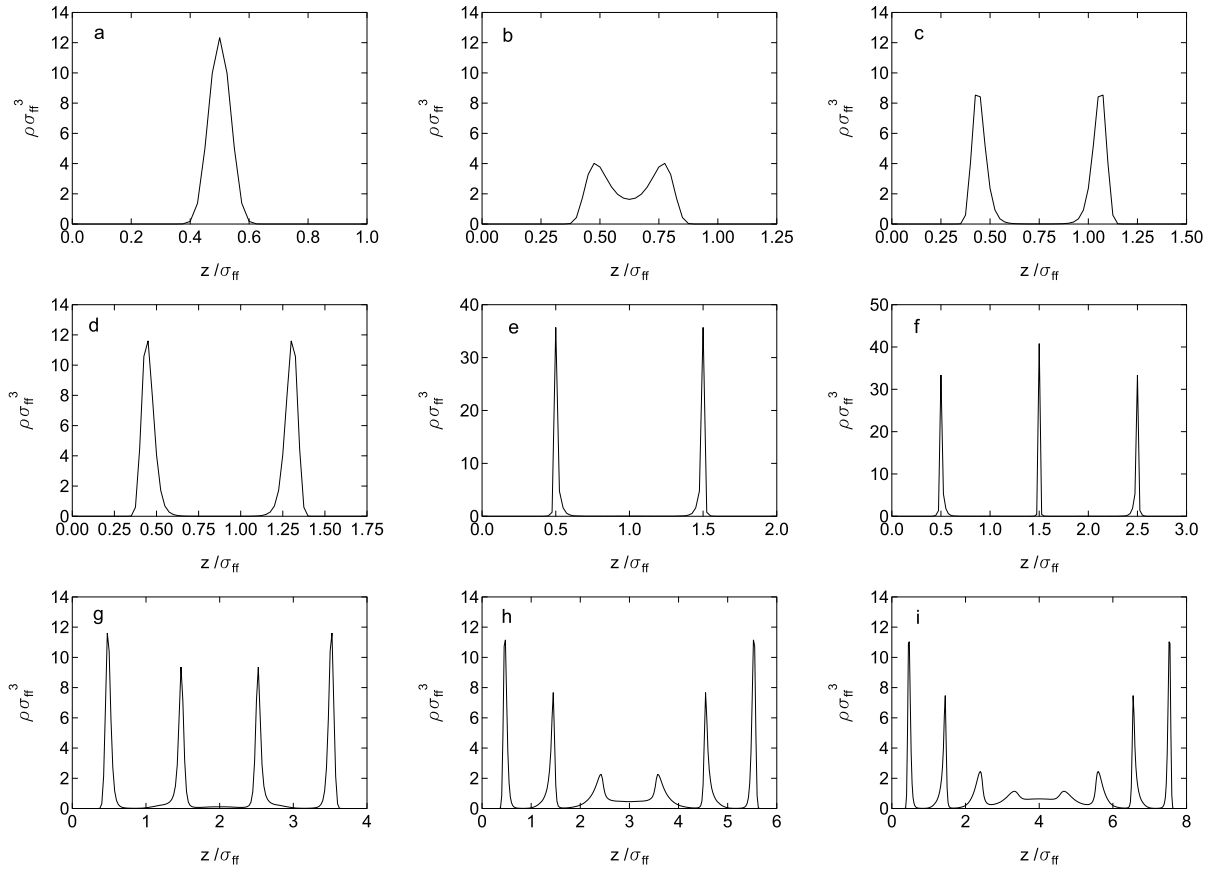

Figure 4.12: Attractive 3-mer in a pore with a 10-4 wall potential at a bulk packing fraction of $\eta_b = 0.30$, which corresponds to $\rho\sigma_{ff}^3 = 0.57$. Pore widths are (a) 1 σ_{ff}, (b) 1.25 σ_{ff}, (c) 1.5 σ_{ff}, (d) 1.75 σ_{ff}, (e) 2 σ_{ff}, (f) 3 σ_{ff}, (g) 4 σ_{ff}, (h) 6 σ_{ff}, and (i) 8 σ_{ff}.

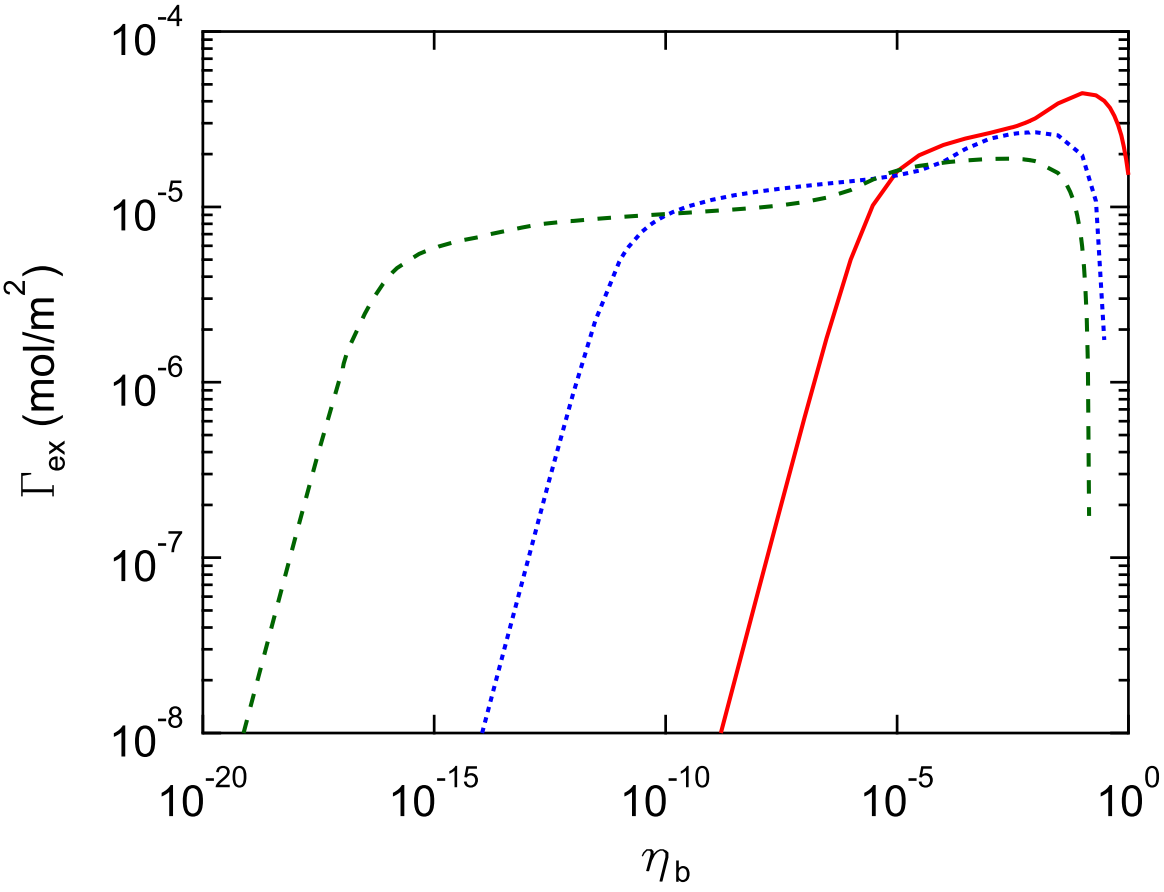

Figure 4.13: Surface excess isotherms inside a $4\,\sigma_{ff}$ pore at increasing bulk packing fractions for attractive 1-mer (solid), 2-mer (- - -), and 3-mer (– – –).

4.4 Conclusions

A new implementation of density functional theory (DFT) has been developed to treat the adsorption of chain molecules on flat surfaces and in slit-shaped pores. A version of the statistical associating fluid theory (SAFT) based on the SAFT-VR equation provides the framework for the chemical potential in the bulk. Fundamental measure theory (FMT) was adopted to provide a rigorous description of the hard sphere contribution to the free energy. By doing so, SAFT is transformed from a method for the treatment of a homogeneous fluid in the bulk to an accurate method for analysis of an inhomogeneous fluid against a surface. The attractive term for adsorption using SAFT has been developed using a perturbation analysis out to second order, rather than by assuming a more approximate mean field.

Several systems involving the adsorption of m-mers have been considered. Calculations using the theory show excellent agreement with published Monte Carlo simulations for densities of hard sphere and hard sphere chains of m-mers near a hard wall as well as a 3-mer with a square-well attractive potential near a hard wall or an attractive wall with a square-well potential. The FMT of Hansen-Goos and Roth,[22] which corresponds to a Carnahan-Starling-Boublík fluid, was in better agreement with our hard sphere simulations than the earlier FMT of Roth *et al.*,[13] which corresponds to a Mansoori-Carnahan-Starling-Leland fluid. Slit-shaped pores have been considered for adsorption of 3-mer chains using both square-well attractive and Lennard-Jones wall potentials. Full slit pore density profiles for square-well and Lennard-Jones walls were compared and showed similar general behavior with differences attributable to the range of the potentials. To accomodate full slit-shaped pores, a 3-mer chain was modeled near walls with a 10-4 attractive potential. Surface excess adsorption isotherms were determined for molecules of varying chain lengths inside such a pore.

The new theory should be useful for predicting adsorption on flat surfaces and in slit-shaped pores. A strength of the approach is the ability to compare predictions of the

SAFT-based theory directly with simulation. While we have shown that the theory is in good agreement with the exact results obtained from the simulations for the molecular models studied, how well this approach will describe real fluids at high pressures has yet to be demonstrated. Nevertheless, the agreement between the predictions from the theory and Monte Carlo simulations is encouraging for the treatment of fluids in porous media at high pressures. The theory will be used to describe experimental results in the following chapter.

References

(1) Tarazona, P. Free-Energy Density Functional for Hard Spheres. *Phys. Rev. A*, **1985**, *31*, 2672–2679. Erratum. *Phys. Rev. A*, **1985**, *32*, 3148.

(2) Tarazona, P.; Marini Bettolo Marconi, U.; Evans R. Phase Equilibria of Fluid Interfaces and Confined Fluids. Non-local Versus Local Density Functionals. *Mol. Phys.*, **1987**, *60*, 573–595.

(3) Lastoskie, C.; Gubbins, K. E.; Quirke, N. Pore Size Distribution Analysis of Microporous Carbons: A Density Functional Theory Approach. *J. Phys. Chem.*, **1993**, *97*, 4786–4796.

(4) Valladares, D. L.; Reinoso, F. R.; Zgrablich, G. Characterization of Active Carbons: The Influence of the Method in the Determination of the Pore Size Distribution. *Carbon*, **1998**, *36*, 1491–1499.

(5) El-Merraoui, M.; Aoshima, M.; Kaneko, K. Micropore Size Distribution of Activated Carbon Fiber Using the Density Functional Theory and Other Methods. *Langmuir*, **2000**, *16*, 4300–4304.

(6) Ravikovitch, P. I.; Vishnyakov, A.; Neimark, A. V. Density Functional Theories and Molecular Simulations of Adsorption and Phase Transitions in Nanopores. *Phys. Rev. E*, **2001**, *64*, 011602.

(7) Ohba, T.; Nicholson, D.; Kaneko, K. Temperature Dependence of Micropore Filling of N_2 in Slit-Shaped Carbon Micropores: Experiment and Grand Canonical Monte Carlo Simulation. *Langmuir*, **2003**, *19*, 5700–5707.

(8) Jagiello, J.; Thommes, M. Comparison of DFT Characterization Methods Based on N_2, Ar, CO_2, and H_2 Adsorption Applied to Carbons with Various Pore Size Distributions. *Carbon*, **2004**, *42*, 1227–1232.

(9) Nguyen, T. X.; Bhatia, S. K. Probing the Pore Wall Structure of Nanoporous Carbons Using Adsorption. *Langmuir*, **2004**, *20*, 3532–3535.

(10) Ustinov, E. A.; Do, D. D. Application of Density Functional Theory to Analysis of Energetic Heterogeneity and Pore Size Distribution of Activated Carbon. *Langmuir*, **2004**, *20*, 3791–3797.

(11) Rosenfeld, Y. Free-Energy Model for the Inhomogeneous Hard-Sphere Fluid Mixture and Density-Functional Theory of Freezing. *Phys. Rev. Lett.*, **1989**, *63*, 980–983.

(12) Rosenfeld, Y.; Schmidt, M.; Lowen, H.; Tarazona, P. Fundamental-Measure Free-Energy Density Functional for Hard Spheres: Dimensional Crossover and Freezing. *Phys. Rev. E*, **1997**, *55*, 4245–4263.

(13) Roth, R.; Evans, R.; Lang, A.; Kahl, G. Fundamental Measure Theory for Hard-Sphere Mixtures Revisited: the White Bear Version. *J. Phys.: Condens. Matter*, **2002**, *14*, 12063–12078.

(14) Hansen-Goos, H.; Roth, R. Density Functional Theory for Hard Sphere Mixtures: the White Bear Version Mark II. *J. Phys.: Condens. Matter*, **2006**, *18*, 8413–8425.

(15) Roth, R. Fundamental Measure Theory for Hard-Sphere Mixtures: A Review. *J. Phys.: Condens. Matter*, **2010**, *22*, 063102.

(16) Bryk, P.; Roth, R.; Mecke, K. R.; Dietrich, S. Hard-Sphere Fluids in Contact with Curved Substrates. *Phys. Rev. E*, **2003**, *68*, 031602.

(17) Figueroa-Gerstenmaier, S.; Blas, F. J.; Avalos, J. B.; Vega, L. F. Application of the Fundamental Measure Density Functional Theory to the Adsorption in Cylindrical Pores. *J. Chem. Phys.*, **2003**, *118*, 830–842.

(18) Kierlik, E.; Rosinberg, M. L.; Fan, Y.; Monson, P. A. Prewetting at a Liquid Mixture-Solid Interface: A Comparison of Monte Carlo Simulations with Mean Field Density Functional Theory. *J. Chem. Phys.*, **1994**, *101*, 10947–10952.

(19) Malijevsky, A. Fundamental Measure Theory in Cylindrical Geometry. *J. Chem. Phys.*, **2007**, *126*, 134710.

(20) Evans, R. *Fundamentals of Inhomogeneous Fluids*; Marcel Dekker: New York, 1992.

(21) Evans, R. *Density Functional Theory for Inhomogeneous Fluids I: Simple Fluids in Equilibrium*; 3rd Warsaw School of Statistical Physics: Warsaw University Press, 2010.

(22) Wertheim, M. S. Fluids with Highly Directional Attractive Forces. I. Statistical Thermodynamics. *J. Stat. Phys.*, **1984**, *35*, 19–34.

(23) Wertheim, M. S. Fluids with Highly Directional Attractive Forces. II. Thermodynamic Perturbation Theory and Integral Equations. *J. Stat. Phys.*, **1984**, *35*, 35–47.

(24) Wertheim, M. S. Fluids with Highly Directional Attractive Forces. III. Multiple Attraction Sites. *J. Stat. Phys.*, **1986**, *42*, 459–476.

(25) Wertheim, M. S. Fluids with Highly Directional Attractive Forces. IV. Equilibrium Polymerization. *J. Stat. Phys.*, **1986**, *42*, 477–492.

(26) McCabe, C.; Galindo, A.; Gil-Villegas, A.; Jackson, G. Predicting the High-Pressure Phase Equilibria of Binary Mixtures of n-Alkanes Using the SAFT-VR Approach. *Int. J. Thermophys.*, **1998**, *19*, 1511–1522.

(27) McCabe, C.; Gil-Villegas, A.; Jackson, G. Predicting the High-Pressure Phase Equilibria of Methane + n-Hexane Using the SAFT-VR Approach. *J. Phys. Chem. B*, **1998**, *102*, 4183–4188.

(28) McCabe, C.; Galindo, A.; Gil-Villegas, A.; Jackson, G. Predicting the High-Pressure Phase Equilibria of Binary Mixtures of Perfluoro-n-Alkanes Plus n-Alkanes Using the SAFT-VR Approach. *J. Phys. Chem. B*, **1998**, *102*, 8060–8069.

(29) Galindo, A.; Gil-Villegas, A.; Whitehead, P. J.; Jackson, G.; Burgess, A. N. Prediction of Phase Equilibria for Refrigerant Mixtures of Difluoromethane (HFC-32), 1,1,1,2-Tetrafluoroethane (HFC-134a), and Pentafluoroethane (HFC-125a) Using SAFT-VR. *J. Phys. Chem. B*, **1998**, *102*, 7632–7639.

(30) Jackson, G.; Chapman, W. G.; Gubbins, K. E. Phase Equilibria of Associating Fluids: Spherical Molecules with Multiple Bonding Sites. *Mol. Phys.*, **1988**, *65*, 1–31.

(31) Chapman, W. G.; Jackson, G.; Gubbins, K. E. Phase Equilibria of Associating Fluids: Chain Molecules with Multiple Bonding Sites. *Mol. Phys.*, **1988**, *65*, 1057–1079.

(32) Huong, S. H.; Radosz, M. Equation of State for Small, Large, Polydisperse, and Associating Molecules. *Ind. Eng. Chem. Res.*, **1990**, *29*, 2284–2294.

(33) Johnson, J. K.; Muller, E. A.; Gubbins, K. E. Equation of State for Lennard-Jones Chains. *J. Phys. Chem.*, **1994**, *98*, 6413–6419.

(34) Blas, F. J.; Vega, L. F. Thermodynamic Behaviour of Homonuclear and Heteronuclear Lennard-Jones Chains with Association Sites from Simulation and Theory. *Mol. Phys.*, **1997**, *92*, 135–150.

(35) Gil-Villegas, A.; Galindo, A.; Whitehead, P. J.; Mills, S. J.; Jackson, G.; Burgess, A. N. Statistical Associating Fluid Theory for Chain Molecules with Attractive Potentials of Variable Range. *J. Chem. Phys.*, **1997**, *106*, 4168–4186.

(36) Gross, J.; Sadowski, G. Perturbed-Chain SAFT: An Equation of State Based on a Perturbation Theory for Chain Molecules. *Ind. Eng. Chem. Res.*, **2001**, *40*, 1244–1260.

(37) Pedrosa, N.; Vega, L. F.; Coutinho, J. A. P.; Marrucho, I. M. Phase Equilibria Calculations of Polyethylene Solutions from SAFT-Type Equations of State. *Macromolecules*, **2006**, *39*, 4240–4246.

(38) Watson, G.; Lafitte, T.; Zeberg-Mikkelsen, C. K.; Baylaucq, A.; Bessieres, D.; Boned, C. Volumetric and Derivative Properties Under Pressure for the System 1-Propanol Plus Toluene: A Discussion of PC-SAFT and SAFT-VR. *Fluid Phase Equilib.*, **2006**, *247*, 121–134.

(39) Haslam, A. J.; von Solms, N.; Adjiman, C. S.; Galindo, A.; Jackson, G.; Paricaud, P.; Michelsen, M. L.; Kontogeorgis, G. M. Predicting Enhanced Absorption of Light Gases in Polyethylene Using Simplified PC-SAFT and SAFT-VR. *Fluid Phase Equilib.*, **2006**, *243*, 74–91.

(40) Watson, G.; Lafitte, T.; Zeberg-Mikkelsen, C. K.; Baylaucq, A.; Bessieres, D.; Boned, C. Volumetric and Derivative Properties Under Pressure for the System 1-Propanol Plus Toluene: A Discussion of PC-SAFT and SAFT-VR (Vol 247, pg 121, 2006). *Fluid Phase Equilib.*, **2007**, *253*, 80–80.

(41) Castro-Marcano, F.; Olivera-Fuentes, C. G.; Colina, C. M. Joule-Thomson Inversion Curves and Third Virial Coefficients for Pure Fluids from Molecular-Based Models *Ind. Eng. Chem. Res.*, **2008**, *47*, 8894–8905.

(42) Courtial, X.; Soo, C. B.; Coquelet, C.; Paricaud, P.; Ramjugernath, D.; Richon, D. Vapor-Liquid Equilibrium in the n-Butane Plus Methanol System, Measurement and Modeling from 323.2 to 443.2 K. *Fluid Phase Equilib.*, **2009**, *277*, 152–161.

(43) McCabe, C.; Galindo, A. "SAFT Associating Fluids and Fluid Mixtures," in *Applied Thermodynamics of Fluids*; edited by Goodwin, A. R. H.; Sengers, J. V.; Peters, C. J. Roy. Soc. Chem.: London, 2010.

(44) Zhao, H. G.; McCabe, C. Phase Behavior of Dipolar Fluids from a Modified Statistical Associating Fluid Theory for Potentials of Variable Range. *J. Chem. Phys.*, **2006**, *125*, 4504–4515.

(45) Zhao, H. G.; dos Ramos, M. C.; McCabe, C. Development of an Equation of State for Electrolyte Solutions by Combining the Statistical Associating Fluid Theory and the Mean Spherical Approximation for the Nonprimitive Model. *J. Chem. Phys.*, **2007**, *126*, 244503.

(46) Zhao, H. G.; Ding, Y.; McCabe, C. Phase Behavior of Dipolar Associating Fluids from the SAFT-VR+D Equation of State. *J. Chem. Phys.*, **2007**, *127*, 084514.

(47) Lymperiadis, A.; Adjiman, C. S.; Galindo, A.; Jackson, G. A Group Contribution Method for Associating Chain Molecules Based on the Statistical Associating Fluid Theory (SAFT-gamma). *J. Chem. Phys.*, **2007**, *127*, 234903.

(48) McCabe, C.; Jackson, G. SAFT-VR Modelling of the Phase Equilibrium of Long-Chain n-Alkanes. *Phys. Chem. Chem. Phys.*, **1999**, *1*, 2057–2064.

(49) McCabe, C.; Galindo, A.; Garcia-Lisbona, M. N. Examining the Adsorption (Vapor-Liquid Equilibria) of Short-Chain Hydrocarbons in Low-Density Polyethylene with the SAFT-VR Approach. *Ind. Eng. Chem. Res.*, **2001**, *40*, 3835–3842.

(50) Paricaud, P.; Galindo, A.; Jackson, G. Modeling the Cloud Curves and the Solubility of Gases in Amorphous and Semicrystalline Polyethylene with the SAFT-VR Approach and Flory Theory of Crystallization. *Ind. Eng. Chem. Res.*, **2004**, *43*, 6871-6889.

(51) Yethiraj, A.; Woodward, C. E. Monte Carlo Density Functional Theory of Nonuniform Polymer Melts. *J. Chem. Phys.*, **1995**, *102*, 5499–5505.

(52) Forsman, J.; Woodward, C. E. An Improved Density Functional Description of Hard Sphere Polymer Fluids at Low Density. *J. Chem. Phys.*, **2003**, *119*, 1889–1892.

(53) Blas, F. J.; del Rio, E. M.; de Miguel, E.; Jackson, G. An Examination of the Vapour-Liquid Interface of Associating Fluids Using a SAFT-DFT Approach. *Mol. Phys.*, **2001**, *99*, 1851–1865.

(54) Gloor, G. J.; Blas, F. J.; del Rio, E. M.; de Miguel, E.; Jackson, G. A SAFT-DFT Approach for the Vapour-Liquid Interface of Associating Fluids. *Fluid Phase Equilib.*, **2002**, *194*, 521–530.

(55) Gloor, G. J.; Jackson, G.; Blas, F. J.; del Rio, E. M.; de Miguel, E. An Accurate Density Functional Theory for the Vapor-Liquid Interface of Associating Chain Molecules Based on the Statistical Associating Fluid Theory for Potentials of Variable Range. *J. Chem. Phys.*, **2004**, *121*, 12740–12759.

(56) Gloor, G. J.; Jackson, G.; Blas, F. J.; del Rio, E. M.; de Miguel, E. Prediction of the Vapor-Liquid Interfacial Tension of Nonassociating and Associating Fluids with the SAFT-VR Density Functional Theory. *J. Chem. Phys.*, **2007**, *111*, 15513–15522.

(57) Georgiadis, A.; Llovell, F.; Bismarck, A.; Blas, F. J.; Galindo, A.; Maitland, G. C.; Trusler, J. P. M.; Jackson, G. Interfacial Tension Measurements and Modelling of (Carbon Dioxide Plus n-Alkane) and (Carbon Dioxide Plus Water) Binary Mixtures at Elevated Pressures and Temperatures. *J. Supercrit. Fluids*, **2010**, *55*, 743–754.

(58) Llovell, F.; Galindo, A.; Blas, F. J.; Jackson, G. Classical Density Functional Theory for the Prediction of the Surface Tension and Interfacial Properties of Fluids Mixtures of Chain Molecules Based on the Statistical Associating Fluid Theory for Potentials of Variable Range. *J. Chem. Phys.*, **2010**, *133*, 024704.

(59) Llovell, F.; MacDowell, N.; Galindo, A.; Blas, F. J.; Jackson, G. Application of the SAFT-VR Density Functional Theory to the Prediction of the Interfacial Properties of Mixtures of Relevance to Reservoir Engineering. *Fluid Phase Equilib.*, **2012**, *336*, 137–150.

(60) Yu, Y. X.; Wu, J. Z. A Fundamental-Measure Theory for Inhomogeneous Associating Fluids. *J. Chem. Phys.*, **2002**, *116*, 7094–7103.

(61) Yu, Y. X.; Wu, J. Z. Density Functional Theory for Inhomogeneous Mixtures of Polymeric Fluids. *J. Chem. Phys.*, **2002**, *117*, 2368–2376.

(62) Yu, Y. X.; Wu, J. Z.; Xin, Y. X.; Gao, G. H. Structures and Correlation Functions of Multicomponent and Polydisperse Hard-Sphere Mixtures from a Density Functional Theory. *J. Chem. Phys.*, **2004**, *121*, 1535–1541.

(63) Bryk, P.; Sokolowski, S.; Pizio, O. Density Functional Theory for Inhomogeneous Associating Chain Fluids. *J. Chem. Phys.*, **2006**, *125*, 024909.

(64) Ye, Z. C.; Cai, J.; Liu, H. L.; Hu, Y. Density and Chain Conformation Profiles of Square-Well Chains Confined in a Slit by Density-Functional Theory. *J. Chem. Phys.*, **2005**, *123*, 194902.

(65) Ye, Z. C.; Chen, H. Y.; Liu, H. L.; Hu, Y.; Jiang, J. W. Density Functional Theory for Copolymers Confined in a Nanoslit. *J. Chem. Phys.*, **2007**, *126*, 134903.

(66) Tripathi, S.; Chapman, W. G. Microstructure of Inhomogeneous Polyatomic Mixtures from a Density Functional Formalism for Atomic Mixtures. *J. Chem. Phys.*, **2005**, *122*, 094506.

(67) Jain, S.; Dominik, A.; Chapman, W. G. Modified Interfacial Statistical Associating Fluid Theory: A Perturbation Density Functional Theory for Inhomogeneous Complex Fluids. *J. Chem. Phys.*, **2007**, *127*, 244904.

(68) Carnahan N. F.; Starling, K. E. Equation of State for Nonattracting Rigid Spheres. *J. Chem. Phys.*, **1969**, *51*, 635–636.

(69) Chang, J.; Sandler, S. I. A Real Functional Representation for the Structure of the Hard-Sphere Fluid. *Mol. Phys.*, **1994**, *81*, 735–744.

(70) Verlet, L.; Weis, J. J. Equilibrium Theory of Simple Liquids. *Phys. Rev. A*, **1972**, *5*, 939–952.

(71) Patel, B. H.; Docherty, H.; Varga, S.; Galindo, A.; Maitland, G. C. Generalized Equation of State for Square-Well Potentials of Variable Range. *Mol. Phys.*, **2005**, *103*, 129–139.

(72) Barker, J. A.; Henderson, D. Pertubation Theory and Equation of State for Fluids: The Square-Well Fluid. *J. Chem. Phys.*, **1967**, *47*, 2856–2861.

(73) Barker, J. A.; Henderson, D. What is "Liquid"? Understanding the States of Matter. *Rev. Mod. Phys.*, **1976**, *48*, 587-671.

(74) Zhang, B. J. Calculating Thermodynamic Properties from Perturbation Theory II. An Analytical Representation of Square-Well Chain Fluid. *Fluid Phase Equil.*, **2001**, *180*, 182–194.

(75) Prausnitz, J. M.; Lichtenthaler, R. N.; de Azevedo, E. G. *Molecular Thermodynamics of Fluid-Phase Equilibria: third edition*; Prentice Hall: New Jersey, 1999.

(76) Steele, W. A. The Physical Interaction of Gases with Crystalline Solids. I. Gas-Solid Energies and Properties of Isolated Adsorbed Atoms. *Surf. Sci.*, **1973**, *36*, 317–352.

(77) Tjatjopoulos, G. J.; Feke, D. L.; Mann, J. A. Molecule-Micropore Interaction Potentials. *J. Phys. Chem.*, **1988**, *92*, 4006–4007.

(78) Snook, I. K.; Henderson, D. Monte Carlo Study of a Hard-Sphere Fluid Near a Hard Wall. *J. Chem. Phys.*, **1978**, *68*, 2134–2139.

(79) Kierlik, E.; Rosinberg, M. L. Perturbation Density Functional Theory for Polyatomic Fluids. III. Applications to Hard Chain Molecules in Slitlike Pores. *J. Chem. Phys.*, **1978**, *100*, 1716–30.

(80) Dickman, R.; Hall, C. K. High Density Monte Carlo Simulations of Chain Molecules: Bulk Equation of State and Density Profiles Near Walls. *J. Chem. Phys.*, **1988**, *89*, 3168–3174.

(81) Anderson, D. G. Iterative Procedures for Nonlinear Integral Equations. *J. Assoc. Comp. Mach.*, **1965**, *12*, 547–560.

(82) Eyert, V. A Comparative Study of Methods for Convergence Acceleration of Iterative Vector Sequences. *J. Comp. Phys.*, **1996**, *124*, 271–285.

CHAPTER V

APPLICATION OF THE SAFT-FMT-DFT APPROACH TO ADSORPTION EQUILIBRIUM DATA: PREDICTION OF PORE SIZE DISTRIBUTIONS AND EXCESS ISOTHERMS

Classical density functional theory (DFT) has important applications in characterizing adsorbent materials and predicting adsorption equilibrium. The most common usage is in the determination of the pore size distribution of an adsorbent, which is performed by first calculating fluid densities for different pore sizes and then developing a pore size distribution that sums the individual pore isotherms to match an experimental cryogenic adsorption isotherm.[1–5] DFT has also been used to model adsorption isotherms of various fluids on activated carbons and other materials at and above cryogenic temperatures by calculating individual pore isotherms and summing them at selected pressures according to a known pore size distribution.[6–13]

There have been advances in DFT involving modeling more complex mixtures, including the incorporation of chain molecules. This can be accomplished through the use of an accurate equation of state-based approach to describe the chain molecules, such as the statistical associating fluid theory (SAFT).[14–17] Chapman and coworkers[18,19] developed an interfacial statistical associating fluid theory (iSAFT) to model bulk and interfacial adsorption properties by combining a DFT based on the original fundamental measure theory (FMT) for monomers[20,21] with bulk fluid properties obtained from SAFT. There has also been a DFT that uses the newest version of FMT[22] and a version of SAFT based on the statistical associating fluid theory of variable range (SAFT-VR)[3] to model chain molecules inside slit pores.[24]

In this chapter, we use our SAFT-FMT-DFT approach[24] to model the density profiles

of nitrogen and n-pentane in carbon parallel slit pores. An experimental isotherm for nitrogen adsorption is used with the simulated single pore nitrogen isotherms to calculate a pore size distribution for BPL activated carbon. This pore size distribution is used with the simulated n-pentane isotherms to predict an excess isotherm for n-pentane on the carbon, which is compared with a unique experimental n-pentane isotherm[25] that extends down to low loadings in the Henry's law region.

5.1 Theory

Model

Density functional theory is used in this chapter to calculate the density profile that minimizes the grand potential function $\Omega[\rho_m(\mathbf{R})]$, where $\rho_m(\mathbf{R})$ is the density profile of a chain molecule as a function of segment position $\mathbf{R} \equiv (\mathbf{r}_1, \mathbf{r}_2, \cdots, \mathbf{r}_m)$ and m is the number of segments in the chain. This is done by setting the functional derivative with respect to the density equal to zero. The grand potential is calculated by

$$\Omega[\rho_m(\mathbf{R})] = F[\rho_m(\mathbf{R})] + \int \rho_m(\mathbf{R}) \left[V_{ext}(\mathbf{R}) - \mu\right] d\mathbf{R} \tag{5.1}$$

where $F[\rho_m(\mathbf{R})]$ is the Helmholtz free energy, μ is the chemical potential for the chain molecule, and $V_{ext}(\mathbf{R})$ is the external potential. Using the general formulation of SAFT, we write the Helmholtz free energy and the chemical potential from SAFT as

$$F = F_{id} + F_{hs} + F_1 + F_2 + F_{chain} \tag{5.2}$$

The general development of the SAFT-FMT-DFT approach has been published recently[24] and will not be reproduced here. We describe below only specific details associated with the application of the theory to the systems considered in this chapter.

The hard sphere repulsive term is calculated using the improved FMT of Hansen-Goos and Roth[22] for a Carnahan-Starling-Boublík (CSB) fluid. The chain term was developed by Yu and Wu[4] for a hard sphere chain. The attractive terms use a perturbation analysis expanded out to second order, rather than a mean field assumption.

The external potential for the carbon is described by

$$V_{ext} = \phi_{sf}(z) \tag{5.3}$$

for a planar wall and by

$$V_{ext} = \phi_{sf}(z) + \phi_{sf}(H - z) \tag{5.4}$$

for a slit-pore of width H, where $\phi_{sf}(z)$ is given by the 10-4-3 potential[27]

$$\phi_{sf}(z) = 2\pi\epsilon_{sf}\rho_s\sigma_{sf}^2\Delta\left[\frac{2}{5}\left(\frac{\sigma_{sf}}{z}\right)^{10} - \left(\frac{\sigma_{sf}}{z}\right)^{4} - \frac{\sigma_{sf}^4}{3\Delta(z+0.61\Delta)^3}\right] \tag{5.5}$$

with $\rho_s = 0.114$ Å^{-3} and $\Delta = 3.35$ Å.

Taking the functional derivative of eq. 5.1 and rearranging results in the equation used to calculate the segment equilibrium density profile:

$$\rho(z) = \frac{1}{\Lambda^3}\exp(\mu)\sum_{i=1}^{m}\exp\left[-\frac{\psi(z)}{kT}\right]G^i(z)\,G^{m+1-i}(z) \tag{5.6}$$

The solution method involves iterating on the segment density. In eq. 5.6, we have

$$\psi(z) = \frac{\delta F_{hs}}{\delta\rho(\mathbf{r})} + \frac{\delta F_1}{\delta\rho(\mathbf{r})} + \frac{\delta F_2}{\delta\rho(\mathbf{r})} + \frac{\delta F_{chain}}{\delta\rho(\mathbf{r})} + V_{ext} \tag{5.7}$$

and

$$G^i = \int\exp\left[-\frac{\psi(z)}{kT}\right]\frac{\Theta(\sigma_{ff} - |z - z'|)}{2\sigma_{ff}}\,G^{i-1}dz' \tag{5.8}$$

where $G^1(z) = 1$. Due to the summation in eq. 5.6, the value of the parameter m is limited to integer values.

The equilibrium value of the density, calculated from eq. 5.6, is then used to calculate the excess density in the pore using

$$\rho(H,P) = \frac{1}{H}\int_0^H\left[\frac{\rho(z)}{m} - \rho_b\right]dz \tag{5.9}$$

where ρ_b is the bulk density. The excess density is calculated as a function of pore widths H and pressures P.

The pore size distribution of the material is determined implicitly by comparing experimental isotherm data with the calculated isotherm, which is obtained by integrating the excess densities in pores over the range of pore widths and pressures using the adsorption integral equation

$$n(P) = \int_0^\infty \rho(H, P) f(H) dH \tag{5.10}$$

where $f(H)$ is the pore size distribution. The model used for the pore size distribution is a log normal distribution

$$f(H) = \frac{1}{\sqrt{2\pi}\, H} \sum_{i=1}^{M} \frac{\alpha_i}{\gamma_i} \exp\left[-\frac{(\ln H - \beta_i)^2}{2\gamma_i^2} \right] \tag{5.11}$$

where M is the number of modes and α_i, β_i, and γ_i are parameters.

Parameter Estimation for Real Fluids

The parameters for the model are in two different categories, fluid-fluid interactions and fluid-solid interactions. They are given in Table 5.1 for nitrogen and n-pentane and were determined by two different methods. The fluid-fluid parameters were estimated using the saturated vapor pressure curve and the vapor-liquid coexistence curve. Following Lastoskie *et al.*[1] and others, the fluid-solid molecular diameter σ_{sf} was calculated using the Lorentz-Berthelot mixing rules (arithmetic mean) using the fluid-fluid molecular diameter σ_{ff} and the solid molecular diameter $\sigma_s = 3.380$ Å. The solid-fluid potential ϵ_{sf} was determined by fitting the onset of the monolayer transition to experimental data for adsorption on a planar non-porous carbon wall. Results for parameter estimation will be discussed in the next sections.

Table 5.1: Model parameters

molecule	σ_{ff} (Å)	ϵ_{ff}/k (K)	λ	M	σ_{sf} (Å)	ϵ_{sf}/k (K)
nitrogen	2.657	40.282	1.83	2	3.0185	42.98
n-pentane	2.791	57.083	2.163	5	3.086	74.63

5.2 Results and Discussion

Nitrogen

The fluid-solid parameters for nitrogen were determined using data of Kruk *et al.*[28] for adsorption of nitrogen on Carbopack F, a commercially available graphitized carbon black with a BET surface area of 6.2 m^2/g at 77K. A wide pore of width $H = 40\,\sigma_{ff}$ was used to simulate a non-porous surface, with adsorption on each wall being unaffected by the presence of the other wall. Results are shown in Fig. 5.1. The solid-fluid potential parameters chosen were the values that best described the curve up to reduced pressures of 4×10^{-3}, which encompasses the range of the experimental data for adsorption of nitrogen on BPL activated carbon.

Nitrogen density profiles were obtained by solving eq. 5.6 for many pore sizes at many pressures. Fig. 5.2 shows the profiles for three different pore sizes, each at three different pressures: one before the monolayer transition, one after the monolayer transition, and one after pore condensation. Pores widths are 8.77 Å, 10.63 Å, and 11.03 Å, which correspond to $3.3\,\sigma_{ff}$, $4.0\,\sigma_{ff}$, and $4.15\,\sigma_{ff}$, with pore walls placed at $z = 0$ and $z = X\sigma_{ff}$ where X is 3.3, 4.0, or 4.15. Figs. 5.2a–c show density profiles that are below the monolayer transition at a reduced pressure of 1.0×10^{-6}. It should be noted in these figures that the first peak does not occur at $z = \sigma_{ff}$, because the solid and the fluid segments have different sizes, with $\sigma_{sf} = 3.018$ Å and $\sigma_{ff} = 2.657$ Å. Thus, the first peak occurs at a value of z somewhat greater than σ_{ff}, near $z = 1.1\,\sigma_{ff}$. Figs. 5.2d–f show density profiles that are above the monolayer transition at a reduced pressure of 1.0×10^{-5}. In Fig. 5.2d, the peak has narrowed and the height has increased significantly, a result of pore condensation. In contrast, at this pressure the larger pores shown in Figs. 5.2e–f do not show pore condensation. Figs. 5.2g–i show density profiles at a reduced pressure of 1.0×10^{-3}, with pore condensation in all three pores. In Fig. 5.2g, the base of the peak has narrowed considerably and the height has increased.

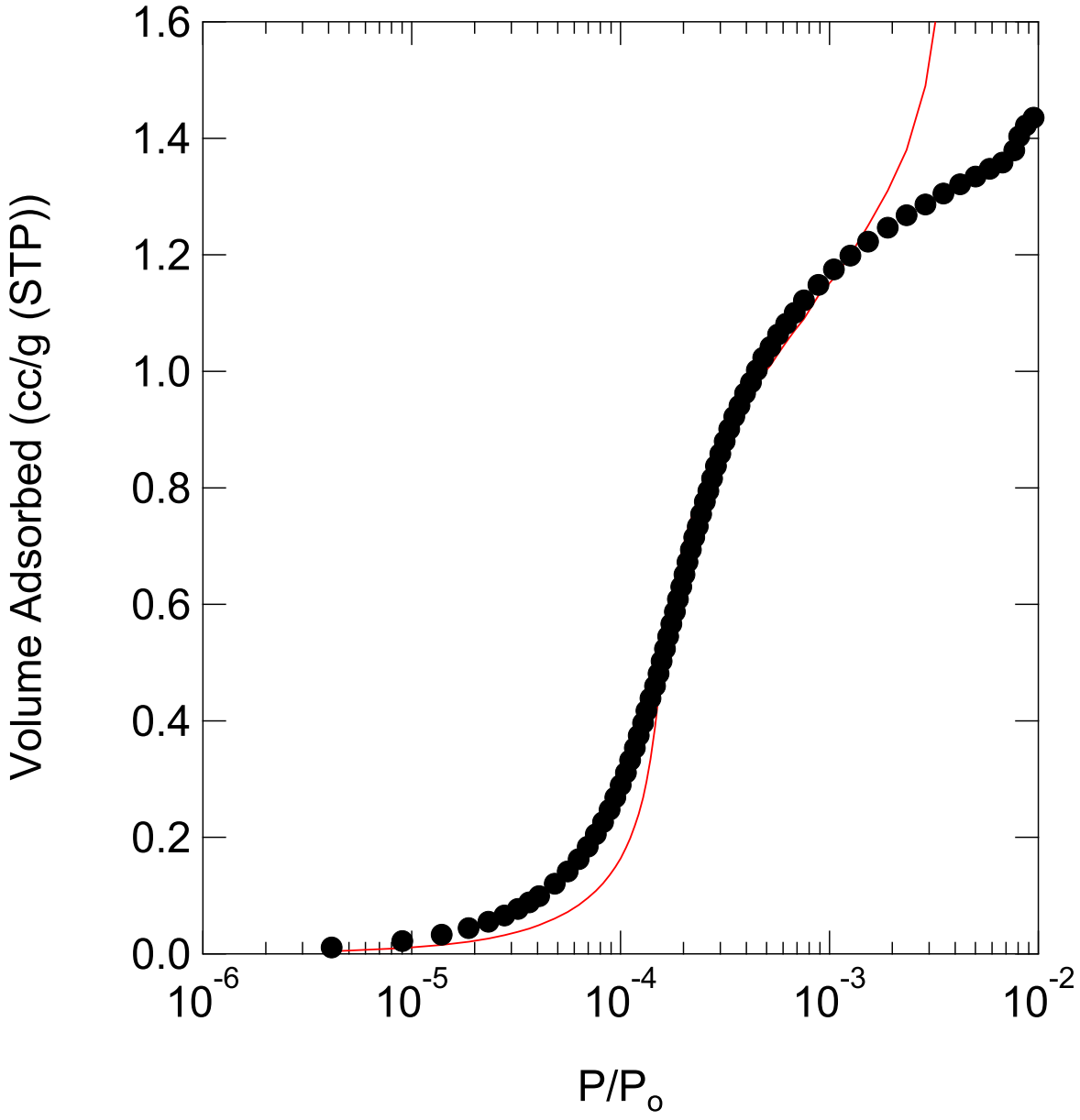

Figure 5.1: Comparison of experimental and theoretical adsorbed volumes of nitrogen on nonporous carbon black at 77 K. The points are experimental data. The solid line is the nitrogen prediction.

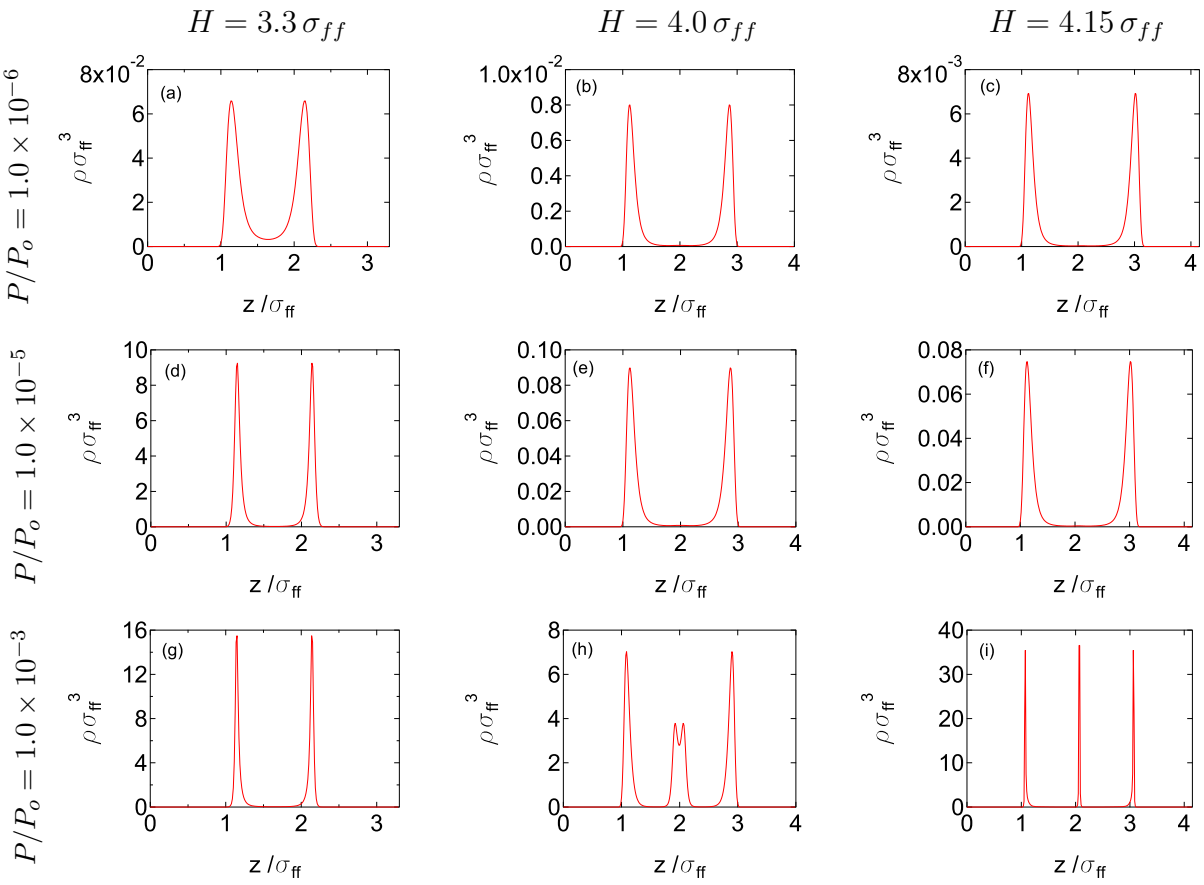

Figure 5.2: Nitrogen density profiles in pores of width 3.3, 4.0, and 4.15 at reduced pressures of 1.0×10^{-6}, 1.0×10^{-5}, and 1.0×10^{-3}. Note the changes in the magnitudes of the densities.

The increase is not as pronounced as the smaller pore that underwent condensation before a reduced pressure of 1.0×10^{-5}. In Fig. 5.2h, the height of the peaks has increased significantly and two smaller peaks have formed in the middle of the pore. These smaller peaks result from the larger peak interacting with its mirror image across the center line of the pore, with the left-center peak associated with the right wall and the right-center peak associated with the left wall. As the pore expands, as shown in Fig. 5.2i, the smaller peaks overlap, resulting in a much higher peaks.

Excess adsorption isotherms for different pore sizes were obtained by determining average excess densities, obtained by integrating the density profiles over the pore widths using eq. 5.9, as a function of reduced pressure. Fig. 5.3 shows the excess densities for nitrogen in pores of width $2.55\,\sigma_{ff}$, $3\,\sigma_{ff}$, $3.5\,\sigma_{ff}$, $4\,\sigma_{ff}$, $5\,\sigma_{ff}$, and $6\,\sigma_{ff}$. The isotherm for the $3\,\sigma_{ff}$ pore shows the monolayer transition occurring at a reduced pressure of 1×10^{-7}, with pore condensation at 4×10^{-7}. The $3.5\,\sigma_{ff}$ pore has a less pronounced monolayer transition at a reduced pressure of 2×10^{-6}, with pore condensation at 5×10^{-6}. The $4\,\sigma_{ff}$ pore isotherm has the monolayer transition at 1×10^{-5} and pore condensation at 3.7×10^{-5}. The isotherms for the $3.5\,\sigma_{ff}$ and $4\,\sigma_{ff}$ pores do cross near a reduced pressure of 3×10^{-4}, because the size of the $3.5\,\sigma_{ff}$ pore is far from an integer value of σ_{ff} and thus inconsistent with the formation of an additional layer of molecules; so, above the monolayer transition, molecules inside the pore are disordered instead of ordered. The $5\,\sigma_{ff}$ pore shows the formation of the monolayer starting at a reduced pressure of 2×10^{-5}, multiple layers forming at 1×10^{-4}, and pore condensation occurring at a reduced pressure of 3.7×10^{-4}. For the $6\,\sigma_{ff}$ pore, the monolayer forms at a reduced pressure of 2×10^{-5}, multiple layers of molecules occur at 1×10^{-4}, and pore condensation occurs at a reduced pressure of 2×10^{-3}. Thus, for adsorption of nitrogen at 77 K in pores up to $4\,\sigma_{ff}\approx1.1$ nm in width, as the pore size increases, the monolayer transition shifts to higher pressures. For pores larger than 1.1 nm, the monolayer transition remains in the same place, but the formation of multiple layers and

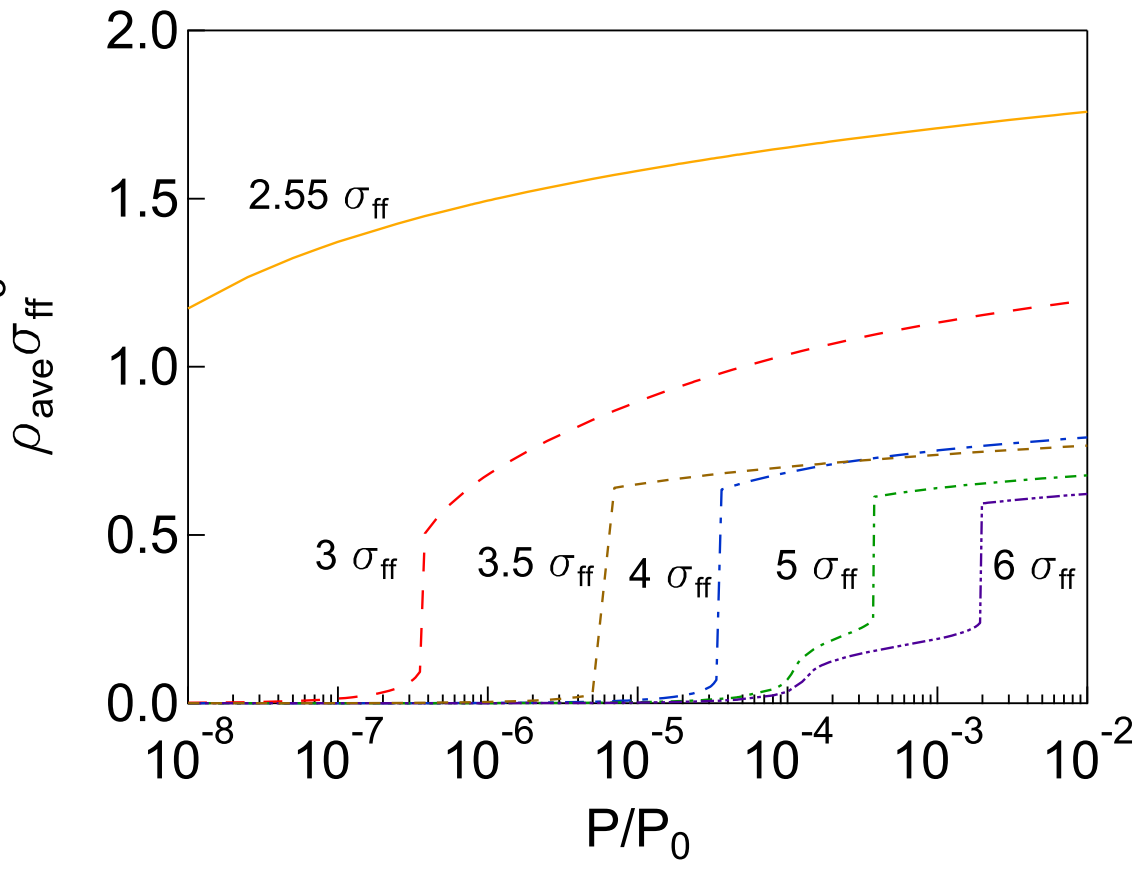

Figure 5.3: Average density of nitrogen pores of increasing width at 77 K.

pore condensation move to higher pressures.

The pore size distribution for BPL activated carbon was determined using the experimental data of Russell and LeVan[29] for adsorption of nitrogen on the adsorbent and is shown in Fig. 5.4. The log normal distribution with three modes, given by eq. 5.11, and thirty-five different pore isotherms like those shown in Fig. 5.3 were used in the calculations. The distribution has a broad peak near 6 Å and a long tail that decreases as pore width increases. The pore size distribution is similar in shape to that calculated by Russell and LeVan[29] from their measured isotherm. They used the single pore isotherms calculated by DFT by Seaton *et al.*,[30] where nitrogen was treated as spherical with a mean field assumption. The calculated pore size distribution had its main peak at 11 Å. However, our individual pore isotherms show higher capacities than those calculated by Russell and LeVan, which leads to lower peak heights in the pore size distribution to give similar overall amounts of nitrogen adsorbed. Fig. 5.5 shows the calculated nitrogen isotherm corresponding to the calculated pore size distribution. The calculated isotherm describes the data well.

Pentane

The data of Avgul and Kiselev[31] for n-pentane adsorbed on a graphite wall were used to estimate the parameters for n-pentane, using the procedure described in the Parameter Estimation Section. The carbon used was a graphitized carbon black with a BET surface area of 12.2 m^2/g. As with nitrogen, a wide pore with a width of $H = 40\ \sigma_{ff}$ was used to simulate a non-porous surface, with results shown in Fig. 5.6 and parameters given in Table 5.1. The parameters were fit emphasizing the lower pressures, noting that the experimental data for adsorption of n-pentane on BPL activated carbon has $P < 10^{-2}$ kPa.

Fig. 5.7 shows the density profiles, calculated using eq. 5.6, for pore widths of 7.81 Å and 8.93 Åat 298.15K. Fig. 5.7 shows the density profiles, calculated using eq. 5.6, for pore widths of 7.81 Å and 8.93 Å. Figs. 5.7a–b show the density profiles of n-pentane at a pressure

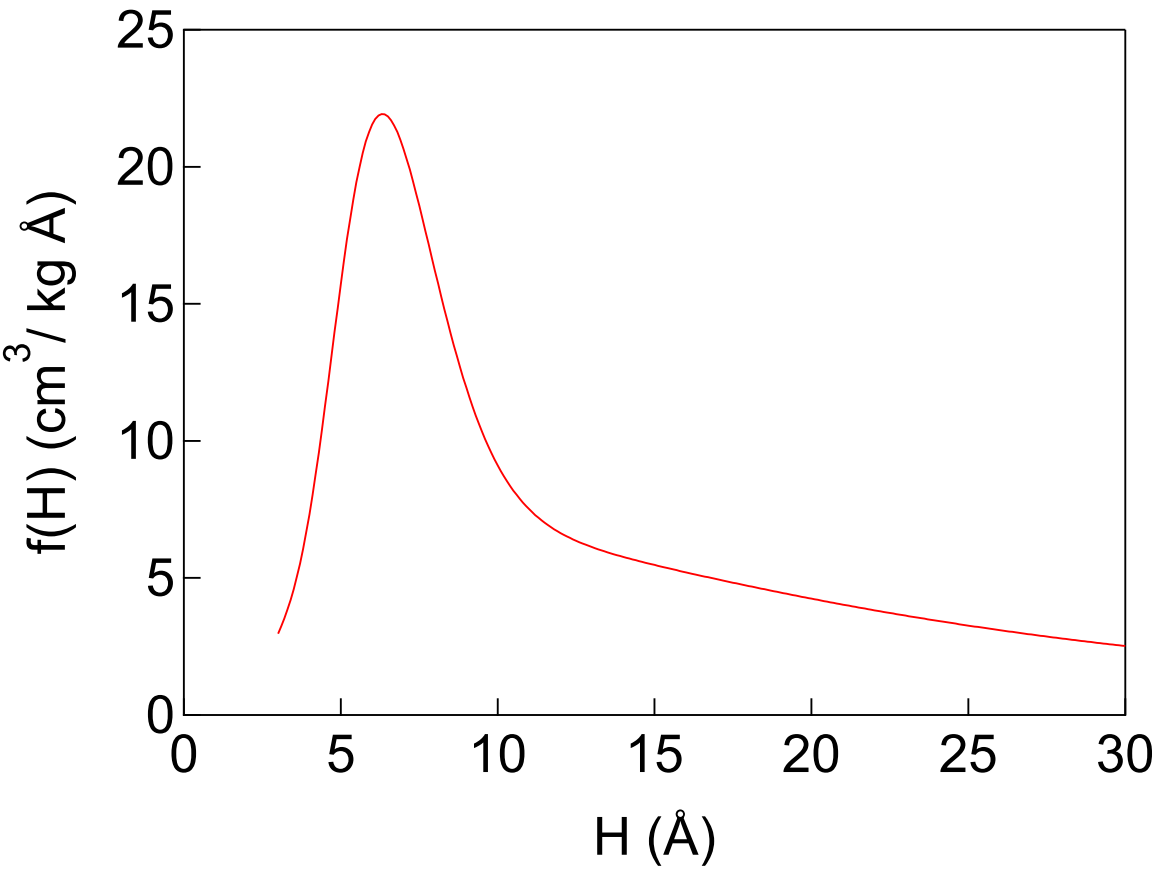

Figure 5.4: Pore size distribution calculated from nitrogen density profiles with three modes in eq. 5.11.

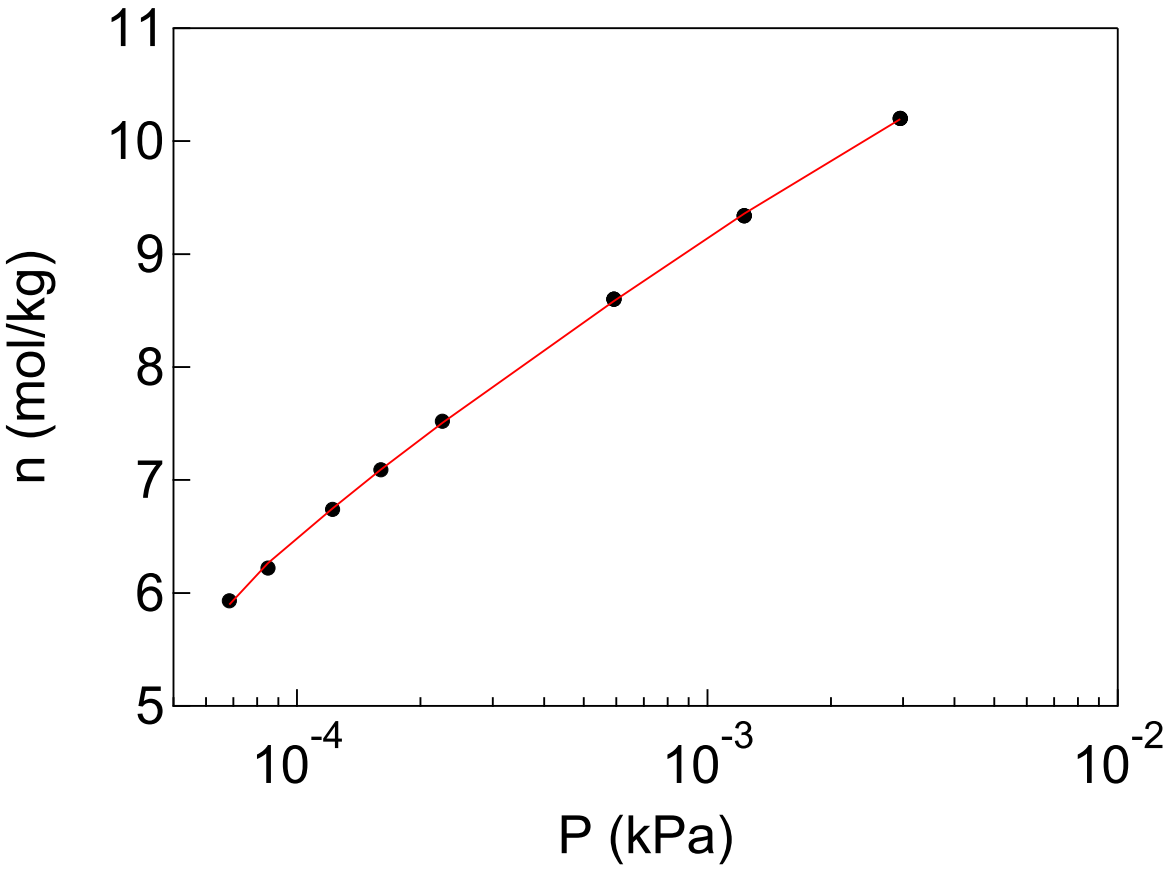

Figure 5.5: Nitrogen isotherm at 77 K on BPL activated carbon. Solid line is the calculated isotherm.

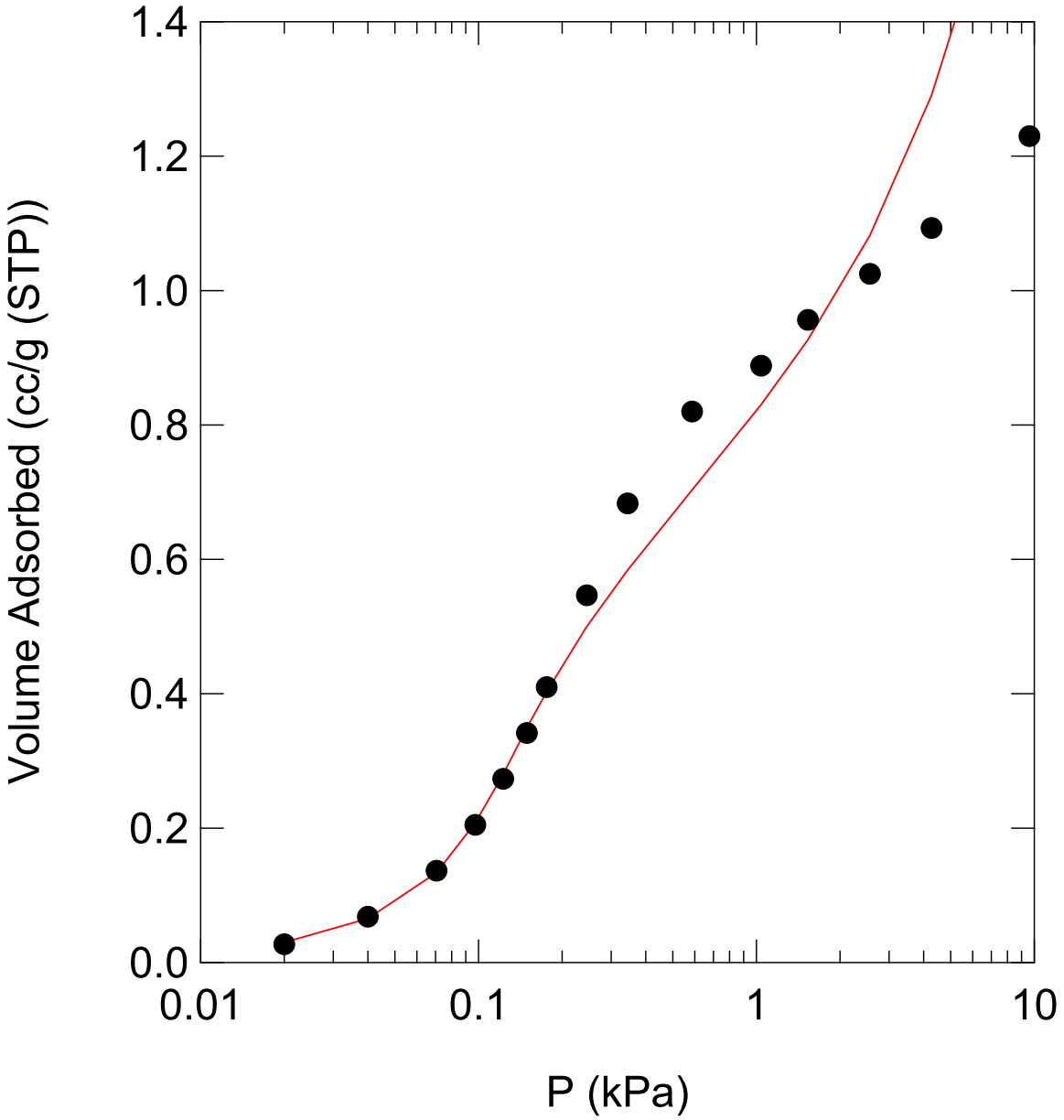

Figure 5.6: Comparison of experimental and theoretical adsorbed volumes of pentane on nonporous carbon black at 293.15 K. The points are experimental data. The solid line is the model predictions.

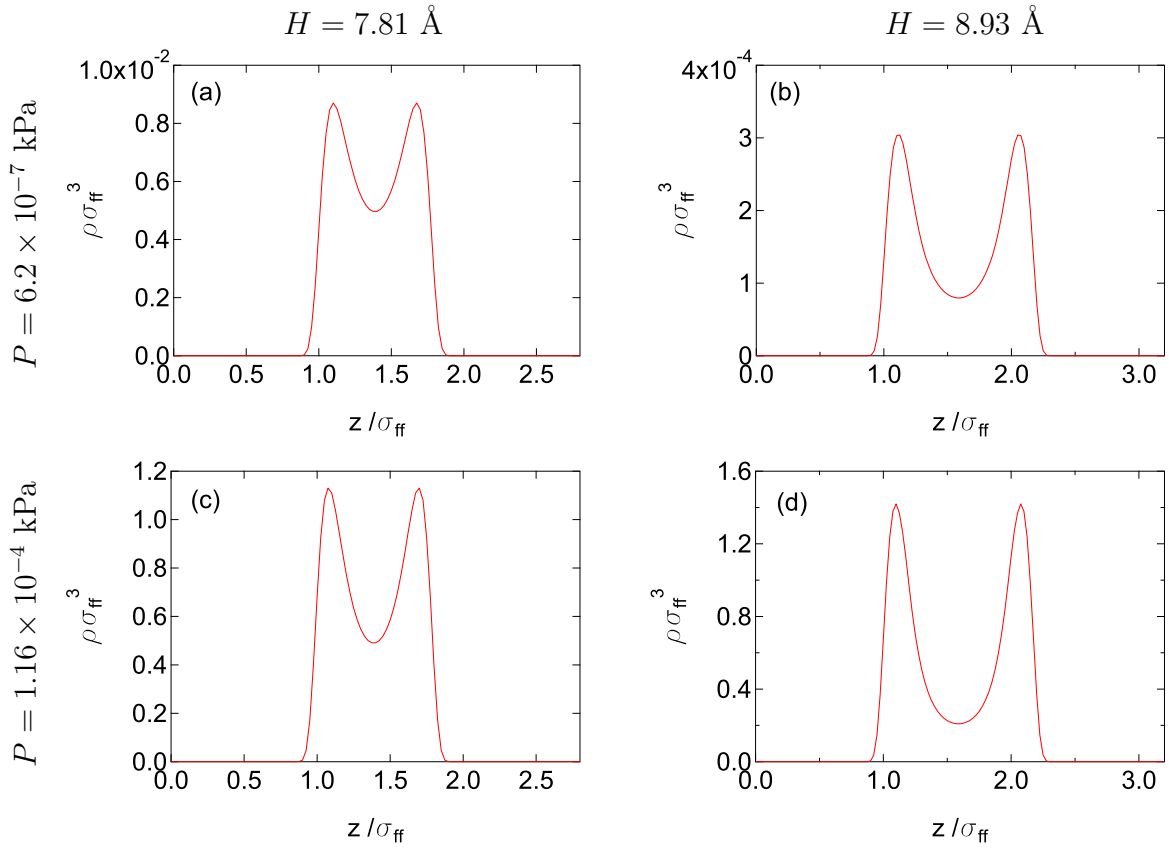

Figure 5.7: n-pentane density profiles in 7.81 Å and 8.93 Å pores at pressures 6.2×10^{-7} kPa and 1.16×10^{-4} kPa.

of 6.2×10^{-7} kPa; the system is well below the monolayer transition. Fig. 5.7c–d shows the density profile at a pressure of 1.16×10^{-4} kPa; at this pressure the system has gone through condensation. Fig. 5.8 shows the average density profiles, calculated with eq. 5.3, for pores of size 8.37 Å, 9.07 Å, and 11.16 Å. The position at which the condensation steps ends in the pores of width 8.37 Å and 9.07 Å, with the isotherms flattening out, are apparent. Also, it can be seen that fluid in the pore of width 11.16 Å does not go through condensation. This follows also for larger pores in the pressure range examined.

Using the pore size distribution determined with nitrogen, an excess isotherm for n-pentane was predicted using the adsorption integral equation, eq. 5.10, and forty-five calculated pore isotherms for n-pentane. This isotherm is shown in Fig.5.9, where it is compared with the experimental data of Schindler *et al.*,[25] which extend to ultra-low concentrations into the Henry's law region. The predicted isotherm transitions smoothly into this linear region and is in generally good agreement with the experimental data.

5.3 Conclusions

This chapter is the first application of the SAFT-FMT-DFT approach to experimental data. The theory was first used to determine interaction parameters of nitrogen and n-pentane with a planar carbon wall. These were used to determine single pore isotherms for the adsorbates. The calculated density profiles for nitrogen show physically expected behavior. When the pore size places the larger density peaks closer than $1\,\sigma_{ff}$ apart in the center of the pore, apparent layering interactions are created. Pore condensation was also observed with the bases of the density peaks narrowing and the heights of the peaks increasing. For n-pentane, pore filling was observed in some pores, but condensation was not found in the larger pores at the pressures considered.

A pore size distribution with an assumed log normal distribution with three modes was determined for BPL activated carbon using experimental data for nitrogen adsorption and

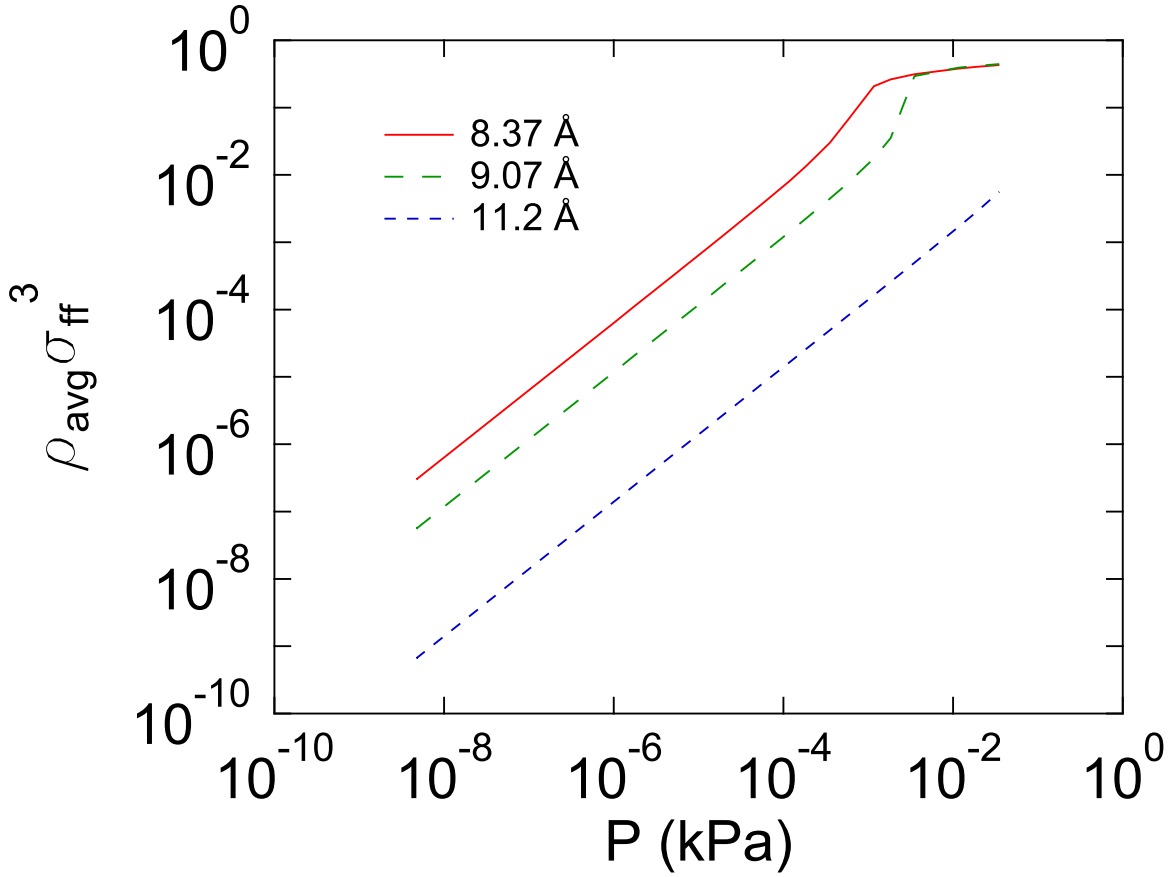

Figure 5.8: Average density of n-pentane in 8.37 Å, 9.07 Å, and 11.2 Å pores at 298.15 K.

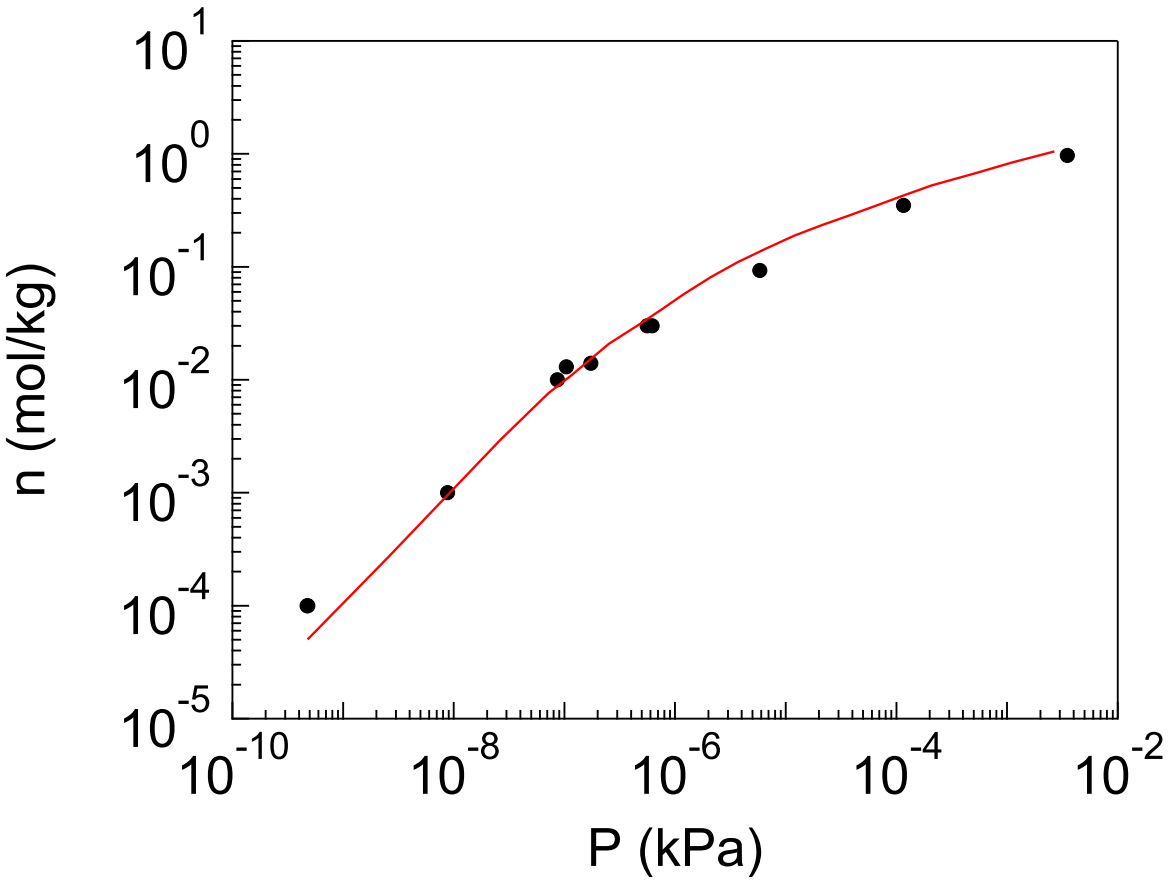

Figure 5.9: Calculated n-pentane isotherm at 25 °Con BPL activated carbon. The circles are the data from Schindler *et al.*[25] The solid line is the isotherm based on the pore size distribution calculated by nitrogen.

the single pore isotherms for nitrogen. The pore size distribution was used with the single pore n-pentane isotherms to predict an n-pentane isotherm for adsorption on BPL activated carbon at 293.15 K. The predicted and measured isotherms compare well.

The SAFT-FMT-DFT approach has been shown to be useful for estimating a pore size distribution from experimental data and calculating an isotherm for a much different type of molecule and temperature using the pore size distribution. The approach can be used to predict the adsorption of many other chain molecules.

References

(1) Lastoskie, C.; Gubbins, K. E.; Quirke, N. Pore Size Distribution Analysis of Microporous Carbons: A Density Functional Theory Approach. *J. Phys. Chem.* **1993**, *97*, 4786–4796.

(2) Lastoskie, C.; Gubbins, K. E.; Quirke, N. Pore Size Heterogeneity and the Carbon Slit Pore: A Denstiy Functional Theory Model. *Langmuir* **1993**, *9*, 2693–2702.

(3) Ryu, Z.; Zheng, J.; Wang, M.; Zhang, B. Characterization of Pore Size Distributions on Carbonaceous Adsorbents by DFT. *Carbon* **1999**, *37*, 1257–1264.

(4) Dombrowski, R. J.; Hyduke, D. R.; Lastoskie, C. M. Pore Size Analysis of Activated Carbons from Argon and Nitrogen Porosimetry Using Density Functional Theory. *Langmuir* **2000**, *16*, 5041–5050.

(5) Ustinov, E. A.; Do, D. D.; Fenelonov, V. B. Pore Size Distribution Analysis of Activated Carbons: Application of Density Functional Theory using Nongraphitized Carbon Black as a Reference System. *Carbon* **2006**, *44*, 653–663.

(6) Ravikovitch, P. I.; Haller, G. L.; Neimark, A. V. Density Functional Theory Model for Calculating Pore Size Distributions: Pore Structure on Nanoporous Catalysts. *Adv. Colloid Interface Sci.* **1998**, *76–77*, 203–226.

(7) Tanaka, H.; El-Merraoui, M.; Steele, W. A.; Kaneko, K. Methane Adsorption on Single-Walled Carbon Nanotube: A Density Functional Theory Model. *Chem. Phys. Lett.* **2002**, *352*, 334–341.

(8) Carati, A.; Ferraris, G.; Guidotti, M.; Moretti, G.; Psaro, R.; Rizzo, C. Preparation and Characterisation of Mesoporous Silica-Alumina and Silica-Titania with a Narrow Pore Size Distribution. *Catal. Today* **2003**, *4*, 315–323.

(9) Figueroa-Gerstenmaier, S.; Bonet Avalos, J.; Gelb, L. D.; Gubbins, K. E.; Vega, L. F. Pore Size Distribution of Porous Glasses: A Test of the Independent Pore Model. *Langmuir* **2003**, *19*, 8592–8604.

(10) Zhang, S.; Shao, T.; Kose, H. S.; Karanfil, T. Adsorption of Aromatic Compounds by Carbonaceous Adsorbents: A Comparative Study on Granular Activated Carbon, Activated Carbon Fiber, and Carbon Nanotubes. *Environ. Sci. Technol.* **2010**, *44*, 6377–6383.

(11) Hornebecq, V.; Knöfel, C.; Boulet, P.; Kuchta, B.; Llewellyn, P. L. Adsorption of Carbon Dioxide on Mesoporous Zirconia: Microcalorimetric Measurements, Adsorption Isotherm Modeling, and Density Functional Theory Calculations. *J. Phys. Chem. C* **2011**, *115*, 10097–10103.

(12) Gor, G. Y.; Thommes, M.; Cychosz, K. A.; Neimark, A. V. Quenched Solid Density Functional Theory Method for Characterization of Mesoporous Carbons by Nitrogen Adsorption. *Carbon* **2012**, *50*, 1583–1590.

(13) Landers, J.; Gor, G. Y.; Neimark, A. V. Density Functional Theory Methods for Characterization of Porous Materials. *Colloid Surf., A* **2013**, *437*, 3–32.

(14) Wertheim, M. S. Fluids with Highly Directional Attractive Forces. I. Statistical Thermodynamics. *J. Stat. Phys.*, **1984**, *35*, 19–34.

(15) Wertheim, M. S. Fluids with Highly Directional Attractive Forces. II. Thermodynamic Perturbation Theory and Integral Equations. *J. Stat. Phys.*, **1984**, *35*, 35–47.

(16) Wertheim, M. S. Fluids with Highly Directional Attractive Forces. III. Multiple Attraction Sites. *J. Stat. Phys.*, **1986**, *42*, 459–476.

(17) Wertheim, M. S. Fluids with Highly Directional Attractive Forces. IV. Equilibrium Polymerization. *J. Stat. Phys.*, **1986**, *42*, 477–492.

(18) Tripathi, S.; Chapman, W. G. Microstructure of Inhomogeneous Polyatomic Mixtures from a Density Functional Formalism for Atomic Mixtures. *J. Chem. Phys.*, **2005**, *122*, 094506.

(19) Jain, S.; Dominik, A.; Chapman, W. G. Modified Interfacial Statistical Associating Fluid Theory: A Perturbation Density Functional Theory for Inhomogeneous Complex Fluids. *J. Chem. Phys.*, **2007**, *127*, 244904.

(20) Rosenfeld, Y. Free-Energy Model for the Inhomogeneous Hard-Sphere Fluid Mixture and Density-Functional Theory of Freezing. *Phys. Rev. Lett.*, **1989**, *63*, 980–983.

(21) Rosenfeld, Y.; Schmidt, M.; Lowen, H.; Tarazona, P. Fundamental-Measure Free-Energy Density Functional for Hard Spheres: Dimensional Crossover and Freezing. *Phys. Rev. E*, **1997**, *55*, 4245–4263.

(22) Hansen-Goos, H.; Roth, R. Density Functional Theory for Hard Sphere Mixtures: the White Bear Version Mark II. *J. Phys.: Condens. Matter*, **2006**, *18*, 8413–8425.

(23) Gil-Villegas, A.; Galindo, A.; Whitehead, P. J.; Mills, S. J.; Jackson, G.; Burgess, A. N. Statistical Associating Fluid Theory for Chain Molecules with Attractive Potentials of Variable Range. *J. Chem. Phys.*, **1997**, *106*, 4168–4186.

(24) Schindler, B. J.; Mitchell, L. A.; McCabe, C.; Cummings, P. T.; LeVan, M. D. Adsorption of Chain Molecules in Slit-Shaped Pores: Development of a SAFT-FMT-DFT Approach. *J. Phys. Chem. C* **2013**, *115*, 21337–21350.

(25) Schindler, B. J.; Buettner, L. C.; LeVan, M. D. Transition to Henry's Law in Ultra-Low Concentration Adsorption Equilibrium for n-Pentane on BPL Activated Carbon. *Carbon* **2008**, *46*, 1285–1293.

(26) Yu, Y. X.; Wu, J. Z. Density Functional Theory for Inhomogeneous Mixtures of Polymeric Fluids. *J. Chem. Phys.*, **2002**, *117*, 2368–2376.

(27) Steele, W. A. The Physical Interaction of Gases with Crystalline Solids. I. Gas-Solid Energies and Properties of Isolated Adsorbed Atoms. *Surf. Sci.*, **1973**, *36*, 317–352.

(28) Kruk, M.; Li, Z.; Jaroniec, M. Nitrogen Adsorption Study of Surface Properties of Graphitized Carbon Blacks. *Langmuir* **1999**, *15*, 1435–1441.

(29) Russell, B. P.; LeVan, M. D. Pore Size Distribution of BPL Activated Carbon Determined by Different Methods. *Carbon* **1994**, *32*, 845–855.

(30) Seaton, N. A.; Walton, J. P. R. B.; N. Quirke, N. A New Analysis Method for the Determination of the Pore Size Distribution of Porous Carbons from Nitrogen Adsorption Measurements. *Carbon* **1989**, *27*, 853–861.

(31) Avgul, N. N.; Kiselev, A. V. Physical Adsorption of Gases and Vapors on Graphitized Carbon Blacks. In *Chemistry and Physics of Carbon: Vol. 6*; edited by P. Walker. M. Dekker: New York, 1970.

CHAPTER VI

CONCLUSIONS AND RECOMMENDATIONS

The research presented in this dissertation focuses on fundamental knowledge of adsorption equilibrium of gases and their mixtures. This includes measurement of pure and mixture adsorption equilibrium as well as modeling adsorption, including the development of a new binary Henry's law relation, prediction of binary equilibrium using mixture coefficients determined from binary Henry's law behavior, and modeling pure gases using density functional theory.

The principle findings of this research are:

Adsorption equilibrium relations for mixtures

- Pure component isotherms of nitrogen and oxygen were measured on a LiLSX zeolite. The measurements were conducted at 25 and 75 °C and pressures up to 5 bar. Toth isotherms were used to model the measured data.

- The new Henry's law relation for a mixture with one component in excess was derived from the Ideal Adsorbed Solution Theory. The total amount adsorbed was approximately equal to the pure component loading of the excess component. The trace component was then shown to be a function of the fractional loading and the pure component loading of the excess component. From this, the Henry's law constant of the trace component with one component in excess became the pure component loading of the excess component divided by the pure component pressure of the trace component at the spreading pressure of the mixture, as shown in eq. 2.13.

- Binary Henry's law behavior for mixtures of nitrogen and oxygen with one component

in excess were measured. The trace component was held constant and the pressure of the component in excess was increased incrementally to 1 bar. The Henry's law constant for the trace component decreased with the increase in the pressure of the component in excess. Henry's law constants decreased more at lower pressures of the component in excess at 75 °C than at 25 °C.

- Two theories were used to describe the binary Henry's law data: the ideal adsorbed solution theory (IAST) and the virial excess mixture coefficients (VEMC). Both the IAST and VEMC utilized the Toth isotherm to describe the pure component isotherms. The Toth IAST was able to describe the trends of the Henry's law behavior, but was lacking in quantitative accuracy. The Toth VEMC was able to accurately describe the Henry's law behavior, both qualitatively and quantitatively. Mixture parameters for the Toth VEMC were determined for 25 and 75 °C solely from the binary Henry's law data.

- Binary adsorption equilibrium were measured at 25 and 75 °C at nominal pressures of 0.25 and 1.0 bar for a full range of compositions. The binary adsorption isotherms were predicted using pure component data along with the Toth IAST and Toth VEMC models. The Toth IAST was unable to accurately predict the binary isotherms, indicating some nonideality. The Toth VEMC, with mixture parameters determined explicitly from the binary Henry's law behavior, was able to accurately predict the binary isotherms.

High pressure adsorption on a carbon molecular sieve

- Pure component equilibrium isotherms of oxygen, argon, and nitrogen were measured on MSC-3R Type 172 carbon molecular sieve at temperatures from 25 to 100 °C and pressures up to 100 bar. Oxygen isotherms were measured up to 10 bar at 50, 75, and

100 °C due to safety concerns. Oxygen, argon, and nitrogen were seen to have similar loadings at 100 bar. A multi-temperature Toth isotherm was used to model oxygen and argon, while the traditional Toth isotherm was used to model nitrogen.

- The isosteric heat of adsorption was determined for oxygen and argon. The isosteric heat was seen to remain relatively constant with increasing loading and temperature. The isoteric heat values agreed with predicted values in the literature, but lower than other measured values in the literature.

- The isotherms of oxygen, argon, and nitrogen were compared with BPL activated carbon, another carbon molecular sieve, a superactivated carbon, two zeolites, and two titanosilicates. The MSC-3R Type 172 carbon molecular sieve had a similar isotherm capacity to that of the superactivated carbon for oxygen, which had a higher capacity than the other adsorbents. Argon loadings on the MSC-3R carbon molecular sieve were similar to those on the 5A zeolite and higher than on the other adsorbents. Nitrogen loadings were similar to those on a 13X zeolite at moderate pressures but had higher loadings at elevated pressures. The MSC-3R had similar loadings to those on BPL activated carbon but were consistently higher.

- Oxygen storage densities were calculated for the MSC-3R Type 172 carbon molecular sieve, which showed much higher storage densities than the bulk gas, with less than a 50% difference at 100 bar. The superactivated carbon had a much lower bulk density than the carbon molecular sieve, allowing the carbon molecular sieve to have a higher storage capacity per m^3 of adsorbent. It was hypothesized that surface reactions may be occuring between oxygen and the carbon surface.

Development of the SAFT-FMT-DFT approach

- The theory originally developed by Bryan Schindler was improved to model full

pores. Predictions were compared to literature Monte Carlo simulations for walls and molecules of increasing complexity. These included hard sphere and square-well wall potentials with hard sphere, hard chain, and square-well chain molecules.

- The square-well wall and square-well chain molecules were used to expand upon the literature comparisons. Whole pore densities were calculated from 1 to 8 σ_{ff}, noting the overlap of the wall potentials and resolution to the bulk density in the center of the larger pores. The Lennard-Jones 6-12 potential was also used to describe the wall potential, showing similar behavior to the square-well potential.

- The 10-4 potential was introduced as the wall potential to describe a more realistic wall. The 10-4 potential is a much stronger attractive potential, approximately an order of mangitude larger than that of the Lennard-Jones 6-12 potential. Whole pore densities were calculated at similar pores widths as the square-well wall, with the pore density profiles reaching much higher densities. Surface excess isotherms were calculated for attractive chains comprised of 1, 2, and 3 m-mers at a range of bulk packing fractions.

Modeling nitrogen and n-pentane with SAFT-FMT-DFT

- The attractive 10-4-3 wall potential was implemented into the theory to accurately describe carbon slit pores. Molecular parameters obtained by Bryan Schindler for nitrogen and n-pentane were used to model adsorption in carbon pores. Nitrogen pore densities were calculated for a range of pore widths and reduced pressures at 77 K. A pore size distribution for BPL activated carbon was obtained using the pore density calculations and a 77 K nitrogen isotherm from the literature.

- Pore density profiles were calculated for n-pentane for a range of pore widths and reduced pressures at 298.15 K. Using the pore size distribution obtained from nitrogen

calculations, a pentane isotherm was modeled. The isotherm was compared to experimental data of Bryan Schindler at 298.15K, agreeing well with the measured isotherm. It is shown that after having obtained a pore size distribution for a material, it is simple then to calculate accurate adsorption isotherms for other gases.

There are opportunities to continue portions of this research. My recommendations for future work are:

- There are possibilities of surface reactions occuring between oxygen and the surface of the carbon molecular sieves. Physical characterization techniques, both before and after oxygen exposure, would provide an insight into this. This is necessary before the carbon molecular sieve can be considered for high pressure oxygen storage.
- The SAFT-FMT-DFT model can be extended for calculations of binary mixtures. This would be useful for predicting adsorption of gas mixtures inside the pores of carbons or carbon composites.

APPENDIX A: LiLSX Isotherm Data

Tabulated data for pure component and binary mixtures of nitrogen and oxgyen on a LiLSX zeolite are provided here.

Pure Component Isotherms

Table A.1: Nitrogen adsorption data on zeolite LiLSX.

25 °C		75 °C	
n (mol/kg)	P (bar)	n (mol/kg)	P (bar)
0.016	0.029	0.010	0.013
0.020	0.039	0.039	0.053
0.051	0.107	0.100	0.152
0.052	0.105	0.217	0.368
0.108	0.199	0.416	0.805
0.128	0.240	0.660	1.57
0.341	0.517		
0.345	0.540		
0.656	0.871		
0.829	0.951		
0.884	1.03		
0.989	1.11		
1.30	1.30		
1.56	1.40		
1.62	1.47		
1.67	1.45		
1.94	1.54		
2.59	1.74		
3.23	1.89		
3.23	1.92		
3.88	2.07		
4.53	2.17		
5.17	2.30		

Table A.2: Oxygen adsorption data on zeolite LiLSX.

25 °C		75 °C	
n (mol/kg)	P (bar)	n (mol/kg)	P (bar)
0.0053	0.0187	0.0026	0.0205
0.0149	0.0627	0.0087	0.0705
0.0348	0.143	0.0234	0.196
0.0846	0.383	0.0549	0.479
0.203	0.933	0.106	0.983
0.218	0.989	0.170	1.64
0.263	1.30		
0.307	1.56		
0.355	1.79		
0.375	1.94		
0.492	2.59		
0.593	3.24		
0.694	3.88		
0.802	4.53		
0.892	5.17		

Binary Mixture Isotherms

Table A.3: Binary nitrogen and oxygen data at 25 °C and 1 bar.

N_2		O_2	
n (mol/kg)	P (bar)	n (mol/kg)	P (bar)
0	0	0.220	1.00
0.039	0.044	0.192	0.929
0.110	0.104	0.153	0.885
0.172	0.156	0.135	0.815
0.256	0.220	0.111	0.741
0.339	0.272	0.090	0.671
0.401	0.311	0.078	0.612
0.469	0.362	0.068	0.549
0.607	0.500	0.048	0.469
0.767	0.680	0.030	0.374
0.852	0.723	0.022	0.277
0.965	0.835	0.011	0.187
1.10	0.980	0.001	0.028
1.13	1.00	0	0

Table A.4: Binary nitrogen and oxygen data at 25 °C and 0.25 bar.

N_2		O_2	
n (mol/kg)	P (bar)	n (mol/kg)	P (bar)
0	0	0.0603	0.250
0.019	0.015	0.0505	0.233
0.051	0.035	0.0419	0.222
0.131	0.084	0.0247	0.188
0.203	0.131	0.0166	0.151
0.291	0.188	0.0087	0.111
0.362	0.218	0.0040	0.052
0.376	0.234	0.0023	0.028
0.39	0.25	0	0

Table A.5: Binary nitrogen and oxygen data at 75 °C and 1 bar.

N_2		O_2	
n (mol/kg)	P (bar)	n (mol/kg)	P (bar)
0	0	0.111	1.00
0.008	0.020	0.108	0.972
0.079	0.180	0.0858	0.866
0.147	0.291	0.0693	0.683
0.208	0.380	0.0526	0.526
0.261	0.512	0.0405	0.481
0.314	0.606	0.0309	0.383
0.375	0.700	0.0199	0.262
0.410	0.760	0.0135	0.197
0.480	0.849	0.0047	0.076
0.499	0.888	0.0010	0.032
0.515	1.00	0	0

Table A.6: Binary nitrogen and oxygen data at 75 °C and 0.25 bar.

N_2		O_2	
n (mol/kg)	P (bar)	n (mol/kg)	P (bar)
0	0	0.0261	0.250
0.016	0.028	0.0199	0.236
0.009	0.015	0.0226	0.229
0.023	0.037	0.0177	0.209
0.063	0.090	0.00708	0.134
0.101	0.163	0.00210	0.0937
0.126	0.193	0.00088	0.0499
0.142	0.245	0.00025	0.0267
0.150	0.250	0	0

APPENDIX B: CMS Approach to Equilibrium

Additional details on the approach to equilibrium of the carbon molecular sieve are provided here.

Approach to Equilibrium

We follow the material balances and rate equations from Wang and LeVan.[1] The system is a static volume with no net flow, so the material balance can be written as

$$M_s \frac{d\hat{n}}{dt} + \frac{d(cV)}{dt} = 0 \tag{B.1}$$

where M_s is the mass of the adsorbent, $\hat{n}$ is the total adsorbate concentration in the adsorbent, and $c = P/zRT$. For a microporous material, $\hat{n}$ can be written

$$\hat{n} = n + (\epsilon_p/\rho_p)c_p \tag{B.2}$$

$$c_p \approx c = P/zRT \tag{B.3}$$

where n is the average adsorbed phase concentration, ϵ_p is the macropore porosity, ρ_p is the particle density, and c_p is the average pore fluid concentration in the macropores. Using the $\hat{n}$ of equation B.2, equation B.1 can be rewritten as

$$M_s \frac{dn}{dt} + \frac{V + (\epsilon_p/\rho_p)}{RT} \frac{dP}{dt} = 0 \tag{B.4}$$

The simplest kinetics model, and the model that best describes the CMS material,[2] is the linear driving force model, which is expressed by

$$\frac{dn}{dt} = k(n^* - n) \tag{B.5}$$

where n^* is the adsorbed-phase concentration that would exist in equilibrium with the fluid-phase concentration surrounding the micropore region and k is the mass transfer coefficient. The isotherm is linearized around the equilibrium point, giving

$$n^* = n(P) = n_f + K(P - P_f) \tag{B.6}$$

where K is the local isotherm slope. Taking the Laplace transform of equation B.5, substituting into equation B.4 and integrating yields

$$\frac{P - P_f}{P_o - P_f} = e^{-at} \tag{B.7}$$

where

$$a = k\left(\frac{KM_sRT}{V + (\epsilon_p/\rho_p)} + 1\right) \tag{B.8}$$

References

(1) Wang, Y.; LeVan, M. D. Master Curves for Mass Transfer in Bidisperse Adsorbents for Pressure-Swing and Volume-Swing Frequency Response Methods. *AIChE J.* **2011**, *57*, 2054–2069.

(2) Giesy, T. J.; LeVan, M. D. Mass Transfer Rates of Oxygen, Nitrogen, and Argon in Carbon Molecular Sieves Determined by Pressure-Swing Frequency Response. *Chem. Eng. Sci.* **2013**, *90*, 250–257.

APPENDIX C: SAFT-FMT-DFT Additional Details

Additional details on the development and implementation of the SAFT-FMT-DFT are provided here.

Confined Fluid

For the hard sphere contribution, the derivative of F_{hs} is

$$\frac{\delta F_{hs}[\rho(\mathbf{r})]}{\delta\rho(\mathbf{r})} = \int \sum_i = \left.\frac{\partial \Phi_{hs}}{\partial n_i(\mathbf{r})}\right|_{\mathbf{r}'} \frac{\delta n_i(\mathbf{r}')}{\delta\rho(\mathbf{r})}\, d\mathbf{r}' \tag{C.1}$$

The n_i terms for $i = 2$, 3, and $V2$ are developed from

$$n_2(z) = 2\pi R \int_{z-R}^{z+R} \rho(z')dz' \tag{C.2}$$

$$n_3(z) = \pi \int_{z-R}^{z+R} \rho(z')[R^2 - (z'-z)^2]dz' \tag{C.3}$$

$$\mathbf{n}_{V2}(z) = \left(-2\pi \int_{z-R}^{z+R} \rho(z')(z'-z)dz'\right)\hat{\mathbf{z}} \;\equiv\; n_{V2}\,\hat{\mathbf{z}} \tag{C.4}$$

For the attractive terms, the derivatives of F_1 and F_2 are

$$\begin{aligned}\frac{\delta F_1[\rho(\mathbf{r})]}{\delta\rho(\mathbf{r})} &= \int \rho(\mathbf{r}')g_{hs}[n_3(\mathbf{r}'');\mathbf{r}']\phi(|\mathbf{r}'-\mathbf{r}|) \\ &\quad + \int \rho(\mathbf{r}') \int \rho(\mathbf{r}'')\frac{\delta g_{hs}[n_3(\mathbf{r}'');\mathbf{r}'']}{\delta\rho(\mathbf{r}'')}\phi(|\mathbf{r}'-\mathbf{r}''|)d\mathbf{r}''d\mathbf{r}'\end{aligned} \tag{C.5}$$

$$\begin{aligned}\frac{\delta F_2[\rho(\mathbf{r})]}{\delta\rho(\mathbf{r})} &= -\frac{1}{2kT}\int \rho(\mathbf{r}')(1+2\xi n_3^2)[\phi(|\mathbf{r}-\mathbf{r}'|)]^2 K_{hs}(\mathbf{r}')g_{hs}[n_3(\mathbf{r}');\mathbf{r}']d\mathbf{r}' \\ &\quad -\frac{1}{4kT}\int \rho(\mathbf{r}')\int \rho(\mathbf{r}'')[\phi(|\mathbf{r}'-\mathbf{r}''|)]^2\frac{\partial n_3}{\partial\rho}\Bigg(4\xi n_3(\mathbf{r}'')K_{hs}(\mathbf{r}'')g_{hs}[n_3(\mathbf{r}'');\mathbf{r}''] \\ &\quad +(1+2\xi n_3(\mathbf{r}''))\left[\frac{\partial K_{hs}(\mathbf{r}'')}{\partial n_3(\mathbf{r}'')}g_{hs}[n_3(\mathbf{r}'');\mathbf{r}''] + K_{hs}(\mathbf{r}'')\frac{\partial g_{hs}[n_3(\mathbf{r}'');\mathbf{r}'']}{\partial n_3(\mathbf{r}'')}\right]\Bigg)d\mathbf{r}'d\mathbf{r}''\end{aligned} \tag{C.6}$$

where $\xi = 1/\eta_{con}^2$. For the chain contribution, the derivative of F_{chain} is

$$\frac{\delta F_{chain}[\rho(\mathbf{r})]}{\delta\rho(\mathbf{r})} = \int \sum_i \left.\frac{\partial \Phi_{chain}}{\partial n_i(\mathbf{r})}\right|_{\mathbf{r}'} \frac{\delta n_i(\mathbf{r}')}{\delta\rho(\mathbf{r})} d\mathbf{r}' \tag{C.7}$$

The equation set was solved using a Picard iteration with Anderson mixing[1,2] and $\Delta z = R/40$.

Bulk Fluid

The chemical potential for the system is calculated using the following equations for a bulk fluid. There are two different densities, the molecular density ρ_m and the segment density ρ_s, where $\rho_s = m\rho_m$. The chemical potential is calculated as the derivative of the Helmholtz free energy in the bulk, A, with respect to ρ_m, i.e.,

$$\mu = \frac{\partial A}{\partial \rho_m} \tag{C.8}$$

where $A = A_{id} + A_{hs} + A_1 + A_2 + A_{chain}$. This gives for the ideal fluid

$$A_{id} = kT\rho_m \left[\ln(\Lambda^3\rho_m) - 1\right] \tag{C.9}$$

and yields eq 4.5. For the hard sphere fluid, we have

$$A_{hs} = kT \sum_{i=0}^{3} \Phi_b^{hs}[n_{\alpha,b}(\mathbf{r})] \tag{C.10}$$

where $\Phi_b^{hs} = \Phi^{hs}[n_{\alpha,b}(\mathbf{r})]$. This gives eq 4.18. The first-order attractive potential, derived by Gil-Villegas *et al.*,[3] is described by

$$A_1 = -4\epsilon(\lambda^3 - 1)n_{3,b}\rho_s g_e^{hs} \tag{C.11}$$

which gives eq 4.21. In contrast to the original SAFT-VR approach, the second-order attractive potential derived by Zhang[5] has been used and is given by

$$A_2 = -2\beta\epsilon^2(\lambda^3 - 1)\left[\rho_s n_{3,b}(1 + \xi n_{3,b}^2)K^{hs} g_e^{hs}\right] \tag{C.12}$$

which gives eq 4.27. The chain term of the Helmholtz free energy in the bulk is[4]

$$A_{chain} = kT \int \Phi_b^{chain}\, d\mathbf{r} \tag{C.13}$$

where $\Phi_b^{chain} = \Phi^{chain}[n_{\alpha,b}(\mathbf{r})]$. Differentiation gives eq 4.32.

References

(1) Anderson, D. G. Iterative Procedures for Nonlinear Integral Equations. *J. Assoc. Comp. Mach.*, **1965**, *12*, 547–560.

(2) Eyert, V. A Comparative Study of Methods for Convergence Acceleration of Iterative Vector Sequences. *J. Comp. Phys.*, **1996**, *124*, 271–285.

(3) Gil-Villegas, A.; Galindo, A.; Whitehead, P. J.; Mills, S. J.; Jackson, G.; Burgess, A. N. Statistical Associating Fluid Theory for Chain Molecules with Attractive Potentials of Variable Range. *J. Chem. Phys.*, **1997**, *106*, 4168–4186.

(4) Yu, Y. X.; Wu, J. Z. Density Functional Theory for Inhomogeneous Mixtures of Polymeric Fluids. *J. Chem. Phys.*, **2002**, *117*, 2368–2376.

(5) Zhang, B. J. Calculating Thermodynamic Properties from Perturbation Theory II. An Analytical Representation of Square-Well Chain Fluid. *Fluid Phase Equil.*, **2001**, *180*, 182–194.

APPENDIX D: Gravimetric LiLSX Data

Gravimetric pure component isotherms on a LiLSX zeolite are presented here.

Table D.1: CO_2 adsorption data on zeolite LiLSX.

10 °C		25 °C		40 °C		55 °C	
P (kPa)	n (mol/kg)	P (kPa)	n (mol/kg)	P (kPa)	n (mol/kg)	P (kPa)	n (mol/kg)
0.6805	3.140	0.3903	2.703	0.4540	2.366	0.6511	2.012
1.322	3.299	0.6566	2.769	0.6716	2.414	1.301	2.211
2.601	3.531	1.307	2.926	1.309	2.583	2.601	2.456
6.405	3.975	2.570	3.144	2.600	2.815	6.426	2.834
12.79	4.445	6.408	3.545	6.426	3.190	12.83	3.171
25.62	5.008	12.87	3.925	12.83	3.534	25.68	3.564
45.18	5.474	25.62	4.424	25.68	3.963	45.16	3.940
64.59	5.743	45.17	4.892	45.12	4.384	64.58	4.213
98.31	6.039	64.58	5.179	64.52	4.683	98.15	4.555
133.0	6.244	98.38	5.536	98.18	5.040	131.6	4.837
162.1	6.357	131.8	5.769	135.7	5.322	162.7	5.021
204.3	6.482	162.5	5.899	163.1	5.458	205.6	5.222
262.1	6.611	203.8	6.024	198.1	5.610	262.7	5.419
325.4	6.719	259.7	6.187	272.6	5.847	324.3	5.583
389.1	6.808	337.9	6.334	326.2	5.967	409.4	5.755
453.2	6.880	389.5	6.395	410.0	6.117	454.5	5.829
517.8	6.943	453.8	6.486	454.2	6.180	518.6	5.923
		518.6	6.548	518.6	6.250		

Table D.2: Nitrogen adsorption data on zeolite LiLSX.

10 °C		25 °C		40 °C		55 °C	
P (kPa)	n (mol/kg)	P (kPa)	n (mol/kg)	P (kPa)	n (mol/kg)	P (kPa)	n (mol/kg)
25.78	0.7637	25.82	0.4710	25.76	0.3202	25.79	0.2079
46.02	1.040	46.62	0.6929	46.90	0.4916	47.37	0.3452
66.59	1.244	65.56	0.8708	65.66	0.6301	65.68	0.4428
98.60	1.482	98.89	1.105	100.0	0.8311	100.8	0.6070
129.9	1.680	129.9	1.296	131.3	0.9964	131.9	0.7426
155.6	1.798	155.8	1.397	155.9	1.090	156.1	0.8270
194.2	1.940	194.3	1.540	194.5	1.233	194.7	0.9451
258.7	2.146	258.7	1.736	259.1	1.423	259.4	1.124
323.2	2.301	323.3	1.918	323.5	1.581	323.7	1.285
387.8	2.441	388.0	2.066	388.0	1.729	388.3	1.420
452.4	2.561	452.5	2.167	452.6	1.850	452.9	1.538
517.0	2.665	517.3	2.299	517.4	1.953	517.5	1.646

Table D.3: Oxygen adsorption data on zeolite LiLSX.

10 °C		25 °C		40 °C		55 °C	
P (kPa)	n (mol/kg)	P (kPa)	n (mol/kg)	P (kPa)	n (mol/kg)	P (kPa)	n (mol/kg)
0.6465	0.01663	0.7444	0.01981	0.6905	0.01025	0.9064	0.009070
1.260	0.01931	1.608	0.02004	1.452	0.01646	1.295	0.01958
2.541	0.02322	2.540	0.02040	2.548	0.01901	2.539	0.01141
6.410	0.03448	6.412	0.02831	6.417	0.02744	6.402	0.02359
12.87	0.05610	12.88	0.04597	12.87	0.04135	12.85	0.02913
25.80	0.09733	25.80	0.07220	26.67	0.05809	25.76	0.04442
46.89	0.1524	46.51	0.1147	45.15	0.08918	46.90	0.07639
65.60	0.2087	65.57	0.1513	66.83	0.1251	65.64	0.09835
100.6	0.2998	98.95	0.2134	99.81	0.1863	98.64	0.1412
130.2	0.3579	129.8	0.2830	130.8	0.2182	130.3	0.1884
155.6	0.4234	155.9	0.3270	156.0	0.2567	156.1	0.2212
194.2	0.5121	194.2	0.4050	194.7	0.3164	194.6	0.2669
258.7	0.6573	258.9	0.5215	259.1	0.4164	259.2	0.3272
323.2	0.7996	323.5	0.6228	323.6	0.4966	323.7	0.3967
387.7	0.9370	387.8	0.7241	388.3	0.5832	388.3	0.4586
452.3	1.064	452.6	0.8316	452.8	0.6568	452.8	0.5294
516.9	1.201	517.1	0.9216	517.3	0.7408	517.5	0.5820

Table D.4: Argon adsorption data on zeolite LiLSX.

10 °C		25 °C		40 °C		55 °C	
P (kPa)	n (mol/kg)	P (kPa)	n (mol/kg)	P (kPa)	n (mol/kg)	P (kPa)	n (mol/kg)
0.2653	0.009920	0.4058	0.006300	0.6590	0.005180	6.409	0.005090
0.8651	0.01037	0.6935	0.01032	1.261	0.006320	12.86	0.005550
1.308	0.01416	1.279	0.00823	2.566	0.007010	25.79	0.01003
2.548	0.01364	2.569	0.00640	6.439	0.01041	45.57	0.02440
6.414	0.02173	6.447	0.01374	12.89	0.01763	66.87	0.03938
12.86	0.03672	12.90	0.02115	25.79	0.02409	101.0	0.05785
25.78	0.06791	26.10	0.03807	46.09	0.04814	96.7	0.05436
45.16	0.1196	47.01	0.06640	67.12	0.06435	121.5	0.06445
65.65	0.1674	67.66	0.09311	101.4	0.09472	159.9	0.08657
99.16	0.2488	98.40	0.1305	101.6	0.09687	224.3	0.1214
130.8	0.3005	110.1	0.1475	126.2	0.1198	288.7	0.1638
156.3	0.3479	135.9	0.1802	164.8	0.1590	353.4	0.1893
194.9	0.4248	174.4	0.2262	229.2	0.2065	417.8	0.2274
259.4	0.5452	238.9	0.3026	293.6	0.2578	482.5	0.2619
323.8	0.6537	303.4	0.3781	358.2	0.3104		
388.3	0.7585	367.7	0.4519	422.7	0.3615		
452.9	0.8584	432.5	0.5179	497.1	0.4112		
517.5	0.9499	497.0	0.5778				